Magnetotelluric Imaging of Electrically Anisotropic Crust Near Fort
McMurray, Alberta:

Implications for Engineered Geothermal Systems

by

Mitchell V. Liddell

A thesis submitted in partial fulfillment of the requirements for the degree of

Master of Science
in
Geophysics

Department of Physics
University of Alberta

Abstract

The goal of this thesis is to investigate the character of the basement rocks beneath the oilsands region around Fort McMurray in the context of developing engineered geothermal systems (EGS). Magnetotelluric (MT) data were collected at 94 stations on two profiles near to Fort McMurray and initial inversions showed that while these data exhibited strong 2-D character, an isotropic analysis of the MT data was not possible. Forward modeling of 2-D anisotropy showed that the basement below a depth of 4 - 5 km is electrically anisotropic with a resistivity ratio close to 1000. It was also shown that certain features of MT data commonly interpreted with a 3-D model could be explained with 2-D anisotropic model. The source of the anisotropy was interpreted to be due to interconnected graphite films oriented ~S27°E within the metamorphic basement rocks. This direction is reasonably close to the current minimum stress direction of ~S40°E, the interaction between the rock MT-interpreted rock fabric and the stress direction will control the propagation of artificial fractures.

Acknowledgements

Table of Contents

List of figures

Figure 2.13: Modified from Heise et al., (2006). Forward models on the left of each image have produced the apparent resistivity and phase responses in the middle panels, and the phase tensors in the right panels. Image (g) has the apparent resistivity and phase response AFTER rotation and alignment to the phase tensor azimuth axes. Shading of phase tensors does not represent skew value, but rather the value of φmax and is thus related to the amount of phase split (ellipticity).

Figure 2.14: From Heise & Pous (2003). 2-D anisotropic model used to create higher than 90° phase in stations places above the shallow block, marked by "> 90". Regional 2-D strike set to 0° (into page). Numbers represent anisotropic resistivity values in directions following the pattern X/Y/Z. The angle α represents the clockwise rotation of the anisotropic axes from the 2-D axes.

Figure 2.15: For a site directly above an anisotropic block with $\alpha s = 15°$ away from the 2-D strike. The color represents the phase differences $\varphi yx - \varphi xy$ with varying depth to top of the block from 0.3 to 3 km. Geometry of the block is fixed and anisotropy ratio within the block is 1000/10 with background resistivity 1000 Ωm. Central white anomalous regions indicate rotation angle/signal period regions that exhibit OOQ phase. Image was provided by Dr. Josef Pek. Note that period is longest at the top of these images; it is long period MT data that will exhibit the OOQ phase effects.

Figure 3.1: Map of the ages and lithological groupings in Western Laurentia. Surface geological data from Hoffman (1988) and structures at depth come from Ross et al., (1991). Modified from McDonough et al., (2000).

Figure 3.2: Map of Alberta showing Precambrian basement terrane boundaries superimposed on the total magnetic field residual map for Northeastern Alberta. Identified are the Taltson Magmatic Zone (T), the Buffalo Head (B), and Rae (R). The star indicates the location of the FMC study region inside the Taltson. Plotted in GMT with information from Ross et al., (1991) and magnetic field data from Natural Resources Canada.

Figure 3.3: Magnetic susceptibility of Northeastern Alberta granite gneiss shield rock samples as a function of the percent of magnetite content. The term cgs denotes centimetre-gram-seconds units. Susceptibility is dimensionless and the linear the relationship is the important feature here, not the value. Modified from Sprenke et al., (1986).

the diagram portrays the true nature of the azimuths. The red region indicates the zone of high skew and oriented phase tensor azimuths.

the ideal phase tensor azimuth as a function of period (red) and the distorted result due to skew (dashed line). Panel three plots the values of φmax and φmin against the natural TE/TM phase. Panel four shows the change in phase tensor skew β as a function of period.

Figure 8.1: Seismic section coincident with the Tower Road MT profile. Location of the Hunt Well is indicated. Coloured boxes indicate the location of potential dipping reflectors, both shallow and deep, from (Chan, 2013). (b) comparison of seismic section with Tower Road shortened bandwidth inversion of the upper 4-5 km compared to seismic section. (c) Comparison of seismic section with forward model from Figure 7.7.

Figure 8.2: Bouguer anomaly contour map for the FMC region (Left). Residual magnetic field data for the FMC region combined with regional strike direction for each site (Right). Gravity and magnetic data downloaded from Natural Resources Canada.

Figure 8.3: Bulk resistivity measurements made parallel and orthogonal to the direction of the conducting phase in a simplified anisotropy model. Resistive and conductive values are chosen to represent unweathered granite and graphite, respectively.

Figure 8.4: Total field aeromagnetic map for the exposed Canadian Shield in northern Alberta. ALP, Arch Lake pluton; AnLP, Andrew Lake pluton; CLSZ, Charles Lake shear zone; CLP, Colin Lake pluton; SP; Slave pluton, WLP, Wylie Lake pluton, TBC; Taltson basement complex. Modified from McDonough et al., (2000).

Figure 8.5: Residual field aeromagnetic data for the larger FMC region. MT profiles are indicated with white outlines. The location of Fort McMurray and Fort McKay are indicated. Letter symbols indicate geological provinces: T = Taltson Magmatic Zone, R = Rae Province, B = Buffalo Head Terrane. Brown circles indicate location of two core samples analyzed by Walsh (2013). Magnetic data downloaded from Natural Resources Canada.

List of symbols and abbreviations

1-D	One Dimensional
2-D	Two Dimensional
3-D	Three Dimensional
ABT	Alberta Basement Transect
BH	Buffalo Head
CLsz	Charles Lake Shear Zone
EGS	Engineered Geothermal System
EM	Electromagnetic
FMC	Fort McMurray
FMCn	Fort McMurray North
GSLsz	Great Slave lake Shear Zone
IV	Induction Vector
MT	Magnetotelluric
OOQ	Out of Quadrant
RHP	Radiogenic Heat Production
SAB	Southern Alberta
SAGD	Steam Assisted Gravity Drainage
STZ	Snowbird Tectonic Zone
TBC	Taltson Basement Complex
TE	Transverse Electric
THO	Trans Hudson Orogen
TM	Transverse Magnetic
TMZ	Taltson Magmatic Zone
TR	Tower Road
WCSB	Western Canada Sedimentary Basin

Chapter 1

Introduction

This thesis was completed as part of Theme 4 of the Helmholtz-Alberta Initiative (HAI), which has been examining the feasibility of using geothermal energy as a heat source for the oilsands industry in northern Alberta. The oilsands industry uses large amounts of heat to produce the hot water needed to separate sand and bitumen, and also to generate the steam that is used to extract bitumen from underground formations through steam assisted gravity drainage (SAGD). The hot water and steam are currently obtained from cold river water, heated by burning vast quantities of natural gas. This process has significant economic and environmental costs; approximately one billion dollars are spent each year on natural gas and relevant carbon taxes while the greenhouse gas emissions from oilsands processing is responsible for 6% of Canada's total carbon emissions (Majorowicz et al., 2012). Engineered Geothermal Systems (EGS) may be able to mitigate both the economic and environmental impacts by providing a cheaper source of hot water and significantly reduced greenhouse gas emissions. In contrast to conventional geothermal systems, which make use of naturally occurring water and permeability to extract heat from the Earth, the development of EGS requires that permeability is created and water, or perhaps carbon dioxide, is injected into the Earth.

There are challenges to EGS development from both a financial and technological standpoint. The drilling of wells is very expensive, and drilling into crystalline rocks such as those of the Albertan basement would be even more so. A lot of effort is therefore spent identifying suitable target regions and characterizing the rocks that will be encountered. Studies by Majorowicz et al., (2012) and Walsh (2013) have determined that the geothermal gradient near fort McMurray is ~21ºC/km, and the 2.3 km deep Hunt

well has a bottom-hole temperature of 47ºC (Chan, 2013). Drilling to depths between 4

km and 7 km is necessary to reach the temperatures of 80ºC - 100ºC required for EGS.

To make the development economic requires long-term planning; the price of natural gas

and the magnitude of carbon taxes in the future are likely to increase over the 30 years

over which an EGS will operate. Once the initial cost of drilling is overcome, fractures

must be created and pumping must be maintained with an adequate flow rate, above

40 L/s is estimated to be necessary for any one system.
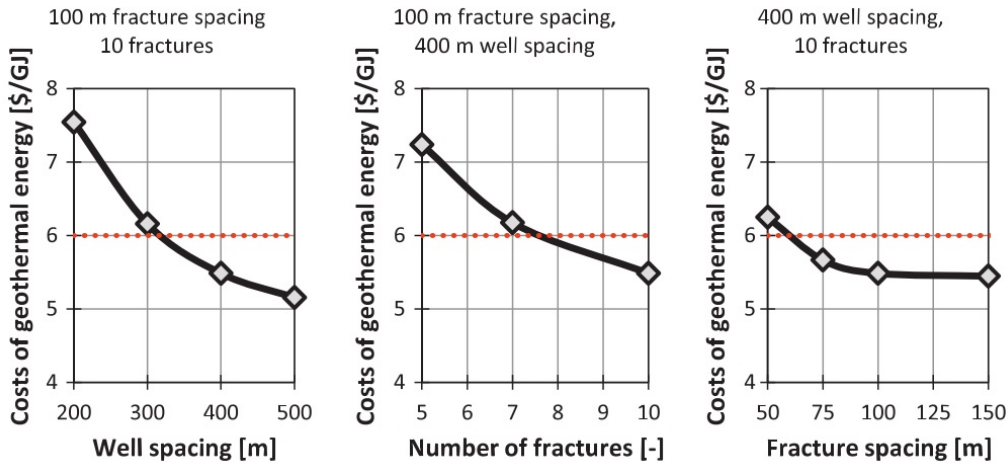
Figure 1.1: From Hofmann et al., (2014). Financial costs of EGS produced energy as a function of well spacing, number of fractures and spacing of fractures. Red dotted line shows estimate of current cost per GJ from burning natural gas**.**

Hofmann et al., (2014) looked at the economics of EGS development near Fort

McMurray, and showed that drilling costs would likely be half of the total cost, which

means that if an EGS is functional it can indeed be economic. Under certain assumptions

about the details of the fractures, the current technology behind EGS can be more cost

effective than the current practice of burning natural gas to heat water (Figure 1.1). The

economic potential of EGS is dependent upon the suitability of the geology in the target

region. It is, therefore, one of the goals of this thesis to contribute to the characterization

of the basement rocks near Fort McMurray with a view to future geothermal development.

Prior to any geothermal development, geophysical exploration is needed to characterize the subsurface in the target area. Magnetotellurics (MT) measures electrical resistivity, and can resolve resistivity structure at the depths that would be used in EGS, i.e., 5 - 10 km. Resistivity is a rock property widely used geothermal exploration and analysis of the MT data will be valuable for possible EGS development in the area.

Chapter 2 first introduces the magnetotelluric (MT) method and explains how it measures the resistivity structure of the subsurface from the Earth's surface. The concepts of dimensionality and directionality in MT data are introduced. Common ways to display MT data, such as the apparent resistivity, phase, and phase tensor, are explained. Examples of the MT response are presented for a set of resistivity structures. Electrical anisotropy is considered as a final generalization and the MT response of anisotropic media is examined in detail.

The geological history and major geological units of the study area are introduced in **Chapter 3**. Specific attention is given to the Taltson Magmatic Zone (TMZ), in which the Fort McMurray (FMC) region is located. The magnetic character of the rocks is suggested to be dependent upon the magnetite content and aeromagnetic maps of the region are presented. Finally, the depositional setting of the Western Canada Sedimentary Basin (WCSB) is summarized.

In **Chapter 4** the various types of geothermal resource are reviewed. The concept of EGS is introduced and a literature review of various electromagnetic geothermal exploration methods is presented. Typical sources of resistivity in geothermal zones and their values are given, and their detection with magnetotellurics discussed along with the

methodology of EGS exploration using a range of electromagnetic methods, with a specific focus on magnetotellurics.

The FMC magnetotelluric data are analyzed in detail in **Chapter 5**. Tensor decomposition is performed to find a regional geoelectric strike direction as a function of signal period to determine if the data can be interpreted using a 2-D approach. Distortional parameters and phase tensors are used to determine if noise or 3-D induction effects are present, and to what degree they affect the MT data. The analysis of strike direction and phase tensor characteristics in Chapter 5 leads to the splitting of the Northern FMCn profile into two parts.

2-D isotropic inversions of the MT data are presented in **Chapter 6**. MT data that appear to be non 2-D are removed from the analysis. The suitability of the 2-D inversion models from the three MT profiles to accurately characterize the FMC basement are discussed and it is determined that a 2-D isotropic assumption is not valid for these data. A reduced bandwidth inversion including only electrically isotropic MT data was carried out and showed that the resistivity structure was approximately 1-D from the surface to a depth of 4-5 km.

Chapter 7 describes in detail the evidence that the FMC MT data are anisotropic. The implications from each piece of evidence are combined to guide the development of a 2-D anisotropic resistivity model that succeeds in explaining all of the complicated features present in the observed MT data. Anisotropic forward modelling is completed with these data using the modelling code developed by Pek & Verner (1997). The fit between the predicted and measured MT data is seen to be acceptable in all aspects. It is shown that parameters in the MT data that are often interpreted to be due to 3-D resistivity structure can actually be explained with 2-D electrical anisotropy.

4

The final chapter of the thesis is **Chapter 8**. It summarizes the interpretations from other studies in the FMC region and presents a joint interpretation of the source of the regional electrical anisotropy in the FMC basement rocks. The implication of these MT data, and their geological interpretation, for geothermal exploitation of the FMC basement rocks in Northern Alberta is discussed.

Chapter 2

The Magnetotelluric Method

Magnetotellurics is a passive geophysical technique that uses the interaction of natural electromagnetic (EM) waves with the Earth to measure the electrical resistivity (reciprocal conductivity) at depth. It was introduced independently by Cagniard (1953) and Tikhonov (1950). By recording EM signals with a broad range of frequencies (periods), MT can investigate the resistivity of the Earth from depths of less than a hundred meters to several hundred kilometres. The electromagnetic signals used in MT are generated by solar interactions with the magnetosphere (periods >1 s) or by worldwide lightning strikes (periods <1 s) (Vozoff, 1991). When the EM signals enter the Earth, they are measured by MT instruments and from the ratio of the electric and magnetic field components, the resistivity of the Earth can be determined. For clarity, note that period is the reciprocal of frequency, f.

2.1 Governing Equations

The Maxwell Equations (Maxwell, 1861) are the basis for the modern understanding of electromagnetism and, therefore also for magnetotellurics. The Maxwell Equations listed in ((2.1-(2.4)) explain the generation and propagation of electric and magnetic fields and describe how the two are inextricably linked in EM waves.

$$\nabla \cdot \boldsymbol{E} = {\gamma}/{\varepsilon_0} \tag{2.1}$$

$$\nabla \cdot \boldsymbol{B} = 0 \tag{2.2}$$

$$\nabla \times \boldsymbol{E} = -\frac{\partial}{\partial t}\boldsymbol{B} \tag{2.3}$$

$$\nabla \times \boldsymbol{B} = \mu_0 \boldsymbol{J} + \frac{\partial}{\partial t} \boldsymbol{E} \qquad (2.4)$$

In Maxwell's equations $\boldsymbol{E}$ represents the electric field strength, measured in volts per metre $(\frac{V}{m})$, and $\boldsymbol{B}$ is the magnetic flux, measured in Teslas (T). The constants μ and ε are the magnetic permeability and dielectric permittivity, respectively. The magnetic permeability departs from its free space value only in large ore bodies and can usually be assumed to be equal to the free space value μ_0. The presence of polar molecules determines the dielectric permittivity. It will be shown that at the long periods used by MT, electromagnetic signals travel diffusively in the Earth, so the free space value for permittivity can be used without error, since it is only found in the term describing the displacement current.

Equation (2.3) is known as Faraday's Law and shows how a time varying magnetic field will induce an electric field. The cross product applied to the electric field in Faraday's Law shows that the induced electric field will be perpendicular to the magnetic field; the negative sign ensures the conservation of energy. This concept can also be expressed as Lenz's Law. Equation (2.4) is a modified form of Ampere's law with displacement current added, and shows that a time varying electric field can produce a magnetic field. The total electric charge density is represented by (γ). It is possible to combine equations (2.3) and (2.4) to give (2.5):

$$\nabla^2 \boldsymbol{E} = \mu\sigma \frac{\partial}{\partial t} \boldsymbol{E} + \mu\varepsilon \frac{\partial^2}{\partial t^2} \boldsymbol{E} \qquad (2.5)$$

Equation (2.5) is a damped wave equation for the electric field. The first term comes from the conduction current, and the second term from the displacement current. Equation (2.5) shows that there are two ways in which an EM signal may propagate. In a vacuum or near-perfect resistor, such as the atmosphere, the conductivity is zero and the

displacement current dominates so that energy is transmitted as an electromagnetic wave. In conductive media such as the Earth, the conductivity is large enough (generally greater than 10^{-4} S/m) that the conduction current is much stronger than the displacement current term. EM signals therefore travel diffusively within the Earth and decay at a rate that can be related to the conductivity. The conductivity is outside of the time derivative in the conduction current term of equation (2.5), so it must be constant in time. There is therefore a relationship between EM signal decay rate and conductivity, this is important in the following discussion of the electromagnetic skin depth.

2.1.1   Electromagnetic Skin Depth

The EM signals used in MT originate outside the Earth, and most of the energy of the EM wave is reflected at the Earth/air interface. A small amount is transmitted and propagates in a diffusive manner within the Earth. The vertically propagating EM field is governed by equation (2.6):

$$\nabla^2 \boldsymbol{E} = \mu\sigma \frac{\partial}{\partial t} \boldsymbol{E} \tag{2.6}$$

Regardless of the angle of incidence, the transmitted EM signal will be refracted and travel almost vertically downwards in the Earth. This is because of the large velocity contrast for the EM wave between the resistive atmosphere and the conductive Earth. Equation (2.6) is a diffusion equation that can be solved by assuming a harmonic time variation of the form:

$$\boldsymbol{E} = \boldsymbol{E}_0 e^{-kz} e^{-i\omega t} \tag{2.7}$$

Equation (2.7) has an exponential variation with depth, z. The term $\boldsymbol{E}_0$ is the value of the electric field at the surface of the Earth ($z = 0$) and the angular frequency ω is $2\pi f$. The variable k depends upon the frequency of the wave and the conductivity of the Earth from

equation (2.6). The electromagnetic skin depth, δ, is defined as the depth in equation (2.7) at which the magnitude of $\boldsymbol{E}$ has decreased from $|\boldsymbol{E}_0|$ to $|\boldsymbol{E}_0|e^{-1}$. It can be shown that the skin depth is:

$$\delta = \sqrt{\frac{2}{\omega\mu\sigma}} \approx 503\sqrt{\rho T} \qquad (2.8)$$

The EM signal period is T, and ρ is the resistivity of the Earth. A conductive material will cause the EM signal to decay more quickly with depth than a resistive material; similarly a short period EM signal will decay more quickly than one with a long period. It is important to note that ρ represents an *average* resistivity over a half sphere with a radius of the skin depth. To obtain a depth sounding of resistivity, signals of a variety at periods can be measured. By recording data at a number of stations, the changes between them can be examined to determine lateral variations in subsurface resistivity structure.

To first order, crustal rocks are quite resistive ($>1000\ \Omega$m) so any conductive feature such as a region with saline fluid in the pore space or graphite films will be relatively low in resistivity (Palacky, 1987). EM signals diffusing in the Earth naturally lose resolution at long periods as they sample a much larger volume.

2.2   Magnetotelluric Impedance and Apparent Resistivity

MT data are recorded in the time-domain and generally analysed in the frequency domain. This means that the signals must be Fourier transformed during data processing. The previous section outlined how signal frequency determines the penetration depth of EM signals diffusing downwards in the Earth.

MT data collection usually records the electric and magnetic fields in two horizontal and orthogonal directions. The time series are converted into the frequency domain as

described above. The x-direction is usually defined as North and the y-direction as East.

The impedance Z_{xy} is defined as the ratio of the electric field in the x-direction, E_x, and

magnetic field in the y-direction, H_y, as:

$$Z_{xy}(\omega) = \frac{E_x(\omega)}{H_y(\omega)} \tag{2.9}$$

Note that the impedance has units of Ohms and is a frequency dependant, complex

quantity. From now on, the dependence of field components and impedances on angular

frequency (ω) will be considered implicit. The components of the electric and magnetic

fields can be used to calculate the impedance tensor, $\boldsymbol{Z}$ as.

$$\begin{bmatrix} E_x \\ E_y \end{bmatrix} = \begin{bmatrix} Z_{xx} & Z_{xy} \\ Z_{yx} & Z_{yy} \end{bmatrix} \begin{bmatrix} H_x \\ H_y \end{bmatrix} \tag{2.10}$$

Equation (2.10) is the basis for all the MT data analysis presented in the following

sections. The impedance tensor contains information about the Earth at that particular

site, as a function of frequency.

As explained above, the frequency of the EM signal can be related to the depth of

penetration through the skin depth equation (2.8). A useful way to examine the MT data

is to calculate a so-called apparent resistivity from each element of the impedance tensor

at each frequency as:

$$\rho_{xy} = \frac{1}{2\pi f \mu} |Z_{xy}|^2 \tag{2.11}$$

The apparent resistivity in equation (2.11) can be considered to be the average resistivity

of the Earth over the volume sampled by the EM signal, at a given frequency (period). If

the true resistivity of the Earth varies with depth, then the apparent resistivity will vary

with frequency (period) and can be plotted as an apparent resistivity curve (Figure 2.1).

Because the impedance is a complex quantity it can be expressed in the form $Z = |Z|e^{i\Phi}$, with the phase angle defined as the argument Φ. Each impedance tensor element will have its own phase value:

$$\Phi_{xy} = tan^{-1}(Z_{xy}) = tan^{-1}\left(\frac{E_x}{H_y}\right) \qquad (2.12)$$

In a perfect resistor, the orthogonal electric and magnetic components of an EM wave are in phase i.e. $\Phi = 0$. If the EM wave is travelling in a material with non-zero conductivity, then there will be a delay between the electric and magnetic field components. In a conductive medium the electric and magnetic field components are no longer in phase, there is a delay introduced of quarter of a cycle so that the phase difference between E_x and its H_y will be $(\frac{\pi}{4})$, or 45°. If there is a vertical resistivity gradient in the medium, then the phase difference will depart from 45°. Increasing resistivity with depth means $\Phi < 45°$, decreasing resistivity with depth means $\Phi > 45°$. If the resistivity of the Earth changes with depth then the signal decay rate will change with frequency and cause the apparent resistivity curve change in turn. An approximation of the magnetotelluric phase can be derived from the derivative of apparent resistivity with respect to period as:

$$\Phi_{xy} = 45\left(1 - \frac{d(log_{10}\rho_{xy})}{d(log_{10}T)}\right) \qquad (2.13)$$

Equation (2.13) shows how phase angle is related to apparent resistivity. If the apparent resistivity increases with signal period then the phase will be below 45° and, in turn, if apparent resistivity decreases, the phase will be greater than 45°. A constant apparent resistivity will result in the phase being exactly 45°. Apparent resistivity curves and their respective phases are convenient and often used to visualize MT data. An example of an apparent resistivity curve is given in Figure 2.1.

Note that in this plot, apparent resistivity and phase are plotted for two orthogonal
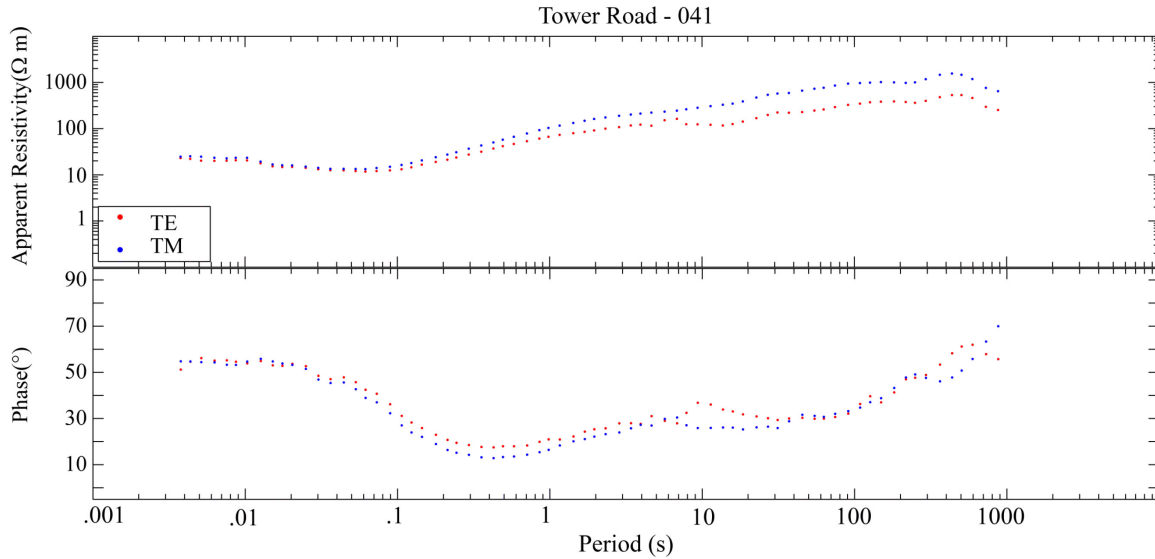
Figure 2.1: A typical MT sounding curve from the Fort McMurray study region described in this thesis. The top panel shows the apparent resistivity as a function of period while the bottom panel shows the phase, each calculated from the complex impedance tensor, (0° rotation). Red and blue curves represent the apparent resistivity calculated from the xy and yx elements of the impedance tensor.

components. The horizontal directions, x and y, are usually chosen to coincide with the

geographic directions North and East. Thus the electric field measured in the North-South

direction is labelled E_x and the East-West electric field E_y, the magnetic field

components have the same naming convention. The measured electric and magnetic

fields are then used to calculate the impedance using equation (2.9). From the impedance,

the apparent resistivity is calculated using equation (2.11) as a function of signal

frequency and is plotted as a curve. Note that only two curves are plotted in Figure 2.1. In

general four apparent resistivity and phase curves, can be calculated, one from each

element in the impedance tensor in equation (2.10).

2.2.1   MT For a One-Dimensional Earth

If the resistivity of the Earth only changes with depth it is said to be 1-D. The horizontal

electric field will be related only to the orthogonal horizontal magnetic field and the

diagonal components of the impedance tensor in equation (2.10), Z_{xx} and Z_{yy}, will be

exactly zero. In addition, the off-diagonal components will be equal in magnitude at all

frequencies, regardless of the azimuthal orientation of the incident wave. The 1-D

impedance tensor can be written in the simple form:

$$\begin{bmatrix} E_x \\ E_y \end{bmatrix} = \begin{bmatrix} 0 & Z \\ -Z & 0 \end{bmatrix} \begin{bmatrix} H_x \\ H_y \end{bmatrix} \qquad (2.14)$$

2.2.2   MT For a Two-Dimensional Earth

In most cases the resistivity structure of the Earth is not one-dimensional and a two or

three-dimensional approach must be taken. In the case of a 2-D Earth, the resistivity

changes both with depth and one horizontal direction, as shown in Figure 2.2:. Equation

(2.14) is not valid if the resistivity of the Earth varies in either horizontal direction, so a

more advanced approach must be used to interpret MT data. The convention is to set the

y-direction as the horizontal direction in which the resistivity changes, so that resistivity

is invariant in the x-direction. This convention means that the x-direction is defined as the

geoelectric strike direction.
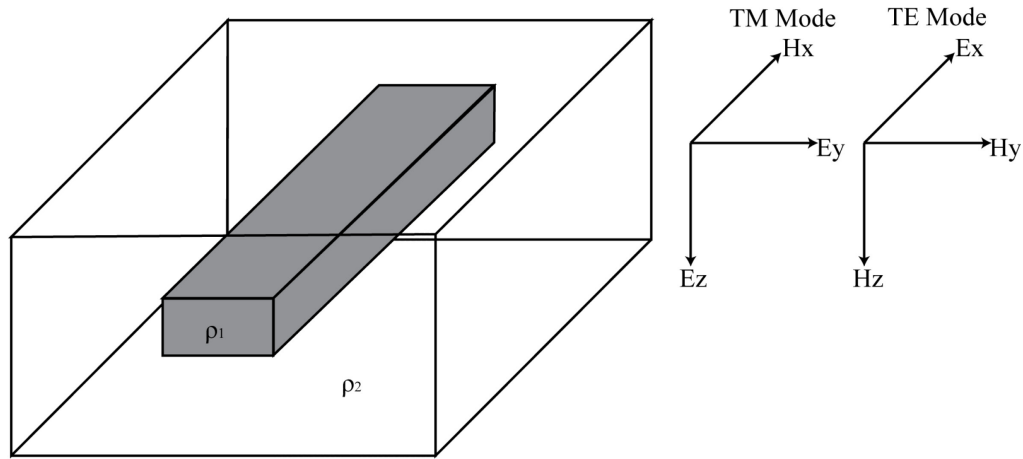
Figure 2.2: Idealized 2-D resistivity structure. The electric and magnetic fields that are associated with the TE and TM mode are shown to the right. The TM mode has electric fields that cross the boundary between resistivities; the TE mode has magnetic fields that cross the boundary. TE and TM will interact differently with the conductor and give different apparent resistivity values.

It can be shown that in the 2-D case, Maxwell's equations decouple into two sets of field components, with each set defined by a field component polarized in the strike direction. In the transverse electric (TE) mode, the electric field is polarized in the x-direction and E_x is related only to H_y and H_z. In the transverse magnetic (TM) mode, the magnetic field is polarized in the x-direction and H_x is related only to E_y and E_z. Each mode corresponds to an impedance tensor element (Z_{xy} and Z_{yx}, respectively) and thus has a separate apparent resistivity curve. In the 2-D case, the impedance tensor takes the form:

$$\begin{bmatrix} E_x \\ E_y \end{bmatrix} = \begin{bmatrix} 0 & Z_{xy} \\ Z_{yx} & 0 \end{bmatrix} \begin{bmatrix} H_x \\ H_y \end{bmatrix} \tag{2.15}$$

The diagonal elements are zero, if the x-direction corresponds to the geoelectric strike direction. If the measurement co-ordinates do not coincide with the strike direction, then all four elements will be non-zero.

14

Determining the strike direction from measured MT data is an important task. Methods that can be used include tensor decomposition, studies of induction vectors and the phase tensor. These will be discussed later in section 2.3.

2.2.3 MT For a 2-D Earth With 3-D Galvanic Distortion

Often MT data analysis requires a decision of whether to proceed with a 2-D or 3-D analysis. An intermediate scenario exists between these two cases if the measured MT data can be shown to be due to a regionally 2-D structure with the 3-D aspects confined to localized, small-scale, features at the surface. If these features are relatively small, then they will distort the electric fields (and impedances) in a frequency independent manner, that is, galvanically.

In the simplest case, only the magnitude of the electric field is changed, causing the calculation of impedance and apparent resistivity to be scaled by a constant factor either upwards or downwards that is called a static shift (Jones, 1988).

Groom & Bailey (1989) suggested that the measured electric field E could be represented by a linear superposition of the regional, E_R, and a distortion factor. In matrix form, the regional field is acted upon by a 2 x 2 distortion tensor D uniformly at all frequencies (Caldwell et al., 2004):

$$\begin{bmatrix} E_x \\ E_y \end{bmatrix} = D \begin{bmatrix} E_x \\ E_y \end{bmatrix}_R = \begin{bmatrix} d_{11} & d_{12} \\ d_{21} & d_{22} \end{bmatrix} \begin{bmatrix} E_x \\ E_y \end{bmatrix}_R \qquad (2.16)$$

Galvanic distortion can be a problem in MT analysis because it affects all frequencies, so data may appear undistorted. It is not possible to know initially whether any shift has occurred at all. Comparison with nearby MT stations or with alternative methods, such as time domain EM, is often the only way to determine if galvanic distortion is present.

More generally, galvanic distortion can change the direction of the electric fields as well as the magnitude. The distortion acts on the 2-D impedance tensor and results in all four elements being non-zero. Groom & Bailey (1989) presented an analysis method that assumed a 2-D regional resistivity structure locally distorted by 3-D effects. The 3-D effects can be represented by a tensor $\boldsymbol{C}$ that is a combination of four specifically identified types of distortion:

$$\boldsymbol{C} = g\boldsymbol{TSA} \tag{2.17}$$

The galvanic scaling factor g, discussed above, acts on the tensors $\boldsymbol{T}$ (twist), $\boldsymbol{S}$ (shear), and $\boldsymbol{A}$ (local anisotropy). The conductivity anomaly can twist the telluric currents towards its local strike direction; this is called the twist tensor. The shear tensor deflects the EM fields so that they are no longer orthogonal to one another, thereby increasing the diagonal values of the impedance tensor. Anisotropy is not necessarily a source of distortion but in the case of equation (2.17) anisotropy is ascribed to local heterogeneities that can polarize the electric field along the anisotropic strike direction, but it does not change the direction of the telluric currents (Simpson & Bahr, 2005).

2.2.4 Three-Dimensional Earth

A three-dimensional Earth has resistivity changes in both horizontal directions and also vertically. A 3-D impedance tensor will have non-zero values in all four elements of equation (2.10) regardless of the co-ordinate system in which it is plotted. This is the most complex, and general, case. In a three-dimensional Earth, separate TE and TM modes do not exist, as Maxwell's equations cannot be decoupled; analysis must include the full impedance tensor at all frequencies.

It should be noted that electrical anisotropy (direction dependant resistivity) is a further generalization of the above resistivity structures. Electrical anisotropy is capable of

making the impedance tensor appear to be of a higher dimensionality that it is and can severely complicate MT analysis. Anisotropy is a complicated concept in magnetotellurics and will be discussed later in this chapter.

2.3   Dimensionality of Magnetotelluric Data

It is important to be able to determine the dimensionality and directionality of measured MT data. The following section describes some methods that are commonly used to determine the dimensionality and strike direction.

2.3.1   Tensor Decomposition

Groom & Bailey (1989) described a method in which the 2-D geoelectric strike direction can be estimated from measured MT data. This method assumes that a 2-D impedance tensor exists and that a real matrix, corresponding to frequency independent distortion, distorts it. The Groom-Bailey (GB) strike angle contains an inherent 90° ambiguity, and therefore will be either parallel or orthogonal to the true strike of the resistivity structure. This inherent non-uniqueness can be overcome by using additional geological or geophysical data to find the true strike direction.

2.3.2   Induction Vectors

The induction vector (IV) is calculated from the ratio of the vertical magnetic field H_z and each of the horizontal magnetic field values (H_x and H_y). IVs are useful in determining strike directions because they have directional information and can point out conductors. The induction vectors points towards conductors when plotted in the Parkinson convention (Parkinson, 1959) and away from conductors in the Wiese convention (Wiese, 1962). In a 2-D situation the induction vectors are perpendicular to the strike direction, so this property can be used to resolve the 90° ambiguity described

above. If there is no horizontal gradient in resistivity, the induction vectors will have a very small magnitude. The components of the IV are sometimes called the "tipper" because the non-zero vertical component of the local magnetic field tips the total magnetic field away from the horizontal plane. In map view an IV will have two components, North-South and East-West. If the Earth is approximated as two-dimensional and invariant in the x-direction, then only the y-component will be non-zero. The example in Figure 2.3 shows how the induction vector can be used to determine the geoelectric strike; the vectors are aligned orthogonally to the strike of the conductor.
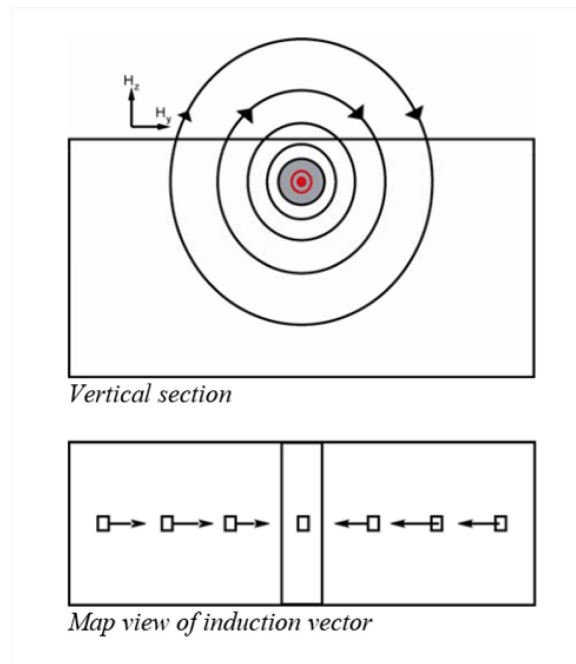
Figure 2.3: Induction vector visualization for a two-dimensional Earth. The shallow conductor creates magnetic fields that deflect Earth's magnetic field (top). The directions of the arrows reflect the location of the conductivity anomaly, in this example they are plotted in Parkinson convention, pointing towards the conductor (bottom). Figure from (Unsworth, 2014).

2.3.3   Phase Tensors

The phase tensor was introduced by Caldwell et al., (2004) and can be useful for determining the dimensionality and strike of MT data. The phase tensor makes no assumption whatsoever about the regional dimensionality and therefore is applicable even with data caused by a 3-D resistivity structure (Caldwell et al., 2004). It is defined as the ratio between the real and imaginary components of the complex electrical impedance tensor:

$$\boldsymbol{\Phi} = \left(\frac{\text{Re}(\boldsymbol{Z})}{\text{Im}(\boldsymbol{Z})}\right) = \begin{pmatrix} \varphi_{11} & \varphi_{12} \\ \varphi_{21} & \varphi_{22} \end{pmatrix} \tag{2.18}$$

If the Earth has a one or two-dimensional resistivity structure, then both the real and imaginary components of the impedance tensor are anti-diagonal. From the definition of the phase tensor in equation (2.18) it can be seen that that the anti-diagonal elements of the impedance tensor are used to calculate the diagonal components of the phase tensor, therefore the principal phase tensor elements are φ_{11} and φ_{22}. The measured impedance $\boldsymbol{Z}$ is complex and therefore can be represented the form $\boldsymbol{Z} = X + iY$, similarly the regional impedance is $\boldsymbol{Z}_R = X_R + iY_R$. The phase tensor is unaffected by galvanic distortion of the electric field and represents the unchanged, regional phase relationship between the electric and magnetic fields. If the distortion tensor ($\boldsymbol{D}$) from equation (2.16) is applied to the regional impedance $\boldsymbol{Z}_R$ then we have:

$$\begin{aligned} \boldsymbol{\Phi} &= X^{-1}Y = (\boldsymbol{D}X_R)^{-1}(\boldsymbol{D}Y_R) \\ &= X_R\boldsymbol{D}^{-1}\boldsymbol{D}Y_R = X_R^{-1}Y_R \\ &= \boldsymbol{\Phi}_R \end{aligned} \tag{2.19}$$

Thus the regional and distorted phase tensors are identical and galvanic distortion does not affect the phase tensor. Near surface, local conductivity heterogeneities can affect MT

data by distorting the incoming electromagnetic wave but as long as the regional electric field (that which would be recorded in the absence of all distortion) is largely constant over the extent of the heterogeneity then phase relationship is preserved (Caldwell et al., 2004). This is the basis of using the phase information of the measured EM fields.

There are three variables that define the phase tensor, they can be used to graphically display it as an ellipse: the magnitudes of φ_{max} and φ_{min}, and the skew angle β. The two angles are defined as the largest and smallest values of the diagonal elements of the phase tensor. The skew angle is a measure of the asymmetry of the phase tensor and defined as:

$$\beta = \frac{1}{2} tan^{-1} \left(\frac{\varphi_{12} - \varphi_{21}}{\varphi_{11} + \varphi_{22}} \right) \tag{2.20}$$

A 1-D or 2-D anti-diagonal impedance tensor will result in a purely diagonal phase tensor and the elements φ_{12} and φ_{21} will equal zero, resulting in a skew angle of zero. The skew alone is not capable of distinguishing 1-D and 2-D resistivity structures. If the elements φ_{12} and φ_{21} have the same magnitude the skew will be zero but the impedance tensor may have higher dimensional qualities. A low skew is a common, but not a diagnostic, characteristic of low-dimensional resistivity structure (Heise et al., 2006).
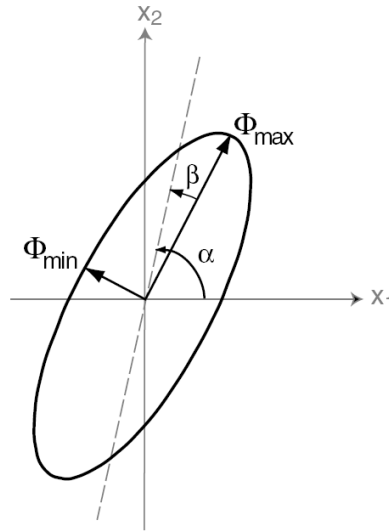
Figure 2.4: The phase tensor as represented by an ellipse. The three coordinate frame independent parameters used to define the ellipse are implicit in the phase tensor formalization. The major and minor axes are the singular values of the tensor and the skew β is a constant shift reflecting a departure from symmetry in $\boldsymbol{\Phi}$ and therefore toward high dimensionality. The angle α-β is the orientation of the major axis of the ellipse and is coordinate frame dependent. From Caldwell et al., (2004).

The graphical visualization of Caldwell et al., (2004)'s phase tensor is presented in Figure 2.4. The major and minor axes of the phase tensor are the values on the diagonal of the diagonal matrix found from decomposing phase tensor matrix by way of singular value decomposition (SVD) and are simply the largest and smallest of the diagonal components post-decomposition. The comparison of φ_{max} and φ_{min} can distinguish between one and two-dimensional impedance data in because 1-D structure will cause identical φ_{max} and φ_{min} values and the ellipse will be a circle. If the Earth resistivity appears different in the two orthogonal directions the phase tensor will plot as an ellipse with ellipticity a function of the split between φ_{max} and φ_{min}.

The orientation of the ellipse is determined by the angle α, which is reference frame dependent, and the phase tensor skew β. For undistorted data, α is related to regional 2-D

geoelectric strike and the semi-major axes of the ellipse will be identical in magnitude to the traditional impedance tensor phase from equation (2.12) and (2.13) (Caldwell et al., 2004). The direction of φ_{max} is the direction of maximum inductive current flow which means that the major axis of the ellipse will orient *perpendicular to the highly conductive direction* (Heise et al., 2006).
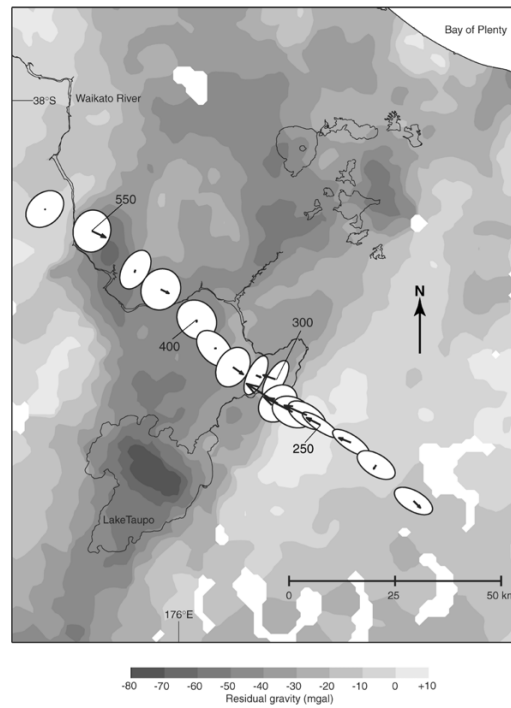
Figure 2.5: Phase tensor ellipses computed at a period of 21.3 s crossing an extension zone filled with conductive volcaniclastic sediments in the Taupo Volcanic Zone, New Zealand. Real-part induction vectors and a regional gravity anomaly map are plotted as well. From Caldwell et al., (2004).

The orientation of the phase ellipses plotted on a map will change by 90° when crossing a resistivity interface. An example, phase tensors for an MT profile crossing a graben structure is shown in Figure 2.5. The phase tensors point perpendicular to one another on either side of the interface and are circular at greater distances from the contact, which is indicated by the "300" label in Figure 2.5.

2.3.4   Summary

Several methods to determine the dimensionality of measured MT data and its directionality have been discussed in this section. The Groom-Bailey tensor decomposition assumes that a 2-D resistivity structure is present and that the measured impedance tensor is a combination of a 2-D impedance tensor with galvanic distortion. The rotation angle at which that model (2-D tensor plus distortion) fits the measured 2-D data is termed the Groom-Bailey (GB) strike angle. The GB strike contains an inherent 90° ambiguity, and induction vectors can help to resolve the ambiguity because they always orients parallel to resistivity gradients, perpendicular to strike. The phase tensor also yields a strike angle, related to the direction at which there is a maximum phase split.

2.4   Anisotropy in Magnetotellurics

Anisotropy describes a physical property of a material, which has different values in different spatial directions. Electrical anisotropy is believed to be common in the basement rocks of Alberta (Boerner et al., 2000). An electrically anisotropic rock will have different resistivities in each direction, which can in general be arbitrarily oriented.

The impedance tensor recorded at an MT station will be influenced by the presence of electrical anisotropy in the underlying rocks. Because MT is a diffusive technique, its resolution decreases with increasing depth of investigation in the Earth. It is impossible to determine from MT data alone whether inferred anisotropy is intrinsic (present at the molecular level) or on a larger spatial scale that is below the resolution of MT at that depth.

This section will present some synthetic resistivity models and describe the MT data generated by each. In each case, the equivalent isotropic structure is included for

comparison. It will also examine what evidence can be used to determine if MT data is detecting an anisotropic Earth.

The figures presented below show the forward solution i.e. what MT data are predicted for a given resistivity model. Often in geophysics we are solving the inverse problem and trying to understand what resistivity structure is present, based on the measured MT data. The inverse problem, where resistivity structure is determined from measured MT data, is discussed in Chapter 6.

2.4.1   One-Dimensional Resistivity With Anisotropic Basement

The first example is a simple two-layer Earth model with a 2000 Ωm layer underlain by a 5 Ωm basement at 10 km depth. In the isotropic case the basement has a resistivity of 5 Ωm in all directions and in the anisotropic case the y-direction is 2000 Ωm. The coloured stripes indicate the orientation of the conductive direction, which in this case is parallel to the x-axis. These values are chosen to match the anisotropic study by Heise & Pous (2001) which will be discussed in the next section. A forward calculation using the code of Pek & Verner (1997) was used to calculate the predicted MT response in the period range 0.001-1000 s. The calculated MT responses are presented as pseudosections, station versus signal period (Figure 2.6 and Figure 2.7).

Model-1 is isotropic and one-dimensional; the xy and yx apparent resistivity and phase data are identical at all MT stations and all periods. At periods less than 0.1 s the apparent resistivity does not vary with period and the phase is 45°, as expected. When the conductive basement is sampled at periods greater than 0.1 s, the apparent resistivity values decrease and the corresponding phase rises above 45°. At all points on the pseudosection the tipper magnitude is exactly zero because there are no changes in subsurface resistivity in the y-direction. The phase tensor ellipses in model-1 are circular

because there is no xy/yx split, and have a skew of $0°$ because the impedance tensor (and

thus the phase tensor) is symmetric.
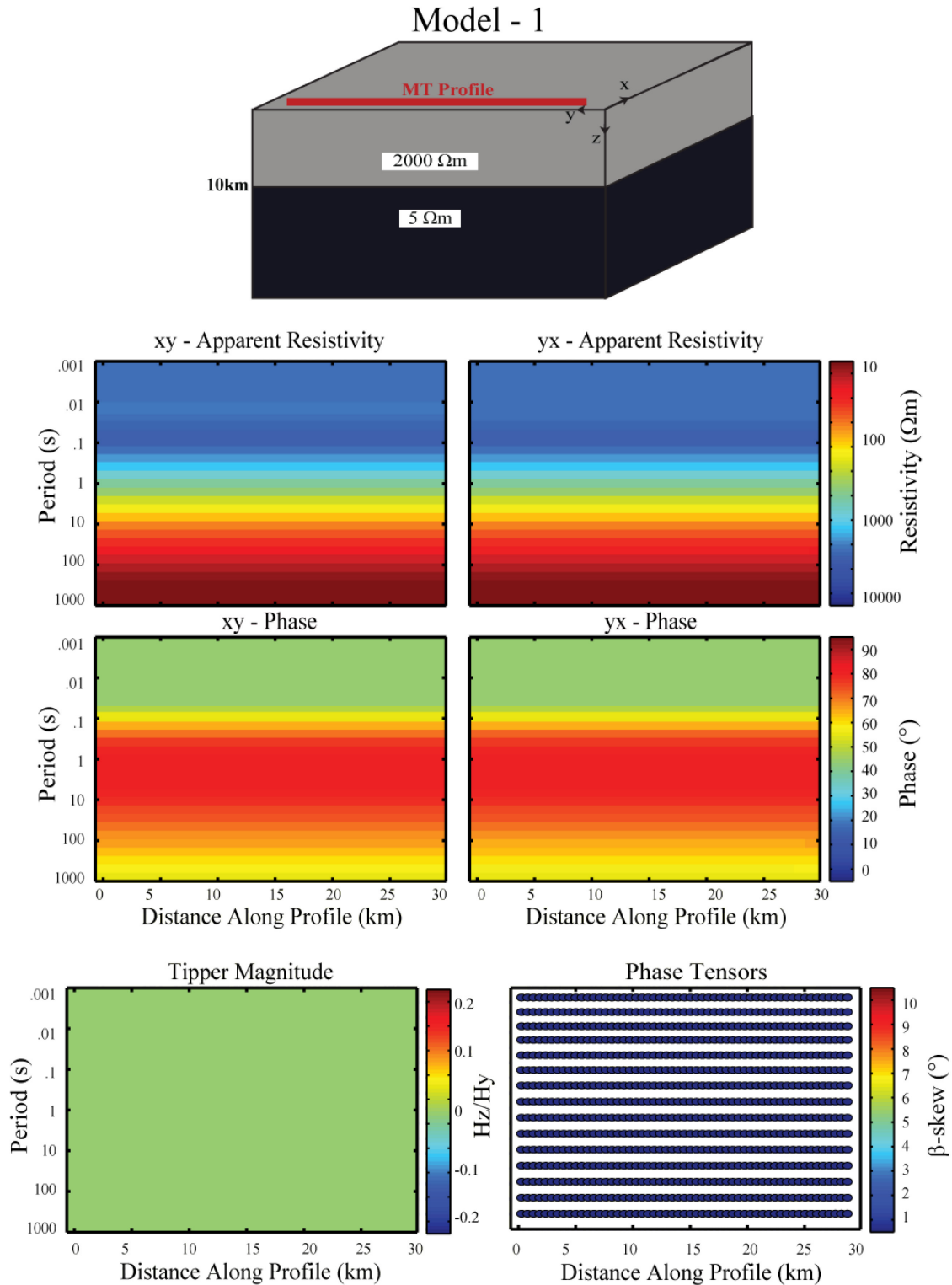
Figure 2.6: Pseudosection results of, Model-1, for a 1-D earth with a conductive basement. The orientation of the MT profile is indicated in red. The upper group of four pseudosections are the apparent resistivity and phase of the xy and yx impedance tensor elements. Tipper magnitude is the ratio between the vertical magnetic field H_z and the in-profile horizontal component H_y.

Model-2 is shown in Figure 2.7, and is identical to Model 1, except that the basement layer is now anisotropic. In the basement, the resistivity in the x-direction is 5 Ωm and the resistivity in the y-direction is 2000 Ωm. The difference between model-1 and model-2 can be seen in the xy data, an interface is only visible in the yx data, since the resistivity in the x-direction is the same at all depths. The large difference between the xy and yx data in model-2 shows that there is an azimuthal dependence in the measured data; direction matters even though the resistivity structure is only 1-D. The tipper is uniformly zero in magnitude because there is no change in the resistivity structure in the y-direction.

The effect of anisotropy in the phase tensor pseudosection begins at a period of 0.1 s where the ellipses orient themselves perpendicular to the conductive direction, in map-view the ellipses align along the x-axis. The degree of ellipticity is relatively constant over the period range 0.1-10 s. Note that because there is no lower interface to the anisotropic basement layer, the phase tensors never change orientation and point in the orthogonal direction as they do in Figure 2.5. The orientation of the phase ellipses line up with the axis of anisotropy. In this example the phase tensors are able to define the direction of the resistivity fabric of the Earth that is not known ahead of time.
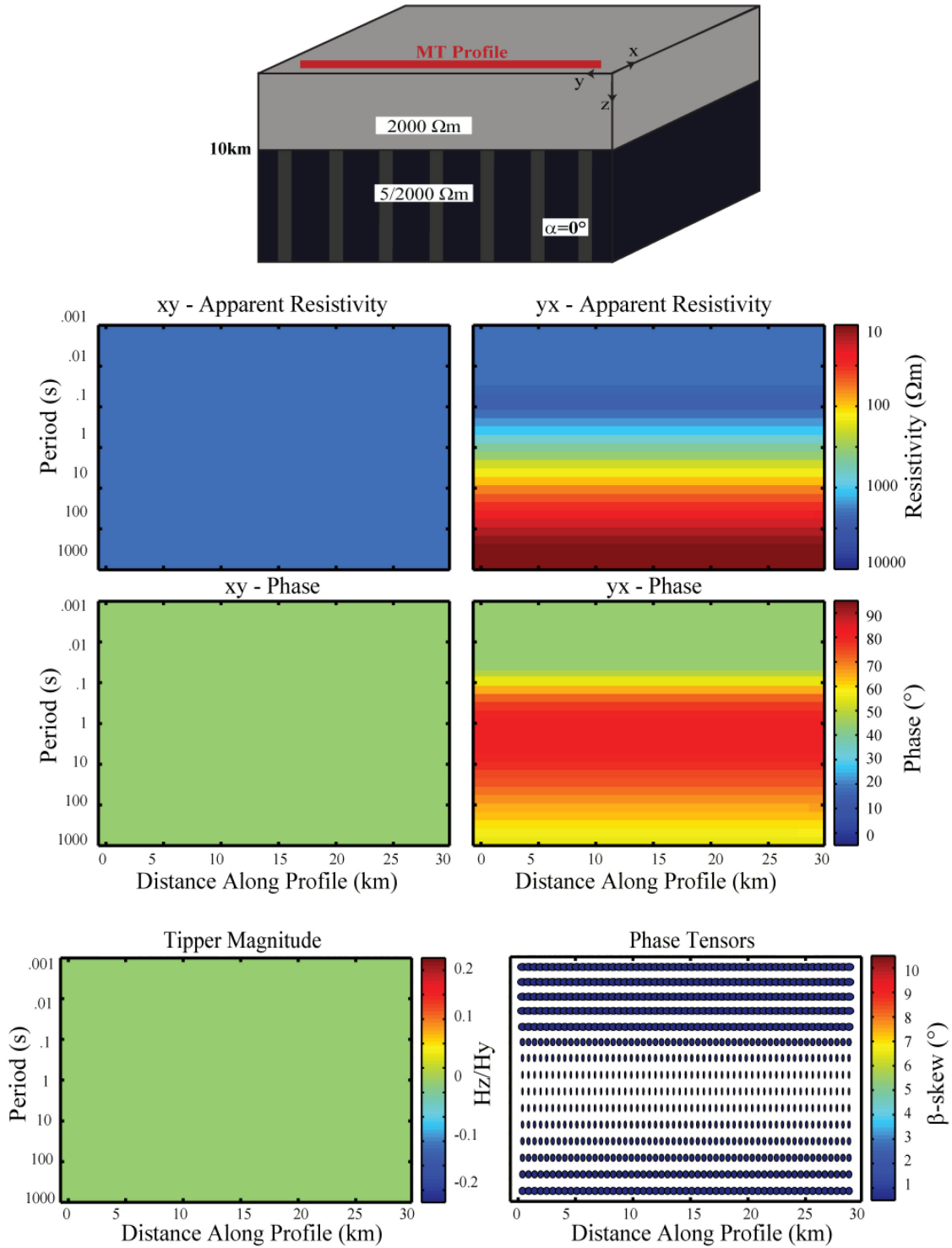
Figure 2.7: Pseudosection results of, Model-2, for a 1-D earth with an anisotropic basement. The orientation of the MT profile is indicated in red. The upper group of four pseudosections are the apparent resistivity and phase of the xy and yx impedance tensor elements. Tipper magnitude is the ratio between the vertical magnetic field H_z and the in-profile horizontal component H_y.

These data can be used to infer electrical anisotropy because of the large split between the xy and the xy apparent resistivity and phase data, combined with the low magnitudes observed in the tipper pseudosection. The 2-D structure in Figure 2.2 would also create a large phase split, but stations on either side of the prism would have large magnitude induction vectors that point towards the prism, orthogonal to its strike.

The phase tensor pseudosection is also included in Figure 2.7. Note that the skew is zero for at all stations and periods in this example. A 1-D Earth will always have a symmetric phase tensor, and thus a skew value of zero.

2.4.2   One-Dimensional Resistivity With Anisotropic Layer

Model-3 and Model-4 are slightly more complicated than Model-1 and Model-2. They are still 1-D but include 3 layers as shown in Figure 2.8 and Figure 2.9. Model-3 is isotropic so the xy and yx data have the same values at all periods and the tipper magnitude is zero everywhere. The phase tensor is perfectly symmetric (skew = 0º), and because there are no phase splits the ellipses are circular at all periods and stations.
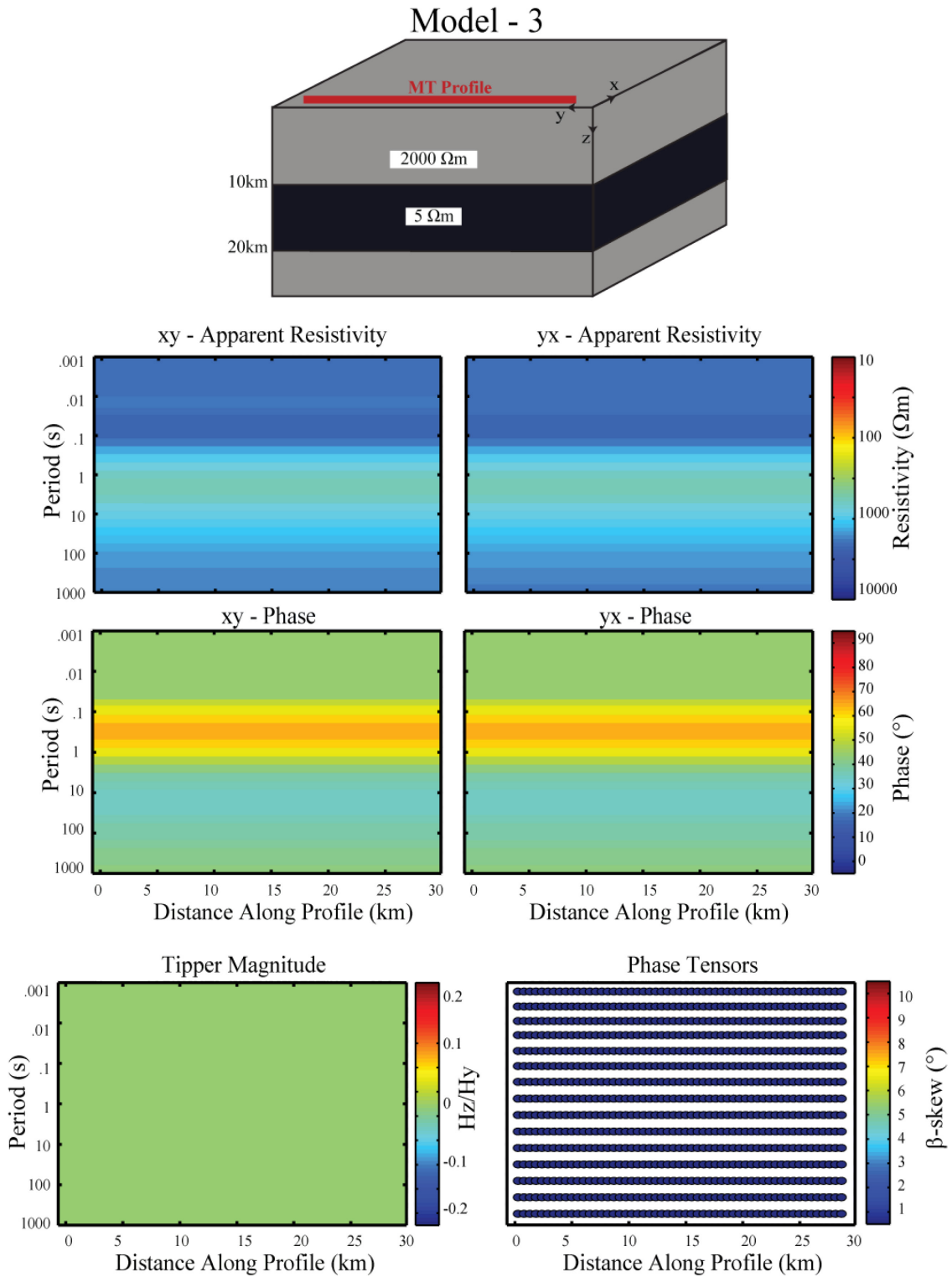
Figure 2.8: Pseudosection results for Model-3, for a 1-D earth with conductive layer 10 km thick at 10 km depth. The orientation of the MT profile is indicated in red. The upper group of four pseudosections are the apparent resistivity and phase of the xy and yx mode. Tipper magnitude is the ratio between the vertical magnetic field H_z and the in-profile horizontal component H_y.
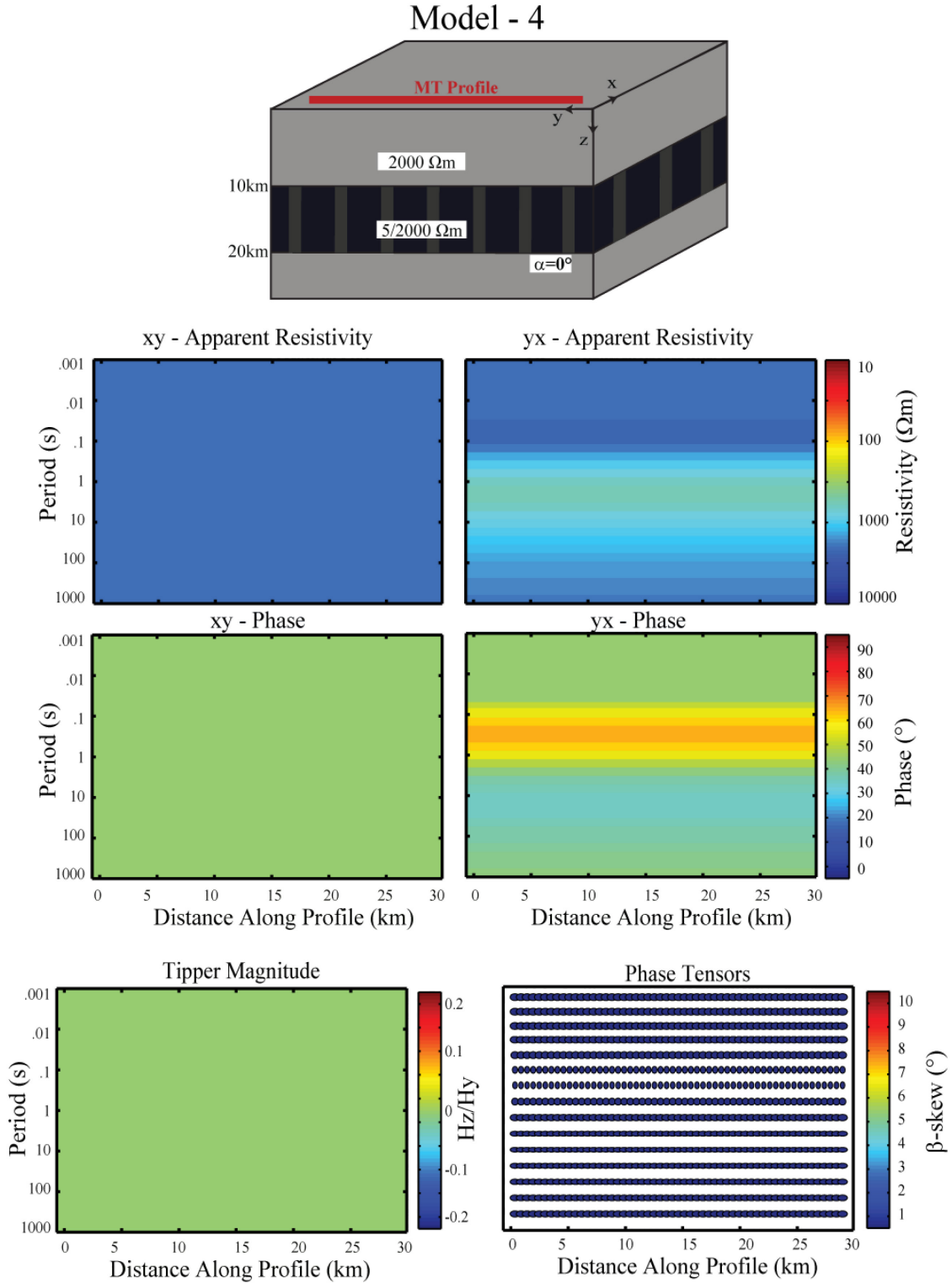
Figure 2.9: Pseudosection results for Model-4, for a 1-D earth with an anisotropic layer, conductive direction aligned with the x-direction. The orientation of the MT profile is indicated in red. The upper group of four pseudosections are the apparent resistivity and phase of the xy and yx mode. Tipper magnitude is the ratio between the vertical magnetic field H_z and the in-profile horizontal component H_y.

Figure 2.9 shows Model-4, which is a 1-D model with an anisotropic middle layer. In Model-4 the split between the xy/yx apparent resistivity data is not nearly as noticeable as the split between the xy/yx phases. This is because the phase generally has values only between 0° and 90°, meaning that some features may be visible in phase perturbations that are smoothed out by the large values of the apparent resistivity, even when plotted logarithmically. Another useful quality of the phase is that it can be thought of as a derivative of the apparent resistivity with period (as shown in section 2.2). The phase can detect these interfaces very effectively because the rate of change of ρ_a will fall off quicker than the actual value of ρ_a.

There is a slight change in the ellipticity of the phase tensor ellipses in Model-4. The ellipses are first polarized perpendicular, and then parallel to, the conductive direction of the anisotropic layer in Model 4. This response is quite subtle, and would likely not be discerned in field MT data containing realistic amounts of noise. It would be challenging to use phase tensor analysis to make a convincing argument for the existence of an anisotropic layer with these data. Even though the layer is quite thick (10 km) and has an anisotropic resistivity ratio of 400, the anisotropy only produces a small effect in the phase tensor pseudosection. The phase split associated with the anisotropic layer is not large enough to cause very strong ellipticity.

2.4.3   Two-Dimensional Resistivity With Anisotropic Prism

The model is made two-dimensional by adding horizontal bounds to the layer, making it a conductive prism, as shown in Model-5 (Figure 2.10). Since the resistivity structure is two-dimensional, the TE and TM modes can be defined in a meaningful way. The TE mode is defined as being derived from the xy impedance tensor element and the TM mode is derived from the yx data. In the TE mode, the horizontal electric field is E_x,

which drives currents in the conductive prism that never cross resistivity boundaries. The TM mode is associated with the electric field E_y, which means that electric currents cross resistivity boundaries of the conductor (travelling in the y-direction) and charges build up on the boundary surfaces adding a galvanic (frequency independent) effect to the inductive effect. The surface charges in the TM mode make it difficult to detect the bottom of the prism and the feature is spread out vertically. The TE mode is generally more effective at detecting conductors than the TM mode but is unable to detect resistors because currents are more difficult to drive in them. The TM mode includes the currents crossing the boundary into the resistor, which is detectable in the galvanic portion of the TM response.

The tipper has a large magnitude on either side of the conductor and changes sign in the centre of the conductor. The phase tensor response for Model-5 is similar to the example shown in Figure 2.5: ellipticity increases in response to the phase split between the TE and TM modes, aligning first perpendicular, then parallel to the conductive direction as the period decreases and detects the base of the prism. The resistivity of the Earth is isotropic and two-dimensional in Model-5 so the phase tensor skew is still 0º.
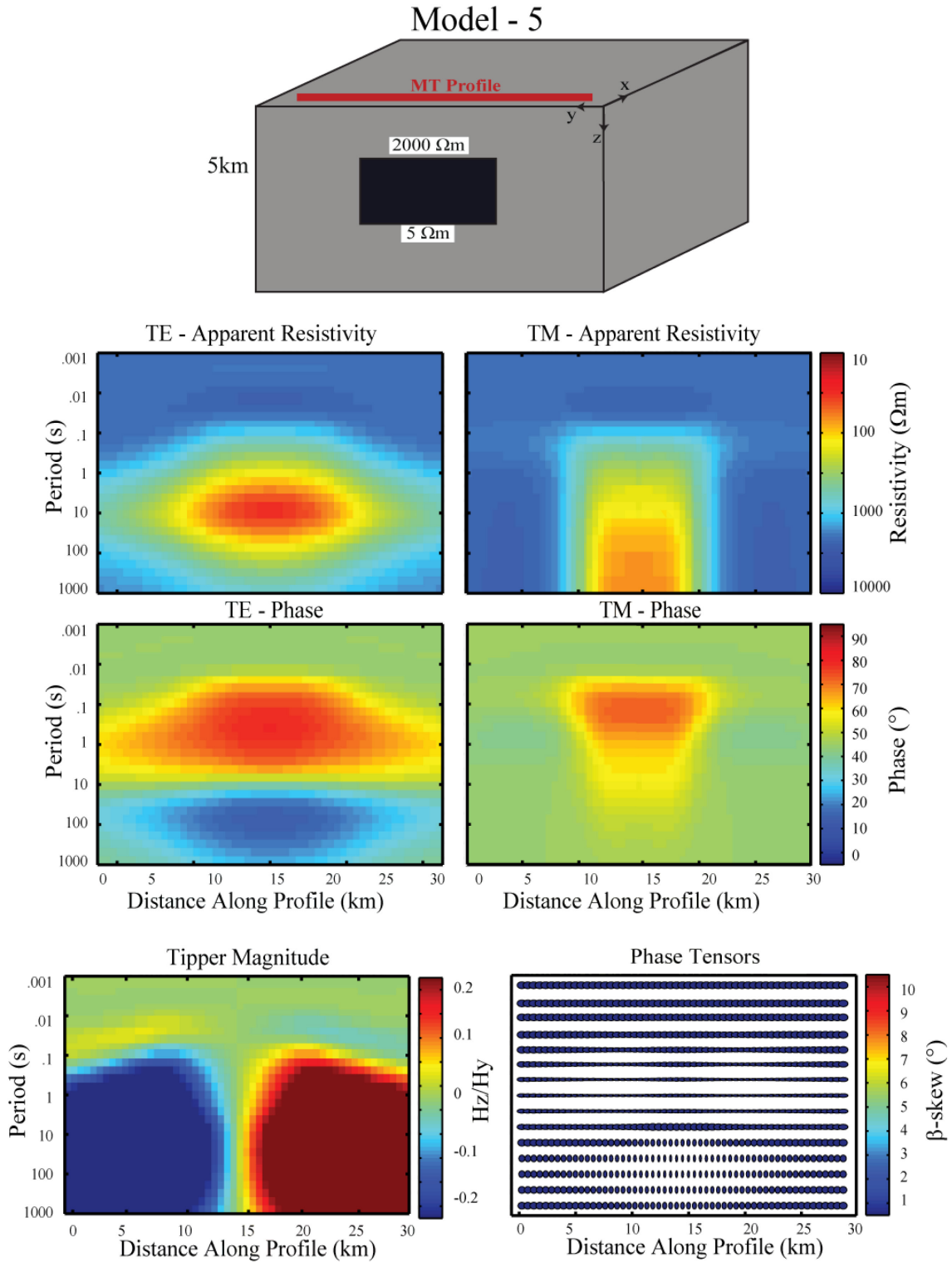
Figure 2.10: Pseudosection results for Model-5, for a 2-D earth with a conductive prism 5 km thick at 5 km depth. The orientation of the MT profile is indicated in red. The upper group of four pseudosections are the apparent resistivity and phase of the TE and TM mode. Tipper magnitude is the ratio between the vertical magnetic field H_z and the in-profile horizontal component H_y.

The prism is made anisotropic in Model-6. The direction of anisotropy is defined to be non-parallel to the 2-D strike of the prism; this extra complexity simulates the situation often found in field MT data. A visualization of the prism with both 2-D and anisotropic strike is included in Figure 2.10. There are now two separate strike directions present in the model, (a) the strike of the prism (parallel to the x-direction) and (b) the strike of the conductive direction represented by the variable α_s. In this case $\alpha_s = 40°$ measured clockwise from the x-axis. The anisotropic results for resistivity and phase are similar to the results for the isotropic prism but smaller in magnitude.

The induction vectors for the anisotropic model shown in Model-6 react similarly to the isotropic case but with much smaller magnitude. Without the phase tensor information the anisotropic model-6 appears to be a simple conductive prism, but with a lower conductivity than the one in Model-5.

The phase tensor pseudosection is the key to identifying the presence of anisotropy and interpreting the structure correctly. Large skew values appear at the frequencies and stations that are affected by the prism. The interaction of the two strike directions (2-D and anisotropic) changes the direction of the electric current in such a way that the phase tensor becomes very asymmetric and the skew rises to higher than 10° (a skew of only 3° has been thought to imply 3-D structure, (Heise et al., 2006)). The azimuth of the major axis of the phase ellipses in this example is parallel to the anisotropy strike just above the high skew block before returning to near circular form at longer periods. The azimuths of the phase tensors are not nearly as strongly oriented as in the case of the anisotropic basement in Model-2 (Figure 2.7), the prism creates high skew phase tensors but does not cause consistent azimuths. The phase tensor ellipses also do not have as strong ellipticity as they did for Model-5. It is clear from this example that MT data with high phase tensor

skew need not necessarily be interpreted at 3-D. An asymmetric phase tensor may be caused either by 3-D distortion or by anisotropic, but fully 2-D, structure.

These examples show how anisotropy can be hidden in MT data that can appear to be isotropic, and that the phase tensor can be a valuable tool for anisotropic analysis. The next section will examine how the phase tensor in particular responds to a variety of anisotropic structures.
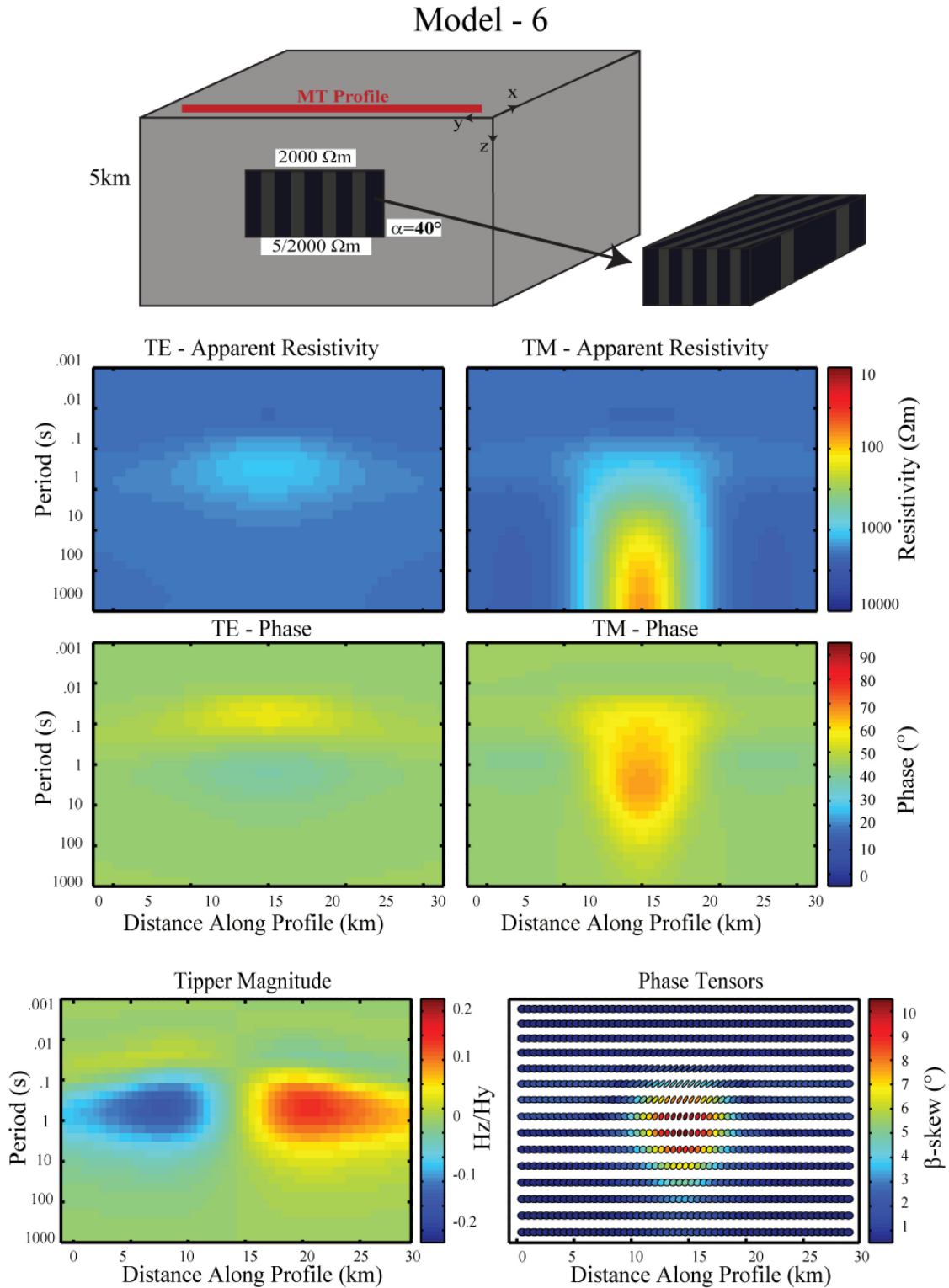
Figure 2.11: Pseudosection results for Model-6, for a 2-D earth with an anisotropic prism with anisotropic strike aligned 40° clockwise from the x-direction. The orientation of the MT profile is indicated in red. The upper group of four pseudosections are the apparent resistivity and phase of the TE and TM mode. Tipper magnitude is the ratio between the vertical magnetic field H_z and the in-profile horizontal component H_y.

2.5 Detecting Electrical Anisotropy from MT Data

The previous section showed examples of MT data calculated for a range of isotropic and anisotropic resistivity models. This represents the solution of a forward problem in geophysics. In practical MT exploration, the opposite analysis is required and MT data is used to infer the resistivity structure of the subsurface, i.e. an inverse problem. This section describes characteristics of MT data that can give evidence for anisotropy. These will be used in Chapter 7 to investigate if anisotropy is present in field MT data from the study area near Fort McMurray in Alberta.

2.5.1 Anisotropic data in Isotropic Inversions

Two-dimensional isotropic MT data analysis uses only the off diagonal elements of the impedance tensor (equation (2.15)). The implicit assumption in 2-D analysis is that any non-zero values in the diagonal components are due to noise or localized distortion and are not representative of the regional resistivity structure. The previous section has shown that that assumption is not always correct if the Earth is electrically anisotropic. If the MT data is indeed due to the presence of anisotropic resistivity structure, then half of the impedance tensor data is being ignored in the inversion.

Heise & Pous (2001) showed that inversion of MT data influenced by an anisotropic structure with a 2-D isotropic inversion code could produce serious artefacts in the resulting 2-D model. The authors used the simple model illustrated below to demonstrate this point. The model has a resistive layer overlying an anisotropic basement halfspace, with conductive/resistive ratio of 2000 Ωm to 5 Ωm, beginning at 20 km depth with the anisotropic strike pointing into the page. Figure 2.12 is the result of the isotropic inversion and shows alternating conductive and resistive dikes oriented along the anisotropic axis.
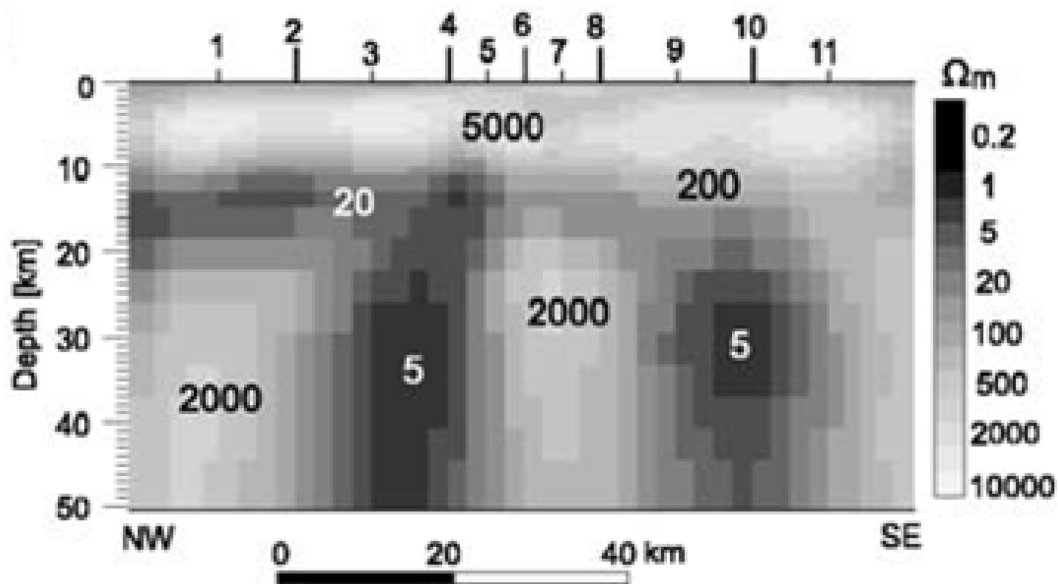
Figure 2.12: Result of an isotropic inversion of anisotropic data with resistivity contrast 2000 Ωm to 5 Ωm. Vertical dyke structures are inserted into the model when none exist in the data used to generate the forward model. From Heise & Pous (2001).

If the anisotropy ratio is greater than five, the 2-D inversion recovers the original model with anisotropy, provided that the data are rotated in the direction of the anisotropy strike or to an angle within a band surrounding it (Heise & Pous 2001). Artefacts arise when anisotropic MT data is treated as being due to an isotropic Earth. The isotropic inversion code cannot reproduce the true, intrinsically anisotropic, nature of the data and instead simulates macro-anisotropy with these long vertical dikes. If vertical features such as these dikes seem an unlikely structure for the study region then the presence of anisotropy can at least be suspected.

2.5.2   Anisotropy and the Phase Tensor

Heise et al., (2006) used phase tensors to try and distinguish between isotropic and anisotropic structure in MT data, and the results are summarized in Figure 2.13. The

degree of ellipticity, orientation, and apparent resistivity curves for each scenario were presented but it should be noted that the phase tensor skew β was not considered.

In panels (a) - (f) of Figure 2.13 the interface is always between a 1000 Ωm isotropic region and an anisotropic region with conductivities of 20 Ωm and 1000 Ωm oriented in the x and y directions. Figure 2.13 (g) has an oblique anisotropy strike and has rotated the MT impedance tensor to be in line with the phase tensor azimuths of the right hand panel, x'' and y''.

Anisotropy on its own is not capable of creating phase splits or changing the azimuth of phase tensors, as evidenced by Figure 2.13 (a) and (b). Images (c) and (d) show that large phase splits can be produced from the interaction between an anisotropic and an isotropic halfspace; the phase split is either above or below 45° depending on whether the anisotropic or the isotropic medium makes up the basement. In either case the phase split only gently decreases and the ellipse trends towards a circle at long periods.

When the anisotropic region is a layer as in (e) the phase split changes direction when the bottom of the layer begins to be included in the skin depth, at this point the phase tensor changes orientation by 90°. If dip is introduced to the anisotropy in addition to strike, the azimuth is unaffected but the phase split becomes somewhat less pronounced. This is because the z-direction resistivity is, to a certain degree, affecting both the modes and muting the splitting effect.

Image (g) illustrates a very complicated situation and includes a dip and slant factor to the orientation of the anisotropy. The direction of φ_{min} picks out the most conductive direction, which in this case is the projection of the conductive anisotropic direction into the horizontal plane although the phase split is not especially large.
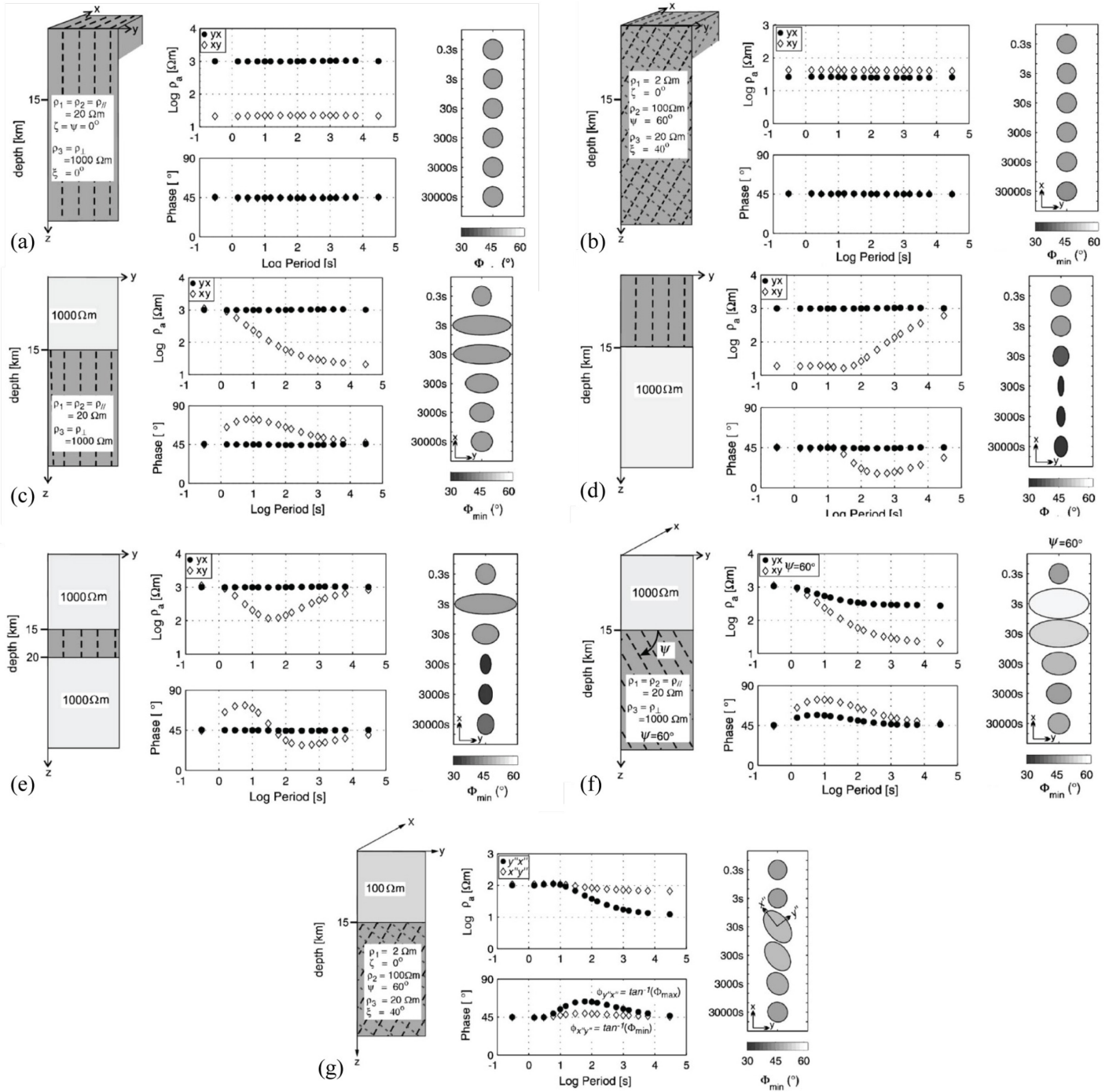
Figure 2.13: Modified from Heise et al., (2006). Forward models on the left of each image have produced the apparent resistivity and phase responses in the middle panels, and the phase tensors in the right panels. Image (*g*) has the apparent resistivity and phase response AFTER rotation and alignment to the phase tensor azimuth axes. Shading of phase tensors does not represent skew value, but rather the value of φ_{max} and is thus related to the amount of phase split (ellipticity).

2.5.3   Out of Quadrant Phase

For a 2-D Earth Weidelt & Kaikkonen (1994) showed that the TE and TM mode phases generally lie between 0 - 90° (1st quadrant). It is possible, however, to have impedance phases plot out of their natural quadrant (OOQ) in extreme cases like the ocean/coastline contrast or for a bounded shallow conductor interacting with a resistive outcrop (Selway et al., 2012). These are cases in which the projection of the local electric field becomes reversed from the direction of current density (Wannamaker, 2005).
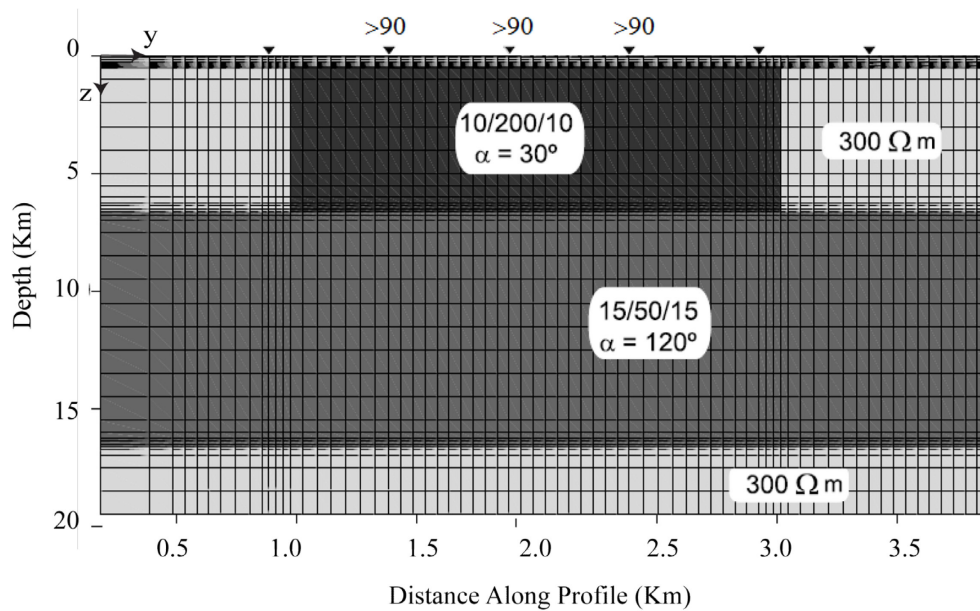
Figure 2.14: From Heise & Pous (2003). 2-D anisotropic model used to create higher than 90° phase in stations places above the shallow block, marked by "> 90". Regional 2-D strike set to 0° (into page). Numbers represent anisotropic resistivity values in directions following the pattern X/Y/Z. The angle α represents the clockwise rotation of the anisotropic axes from the 2-D axes.

Heise & Pous (2003) showed that anisotropy is capable of producing magnetotelluric phase values that are outside of the quadrants defined above. The authors performed a forward calculation from the complicated anisotropic model in Figure 2.14 and were able to explain their distorted resistivity curves and out of quadrant phase. The model

consisted of a shallow anisotropic block, embedded within a 2-D Earth, overlying an anisotropic layer with a nearly orthogonal anisotropy strike to the block's anisotropy strike; neither anisotropic strike was parallel to the regional geoelectric strike (into the page in Figure 2.14).

 In the study region only a small number of central sites of a long profile exhibited OOQ phase and the anisotropic interpretation was corroborated by the presence of outcroppings of macro-anisotropic schists and graphite bearing blackschists nearby. An increase in induction vector magnitude near the edge of the shallow block is predicted by the forward model (Heise & Pous, 2003).

More recently it was shown by Pek et al., (2012) that complicated anisotropy is not strictly necessary to create OOQ phase from a 2-D resistivity structure. An outcropping anisotropic block embedded within a 2-D isotropic halfspace, with sufficiently different regional strike than the block's anisotropy strike, will create the OOQ phase. This is due to the current channelling at the contact between isotropic and anisotropic media. If the MT data are displayed in a co-ordinate system with azimuth *between the regional and anisotropic strikes* then no anomalous behaviour is observed. This means that, in a 'Pek-like' anisotropic region, the rotation band over which OOQ phase is observed can be used to determine the vales of both the 2-D and the anisotropic strike.

An example of this phenomenon is shown in Figure 2.15 for the case of an anisotropic block with varying amounts of overburden. Each pseudosection shows signal period as a function of the azimuth of the co-ordinate system. The color is the value of φ_{yx} - φ_{xy}, the phase difference; white regions are extremely large phase splits and indicate the rotation angle/signal period zones where OOQ phase would be observed. As the overburden is

thickened the effect becomes muted and occurs over an ever-thinning band of rotation angles, as seen in the lower images of Figure 2.15.
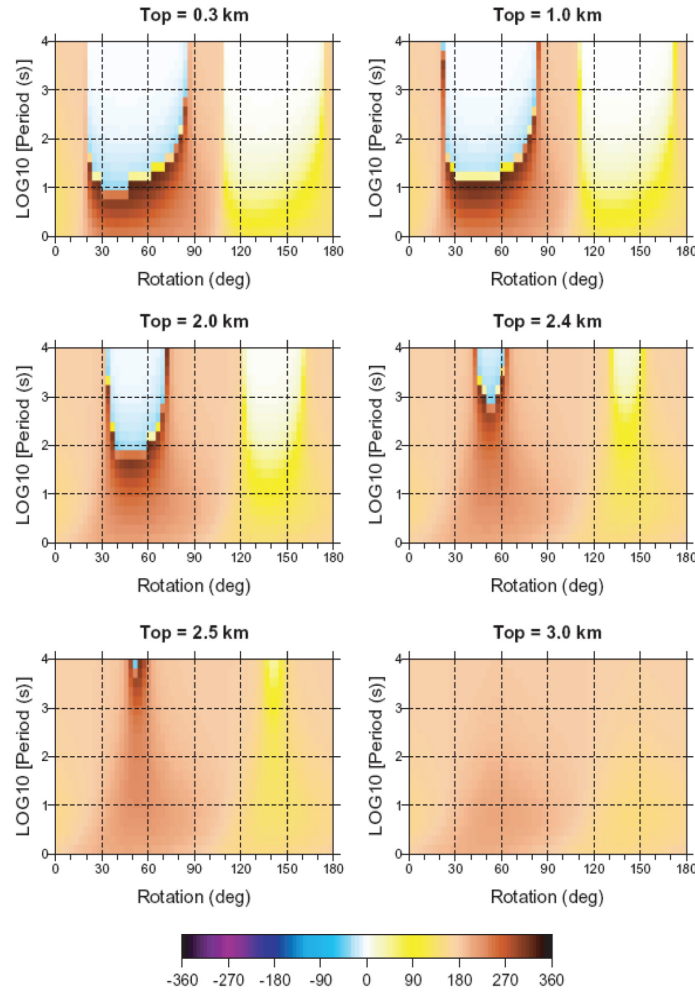
Figure 2.15: For a site directly above an anisotropic block with $\alpha_s = 15°$ away from the 2-D strike. The color represents the phase differences $\varphi_{yx} - \varphi_{xy}$ with varying depth to top of the block from 0.3 to 3 km. Geometry of the block is fixed and anisotropy ratio within the block is 1000/10 with background resistivity 1000 Ωm. Central white anomalous regions indicate rotation angle/signal period regions that exhibit OOQ phase. Image was provided by Dr. Josef Pek. Note that period is longest at the top of these images; it is long period MT data that will exhibit the OOQ phase effects.

The anisotropy ratio of the block is 100/1 within an otherwise resistive and isotropic half-space of 1000 Ωm. No OOQ phase is observed at any rotation angle once the overburden thickness exceeds 3 km. The effect would disappear at shallower depths if the overburden were made of a more conductive material.

2.6   Summary

This chapter has introduced the fundamentals of the magnetotelluric method and has shown how measured MT data contain information that depends on the dimensionality of the subsurface resistivity structure (1-D, 2-D, 3-D, 2-D with anisotropy). The set of forward problems described in this chapter allow us to understand how the apparent resistivity, phase, induction vector and phase tensor can be used to characterize each scenario - and will aid interpretation of field MT data in subsequent chapters.

Chapter 3

Geological Setting

The Fort McMurray (FMC) region is located in Northeast Alberta, and 150 km to the Northeast the WCSB pinches out, exposing the underlying Precambrian basement rocks of the Canadian Shield. This is the only place where Precambrian basement rocks are exposed at the surface in Alberta, elsewhere they are buried beneath the Phanerozoic sedimentary rocks of the WCSB (Ross, 2000). These crystalline basement rocks are part of Laurentia, the North American craton, which includes Precambrian rocks exposed in the Canadian Shield and Greenland, and the surrounding platforms where sedimentary rocks overlie Precambrian basement. Laurentia has remained a stable assemblage of continental crust since its initial assembly in the Proterozoic eon through processes that included continent-continent collisions and terrane accretion (Hoffman, 1988). Direct study of the Precambrian basement rocks beneath the platform is very challenging because of the limited number of basement core samples that have been recovered from this area. In the FMC region all available basement core samples were compiled and described by Walsh (2013), building on studies of the Precambrian basement (Burwash et al., 1962; Burwash & Cumming, 1976; Burwash, 1979; Ross, et al., 1991). Studies of regional scale basement structures require that the core samples are combined with geophysical data. This approach was successfully used during the Lithoprobe Alberta Basement Transect (ABT) which synthesized both seismic and electromagnetic data with the goal of mapping structures in the Alberta basement (Ross, 2000; Boerner et al., 2000). This chapter outlines the tectonic setting of the Precambrian basement rocks in Alberta and specifically beneath the Fort McMurray area in order to guide the geological interpretation of the magnetotelluric (MT) data collected as part of this thesis.

3.1   Major Geological Units and Tectonic Features

The major geological provinces and tectonic features of Laurentia are shown in Figure 3.1. The Archean cratons are ancient blocks of stable continental crust that were assembled during the Proterozoic from 2.0 - 1.7 Ga: the Slave, the Superior, and the Churchill which is divided into the Rae and the Hearne (Hoffman, 1988). The Proterozoic terranes of Western Laurentia are the Buffalo Head, Hottah, Chinchaga, Nahanni, Thorsby and Wabamun (Ross et al., 1991). These crustal blocks were assembled into their present configuration during the time period 1.9 - 2.4 Ga (Chacko et al., 2000; Ross, 2002).

Aeromagnetic studies have allowed the Precambrian structures beneath the sedimentary rocks of the WCSB in Alberta to be mapped and ages have been determined with isotopic dating of drill cores recovered from hydrocarbon exploration (Burwash et al., 1962; Burwash, 1979; Ross et al., 1991; Meyer et al., 1992). The collisions between the Archean provinces occurred along the orogenic belts in that were active during this time (Hoffman, 1988; Hoffman, 1989a; Ross, 2002):

1. The Thelon (TN) orogen forms the boundary between the Rae and Slave Provinces in the North. It is within the TMZ that the MT study of this thesis is located. Its southward extension is the Taltson Magmatic Zone (TMZ), labelled "TA" Figure 3.1. It forms the boundary between the Rae and the Buffalo Head terrane, labelled "BH" in Figure 3.1 (Hoffman, 1989b). This orogenic belt is mainly comprised of 1.98-1.92 Ga granitic rocks but also includes regions of older (ca. 2.0-3.0 Ga) metasedimentary rocks and granitic gneisses (Thériault, 1992; Chacko et al., 2000).

2. The Wopmay orogen is located on the western margin of the of the Slave province and consists primarily of plutonic belts and shelf-related sedimentary rocks, formed between 1.90 and 1.85 Ga (Hoffman, 1988).

3. The Trans-Hudson orogen (THO), which forms the boundary between the Archean Superior and Hearne cratons, contains accretionary prisms, oceanic crust, and significant magmatic material that was assembled between 1.92 and 1.80 Ga (Corrigan et al., 2009).
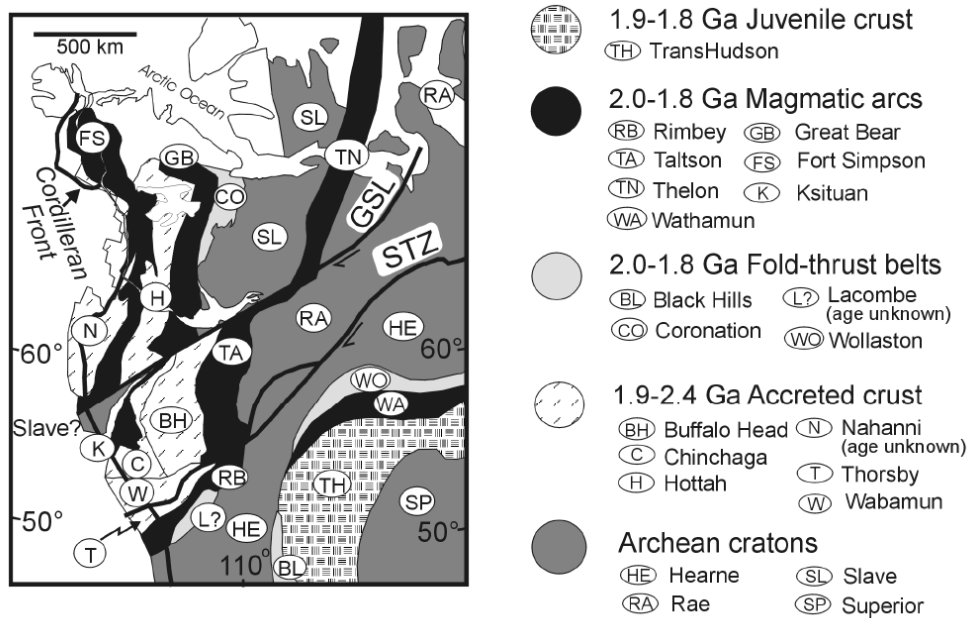
Figure 3.1: Map of the ages and lithological groupings in Western Laurentia. Surface geological data from Hoffman (1988) and structures at depth come from Ross et al., (1991). Modified from McDonough et al., (2000).

Relative motion between the Proterozoic blocks listed above has been controlled by the Great Slave Lake shear zone (GSLsz) and the Snowbird tectonic zone (STZ). The STZ stretches SE-NW 3000 km from Hudson's Bay to the Canadian Cordillera and acts as the

northern border of the Hearne craton. The role of the STZ in the development of Laurentia remains poorly understood (Ross, 2002). The Great Slave Shear Zone (GSLsz) is a dextral fault zone that separates the TN Orogen and Slave craton in the North from the TMZ and Rae craton to the South (Hoffman, 1988). Based on cross-cutting relationships and isotopic age dating the GSLsz is thought to have been active from 1980-1920 Ma (Hanmer et al., 1992). It is possible that the activity along the GSLsz impacted the stress state and resulting fabric of the TMZ rocks. Shear zones have been active in the past in this region and can exert some control over the ancient stress state, sometimes creating rocks that exhibit electrical anisotropy that reflects details of that ancient stress, as discussed in Hanmer et al., (1992); and Eaton (2004).

3.2   Tectonic Assembly of Laurentia

According to Hoffman (1988), modern Laurentia, was created by the assembly of Archean cratons and Proterozoic terranes during the Paleoproterozoic from 2.0-1.7 Ga. This assembly occurred as subduction caused the closing of ocean basins, leading to terrane accretion and continent-continent collisions throughout the Proterozoic. Additional terrane accretion in the Phanerozoic led to the growth of the Western margin of Laurentia in the Canadian Cordillera. This assembly can be summarized, as follows (based on Hoffman, 1989b):

- Between 2.0 and 1.8 Ga, the seven Archean blocks, which exist today as the Slave, Rae, Hearne, Superior, Wyoming, Nain and Burwell, were amalgamated. At the same time a large amount of Proterozoic crust was accreted to the growing craton.

- By 1.8 Ga major assembly of Laurentia had ceased. Tectonic accretion of Proterozoic crust continued up to 1.6 Ga and was supplemented by the initiation of anorogenic magmatism, i.e. magmatic activity not associated with plate boundaries. This is evidenced by many batholiths dated between 1.79 and 1.73 Ga in regions far from contemporaneous orogens (Hoffman, 1988).

- The period 1.6-1.3 Ga was dominated by the anorogenic magmatism that had begun earlier. Thousands of square kilometers of sheet-like magmatic rocks were emplaced and evidence of erosion implies periods of major uplift must have occurred. Orogenic activity was halted during this period. The widespread and temporally extensive anorogenic magmatism in Laurentia led Hoffman, (1989a) to suggest that Laurentia had been above a large mantle upwelling during this time.

- From 1.3 to 1.0 Ga orogeny began again along the Grenville orogen in Eastern Laurentia and a thrust belt in the Northwest at the border of the modern day Beaufort Sea. The Grenville orogen in spatially consistent from modern day Mexico to Sweden and marks the suture of Paleoproterozoic Laurentia to the Neoproterozoic supercontinent Rodinia.

Rodinia experienced final breakup between 750 and 540 Ma (Monger & Price, 2002). The formation of the modern Atlantic Ocean in the Cretaceous marked the end of the Proterozoic structure of Laurentia, only the plate margins have experienced significant deformation since (Hoffman, 1989a).

3.3 The Taltson Magmatic Zone

The FMC region lies within the Taltson Magmatic Zone, which is the southern part of the Thelon-Taltson orogen. It stretches over 2000 km North-South and forms the majority of the Precambrian basement rocks in North East Alberta (Figure 3.2). The TMZ is generally thought to be the result of crustal thickening, resulting from the addition of pre-2.0 Ga crust to the Western edge of the Rae Province by oceanic plate subduction (Ross 2000; McDonough et al.,2000). U-Pb dating has suggested that collision related

magmatic activity in the TMZ had ceased by 1.92 Ga(Ross et al., 1991). There are differing views on the origin of the TMZ, and Chacko et al., (2000) suggested an origin in the plate-interior rather than at a plate margin, noting that granitoid geochemical and isotopic signatures do not resemble those found in modern subduction zones. Their model is reminiscent of the current Indian-Asian collision, which produces magmatic rocks without the influence of a subduction zone.

The TMZ is separated from the Rimbey magmatic arc to the South by the Snowbird Tectonic Zone (STZ) and continues north across the Great Slave shear zone into the Thelon Orogen, which is proposed to have formed by the collision of the Slave and Rae provinces (Hoffman, 1988; 1989). The large lateral extent of the GSLsz in the North and the STZ in the South stands out clearly in Figure 3.1. It is of note that these zones of deformation extend nearly the entire breadth of the continent and occur at an oblique angle to the direction that crust had been accreted to the growing North American continent.
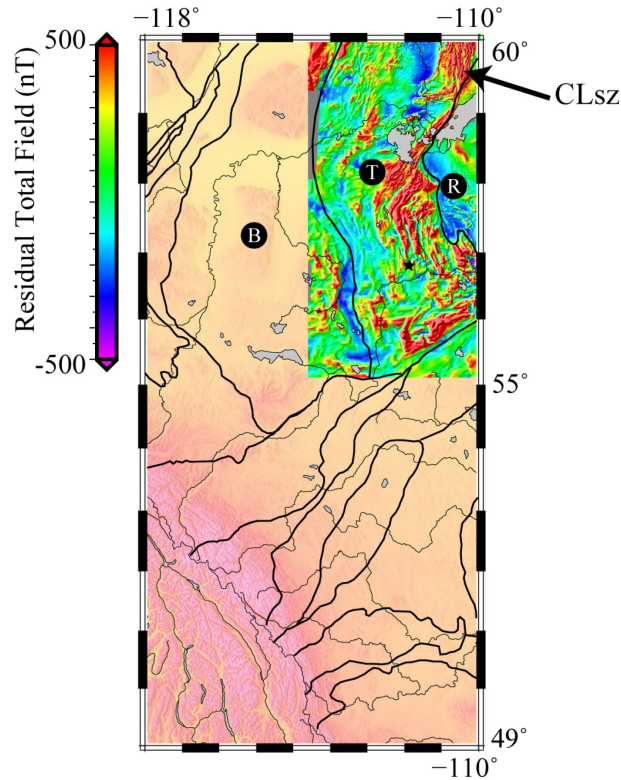
Figure 3.2: Map of Alberta showing Precambrian basement terrane boundaries superimposed on the total magnetic field residual map for Northeastern Alberta. Identified are the Taltson Magmatic Zone (T), the Buffalo Head (B), and Rae (R). The star indicates the location of the FMC study region inside the Taltson. Plotted in GMT with information from Ross et al., (1991) and magnetic field data from Natural Resources Canada.

The Charles Lake Shear Zone (CLsz) is an outcropping system of high-grade mylonites in Northern Alberta and has been identified by McDonough et al., (2000) as the main strike-slip fault zone involved in the oblique collision of the Buffalo Head with the Taltson arc. The flanks of the CLsz have extensive dip-lineated mylonites formed from Taltson gneisses, which indicate strain direction and crustal shortening, while the centre contains strike-lineated mylonites. Beneath the sedimentary cover to the South, the basement rocks cannot be mapped directly but some features may be traced with aeromagnetic data. Aeromagnetic data is usually presented as either the total measured

magnetic field, or as the residual field with the Earth's field removed. The residual field aeromagnetic data for Northeastern Alberta, including the TMZ, is shown in Figure 3.2.

Aeromagnetic anomalies are due to either a paramagnetic or ferromagnetic response from the rocks. A paramagnetic mineral exhibits induced magnetization; it aligns itself parallel to an external magnetic field while it is being applied, magnetization is therefore proportional to the strength of the external field. Rocks are paramagnetic if their constituent minerals contain small net magnetic moments that align in response to an applied magnetic field. Common examples of paramagnetic minerals are olivine, pyroxene and amphibole (Tarling & Hrouda, 1993).

Ferromagnetic materials exhibit strong magnetization that remains after removal of an applied magnetic field. The atoms in a ferromagnetic material align themselves parallel to the external magnetic field permanently. In this way ferromagnets record the direction of the Earth's magnetic field at the time that the rock cooled through the Curie temperature. If a material contains populations of atoms that align oppositely to the applied field in such a way that they cancel and the net magnetic moment is 0, then the material is called antiferromagnetic. Ferromagnets are less common than paramagnets, common examples include nickel, iron, cobalt, and their compounds (Tarling & Hrouda, 1993).

Ferrimagnetism is a weaker type of ferromagnetism where there are opposing magnetizations, as with antiferromagnetism, but one outweighs the other and results in a weak magnetic moment. An important example of a ferromagnetic material is the iron oxide magnetite. It is ferrimagnetic due to the details of its crystal structure.
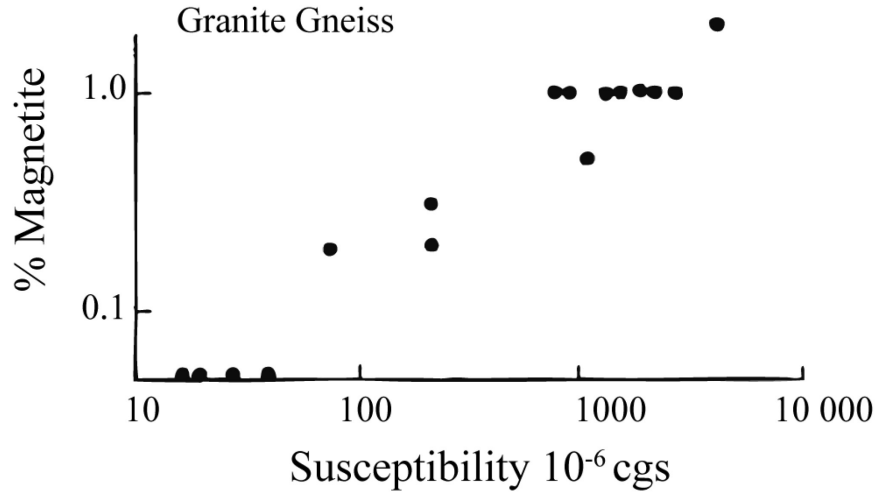
Figure 3.3: Magnetic susceptibility of Northeastern Alberta granite gneiss shield rock samples as a function of the percent of magnetite content. The term cgs denotes centimetre-gram-seconds units. Susceptibility is dimensionless and the linear the relationship is the important feature here, not the value. Modified from Sprenke et al., (1986).

Rocks in the Canadian Shield are generally paramagnetic rather than ferromagnetic, although ferromagnetism can be an important local factor in some formations e.g. some amphibolites and granite gneiss from Northeastern Alberta as described by Sprenke et al., (1986). Figure 3.3 shows the relationship between magnetite content and magnetic susceptibility for granite gneiss samples from the shield rocks in Northeast Alberta. A large positive magnetic susceptibility is related to the degree of magnetization a material exhibits in response to a magnetic field. Magnetite exhibits remnant magnetism, so it can be said that the magnetic susceptibility of rocks in the Alberta basement depends largely upon the content of ferrimagnetic magnetite (Sprenke et al., 1986).

Magnetite may be expected to exist in the magmatic rocks of in the TMZ, whether those rocks are came from the closure of Paleoproterozoic ocean basins or otherwise (Ross, 2002; Chacko et al., 2000; Henderson et al., 1987). Rocks containing magnetite appear as a positive anomaly on aeromagnetic surveys in this region, even when covered with kilometers of Phanerozoic sedimentary rocks. Total field aeromagnetic data for the

exposed shield rocks of Northeastern Alberta is presented in Figure 3.4 from McDonough et al., (2000).

The magnetic properties of rocks can be correlated with their deformation and metamorphosis history. Magnetic highs in Northeast Alberta are often associated with the Taltson Basement Complex (TBC) gneisses and the Chipewyan granite, which are thought to have little shear deformation in their history. The magnetic high associated with the TBC and Chipewyan granites in Figure 3.4 can be traced until it spreads and finally terminates North of the FMC study region (Figure 3.2 right). High levels of stress, strain and heat can change the molecular nature of the rock and therefore change its magnetic signature. Magnetic lows can sometimes be associated with zones of high deformation and metamorphosis (Sprenke et al., 1986). The Charles Lake shear zone is one such magnetic low and is indicated by the white box in Figure 3.4. The magnetite in the CLsz has been oxidized to hematite through the stresses associated with mylonitization (Sprenke et al., 1986; McDonough et al., 2000).
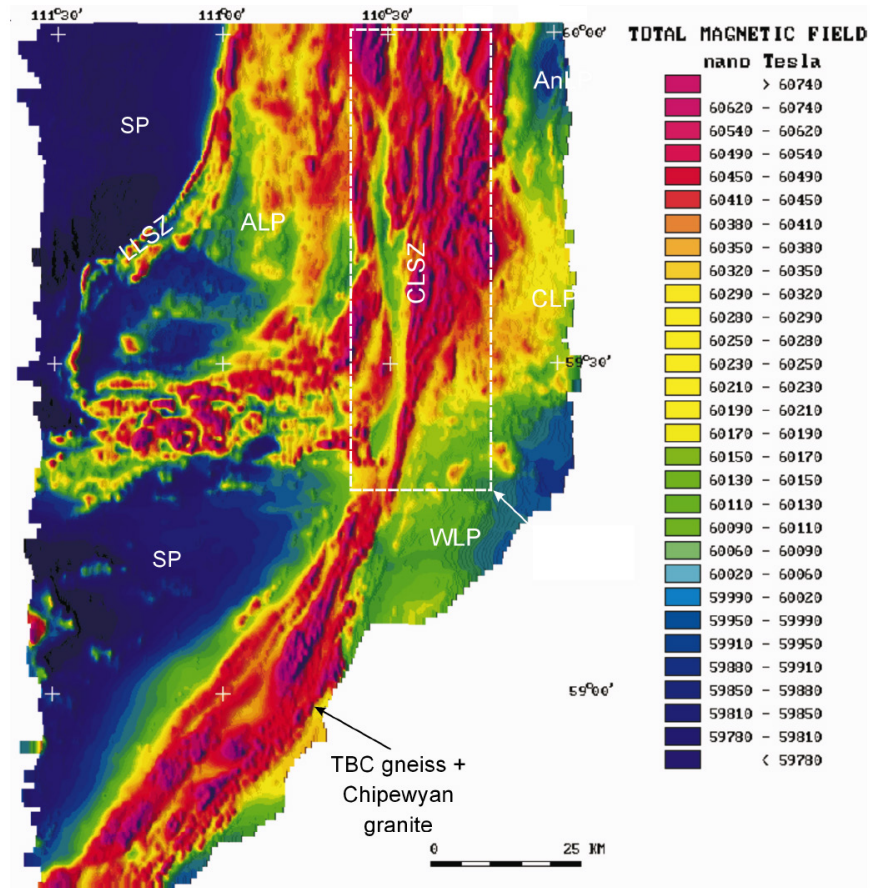
Figure 3.4: Total field aeromagnetic map for the exposed Canadian Shield in Northeastern Alberta. ALP, Arch Lake pluton; AnLP, Andrew Lake pluton; CLSZ, Charles Lake shear zone; CLP, Colin Lake pluton; SP; Slave pluton, WLP, Wylie Lake pluton, TBC; Taltson basement complex. Modified from McDonough et al., (2000).

3.4   Depositional Setting of the WCSB

The exposed rocks of the Canadian Shield in Northeast Alberta dip Southwest beneath the WCSB until they are covered by over 4 km of sedimentary rocks close to the Canadian Cordillera. Figure 3.5 shows a Southwest-Northeast cross-section of Alberta. In the study area around Fort McMurray the Phanerozoic sedimentary rocks are ~250 m thick (Wright et al., 1994).
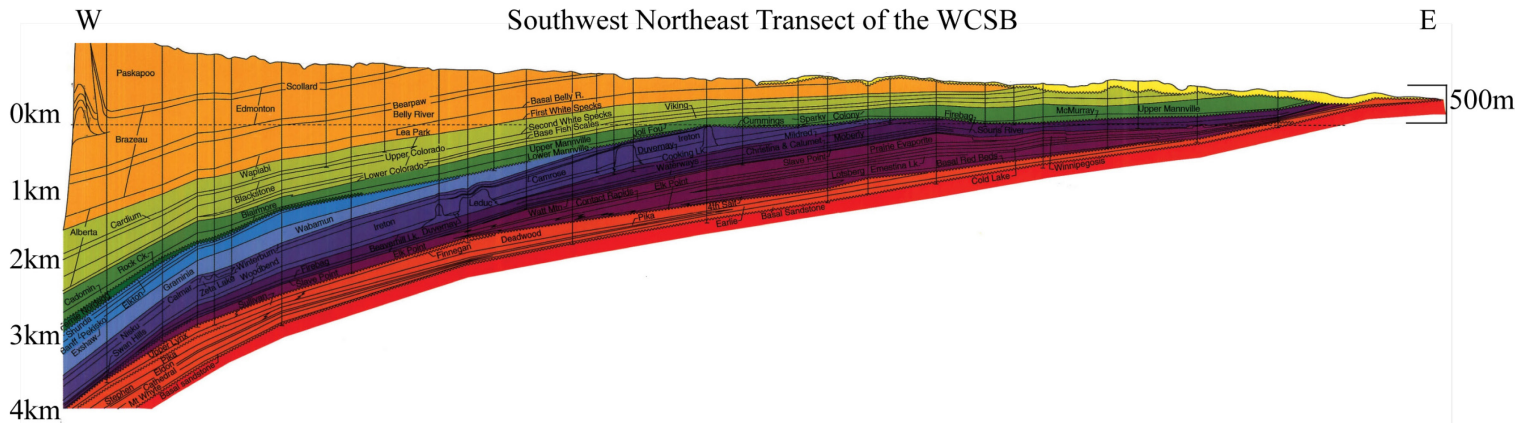
Figure 3.5: Southwest to Northeast transect of the WCSB in Alberta from the Rocky Mountains to the Canadian Shield outcrop. Colours reflect the age of the depositional formation, ranging from Cambrian on the bottom to Cenozoic strata on top. Modified from (Wright et al., 1994).

The earliest sedimentary succession of the WCSB dates from 0.5 Ga and lies above the youngest Precambrian basement at ~1.9 Ga. This is a 1.4 billion years hiatus associated with the unconformity formed after Laurentia was assembled. During this time, Alberta was located on the passive western margin of Laurentia with a shallow marine depositional setting from the Cambrian to the late Jurassic (Price, 1994). Plate subduction changed the passive Western margin of Laurentia into a convergent one at the end of the Jurassic and led to the accretion of a number of Cordilleran terranes (Monger & Price, 2002; Wright et al., 1994). Subduction continued into the Eocene and erosion of the mountains provided abundant sediments that were deposited in the growing foreland basin, formed by downward flexure of the continent by the load of the mountains (Price, 1994).

During the early Cretaceous, high sea levels resulted in the basin wide deposition of formations such as the Mannville group that resulted in the formation of large amounts of hydrocarbon resources. Coal was deposited on the coastal plains, which are present in Western Alberta and the Foothills regions. Fluvial and valley fill structures and

sandstones provided stratigraphic and structural traps for oil as it migrated from pre-Mannville source rocks (Hayes et al., 1994).
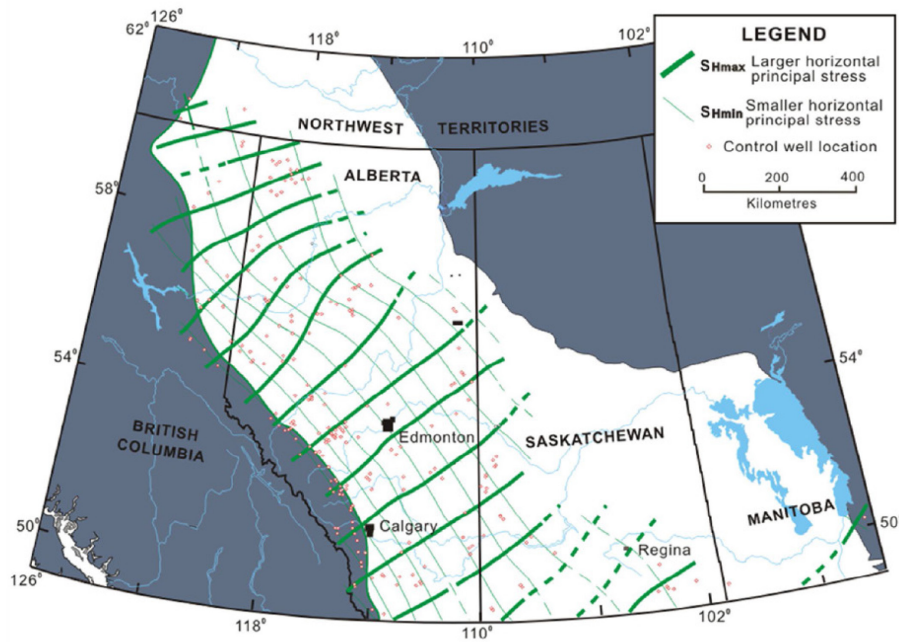
Figure 3.6: From Grasby et al., (2012). Directions of maximum horizontal stress (thick green lines) inferred from well breakouts in Alberta. Maximum stress direction is generally orthogonal to the trace of the Cordillera arc upon the Western edge of the Laurentia.

The Athabasca oil sands are found in the McMurray formation and date from the Cretaceous period. The load of the growing fold and thrust belts upon the craton margin caused the migration of oil from the Southwest to the Northeast where it saturated sand deposits (Conly et al., 2002). The tectonic load from the Rocky Mountains still affects the stress regime of Alberta today by imparting a general Northeast-Southwest direction of maximum stress upon the basement rocks as seen in Figure 3.6 by Grasby et al., (2012). It is not uncommon for Precambrian basement features to exert some control on the Phanerozoic depositional style; the Dunvegan gas field has for its up-dip seal is the Precambrian Dunvegan fault. The Dunvegan fault formed in the same location as a

Precambrian boundary which likely influenced creation and controlled its propagation (Wright et al., 1994). Reactivation of the Precambrian basement since the Phanerozoic is thought to be related to heterogeneities in the sedimentary layers and therefore the localizations of fluids and hydrocarbons (Ross et al., 1999)

3.5   Summary

The goal of Theme 4 of the Helmholtz Alberta Initiative (HAI) is to investigate the potential of geothermal energy as a heat source for use in the oil sands industry. In this context, it is important to characterize the subsurface structure of the region. The tectonic and geological history of both the Precambrian basement and Phanerozoic sedimentary rocks in Alberta has been summarized in this section to provide context for the research in this thesis. The study region near Fort McMurray is located within the TMZ, which has a complex history of deformation and magmatic activity. Aeromagnetic studies of the TMZ have shown that the study region is located in an aeromagnetic low, located south of the high magnetic anomalies associated with magnetite content which can be traced from the TBC and Chipewyan granite outcrops near Lake Athabasca.

Studies by Walsh (2013) and Chan (2013) have attempted to characterize the crust in the FMC region by direct analysis of core samples, well logs and seismic profiles This thesis extends the previous work in this region by examining the crustal structure of the region using magnetotelluric imaging.

Chapter 4

Geothermal Background

4.1 Introduction

Heat is constantly escaping from the Earth with an average heat flow of 50 mW m^{-2} that originates from both the primordial heat left over from the formation of the Earth and radioactive decay of elements in the crust and mantle (Fowler, 1990). While this energy flux is less than 1/100 000th of the average insolation (Stegena, 1976) geothermal energy is a viable source of power because of the vast quantities of heat stored in rocks within drilling depth of the surface. Geothermal exploration is focussed on the upper 10 km of the crust, which is the region that may be reasonably accessed from surface. There are many places with a high enough temperature gradient to contain significant amounts of thermal energy. This is stored both in the host rock and in any fluids that might be present in fractures or pores. Localized regions with high temperatures can be used to generate electricity while reservoirs with lower temperatures (< 160°C) are better suited as a source of heat that can be directly used for heating greenhouses, swimming pools and in industrial processes. To date, over 88 000 GWh of direct use heat energy has been utilized worldwide while geothermal electricity has created over 63 000 GWh (Lund et al., 2011).

Geothermal reservoirs are found in a range of geological settings and are defined as regions of the Earth that collect and store heat, becoming significantly hotter than their environment. These reservoirs are organized broadly by the mode of heat transport into the reservoir, either by conduction or convection from depth. If the host rock has enough natural porosity and permeability then heat can effectively be transported to the surface, such systems are called hydrothermal systems and are the most economically viable

(Moeck, 2013). Hydrothermal reservoirs are most often found at tectonic regions such as active spreading ridges or subduction zones, or above of recent intrusions that can provide heat, fluid, and natural fractures in sufficient quantity. Typical heat sources and surface expressions are seen in Figure 4.1.
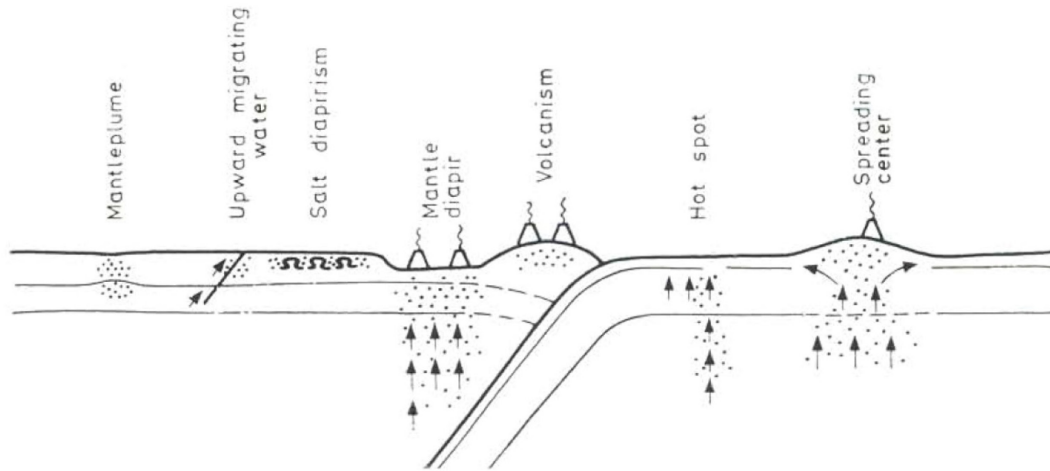
Figure 4.1: From (Stegena, 1976). Schematic of upward-moving hot material producing hydrothermal reservoirs

Utilization of heat from hydrothermal reservoirs is generally limited to regions of active tectonics, volcanism and localized magma intrusions. Indeed, spreading plates alone contribute to 40% of the Earth's heat loss (Stegena, 1976) This requires the presence of heat, as well as the fractures and fluids to allow fluid circulation to remove the heat. Currently implemented hydrothermal systems include subduction zones in Mexico, Indonesia and the Philippines, spreading ridges as in Iceland, magma intrusions in continental crust as in Lardarello, and extensional regions such as the Upper Rhine Graben in Germany. Magma chambers such as Yellowstone National Park in North America is not a development target but serves as a good example of a hot spot geothermal reservoir for study.

Away from hydrothermal regions such as these, high temperatures may still be present, but the fluids and porosity needed to extract the hear are lacking. Thus these conduction dominated systems are much more difficult to utilize and are referred to as "Hot Dry Rock"(Berktold, 1983). Their geothermal potential should not be ignored, as there is an enormous amount of heat stored in the crust. For the example of the U.S.A., Tester et al., (2007) showed that the total amount of thermal energy found at depths between 3 and 10 km is of the order of 100 000 times the country's annual energy consumption. Extraction of the heat stored in conductive contexts requires the creation of artificial porosity (fractures) and the injection of a fluid to transport the heat to the surface, in what is called an Engineered Geothermal System (EGS), illustrated in Figure **4.2**.
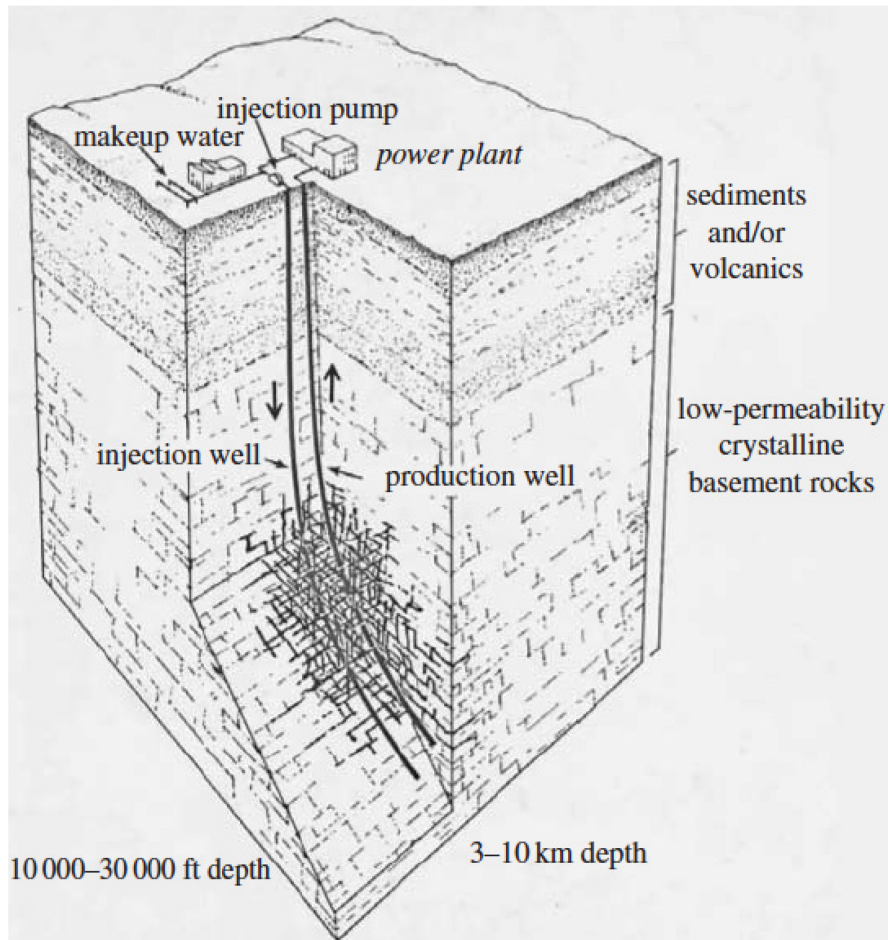
Figure 4.2: From Tester et al., (2007). Schematic of Engineered Geothermal System, designed for use in a region of hot rock with low natural permeability. Water is pumped down a well through induced fractures and produced through a second well.

In an EGS one or more wells are drilled into the thermal resource and fractures are created with high pressure fluid injection into the formation (Hofmann et al., 2014). Pumping fluids through the reservoir can be used to extract heat. The process can be thought of as "heat mining" as thermal energy is removed far quicker than it can be replenished via diffusion due to natural heat flow. Drilling to the required depths is both expensive and difficult, details of the lithology and geology must be taken into account to minimize the costs and associated risks. Knowledge of the stress regime and any

anisotropy is necessary when planning and attempting to predict the propagation of the induced fractures.

Discovery and development of both conventional (hydrothermal) systems, and EGS requires geological and geophysical exploration. In the first case the target will be hot fluids permeating a host rock and circulating in a closed system, in the latter it will be focussed on regions with elevated temperatures and regions / formations where fractures may be effectively formed. Geophysical and geological exploration must be integrated with other scientific data, and ultimately economic predictions and cost analyses to evaluate the feasibility of the geothermal resource. A key geophysical parameter to measure is electrical resistivity because it is sensitive to fluid quantity and rock permeability, it can be related to temperature as well (Spichak & Manzella, 2009). Electrical resistivity can be determined with various EM techniques. For exploration beyond 500 - 1000 m depth, the preferred EM method is magnetotellurics, which uses natural electromagnetic signals to measure the resistivity at depths larger than those available to any other EM method. MT makes use of signals from 1000 - 0.001 Hz, high frequency waves dissipate more quickly in the Earth while low frequency signals may sample much deeper regions. MT is, therefore, quite versatile can be appropriate for exploration on depths scales from 1 km to 200 km. Resolution drops with increasing signal period but when applied to the upper 10 km of the crust, as is suitable for geothermal exploration, MT retains reasonable resolution and can map subsurface resistivities effectively.

The focus of this thesis is to understand how MT geothermal exploration can be applied to locations suitable for EGS. MT measures electrical resistivity, the next section will demonstrate the different sources of electrical resistivity often encountered in geothermal zones.

4.2   Resistivity of Rocks Encountered in Geothermal Zones

To understand how electromagnetic methods can be used in geothermal exploration, the resistivities of rocks typically found in these systems must be considered. Rocks are rarely pure materials and are usually composed of several components each with different resistivities. The overall resistivity can be calculated from knowledge of the composition and geometric distribution of the components. Two phases control the resistivity, the individual rock grains with generally very high resistivity, and the pore space occupied by generally low resistivity material. A conducting second phase may be composed of saline fluid, melt, sulphides or graphite films and carry a several order magnitude influence upon the total resistivity of the rock (Unsworth & Rondenay, 2012).

The composition and degree of interconnection of any pore fluid, and the temperature both of the rock matrix and pore fluid, will also be of importance (Berktold, 1983). A typical hydrothermal reservoir is shown in Figure 4.3 and shows the unique resistivity features expected to be present in the reservoir. Each component contributes to the bulk measurement of resistivity to various degrees, it is important to understand the reasons why each of part of the typical geothermal resource has the resistivity signature that it exhibits. The contributing factors from the various materials will be considered individually and then combined.
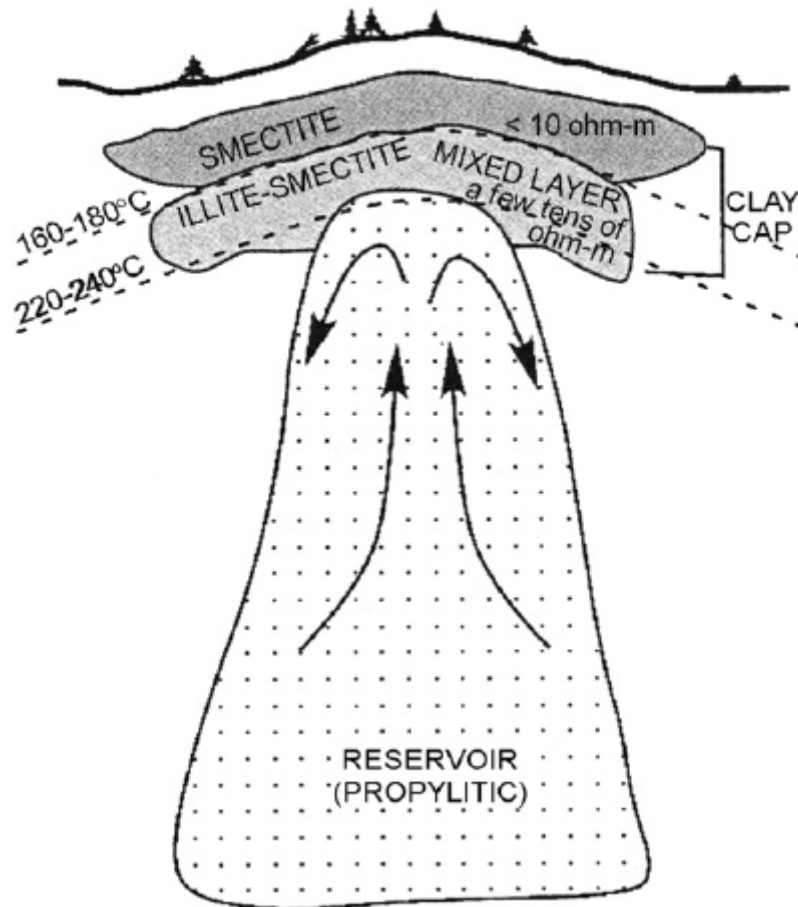
Figure 4.3: From Pellerin et al., (1996). Model of a convection dominated hydrothermal reservoir, hot fluid in porous host rock beneath highly conductive cap rock of clay and alteration minerals, which will be the picked out in the survey. Two zones of alteration mineral (Smectite, Illite) are shown and related to the temperatures required to produce them.

4.2.1 Resistivity of Mineral Grains

All rocks are made from an assembly of one or more different minerals. The resistivity will depend upon the electrical properties of each particular mineral, their abundance and geometric distribution. A low resistivity means that there are charge carriers, typically ions or electrons, that are free to move under the influence of an electric field. Rock grains will generally have a very high electrical resistivity since most have strong chemical lattices that do not allow electron motion or contain natural pathways by which

current can travel. There is, however, an exponential decrease of resistivity with temperature, as thermal activation increases the mobility of the charge carriers. The relationship between temperature and resistivity for synthetic basalt was examined by Presnall et al., (1972), who reported two temperature regimes, both linear with respect to log conductivity. For solid basalt there were two curves, shifted by approximately one order of magnitude upwards if the basalt was glassy rather than crystalline. Crystalline basalt ranged in resistivity from 10^4-10^2 Ωm near the melting point near 1100°C. The two types of solid basalt experienced the same rate of conductivity increase with temperature, but without a firm crystalline structure the glass basalt was able to more effectively conduct electricity and reached a maximum around 10 Ωm. Above the solidus, the two conductivity curves increase by approximately an order of magnitude and have a much steeper slope reflecting that disassociated ions in the melt are a much more effective current transfer mechanism. Typical solid-state igneous and metamorphic rocks in the Canadian shield will have resistivities greater than 1000 Ωm (Palacky, 1987).

4.2.2   Melt and Partial Melt

Partially molten rocks facilitate current transport and higher melt fractions will correspond to higher conductivities. The melt will contain dissolved ions that carry electric charge, and are free to move through the liquid phase. The viscosity of the molten rock controls the mobility of the charge carriers in the melt. For low melt fractions the dihedral angle describing the geometry of melt accumulation on grain boundaries is very important. If the dihedral angle is small ($< 60°$) then melt will form interconnected pathways and conductivity will rise dramatically (Watson & Brenan, 1987; Partzsch et al., 2000). As with brines, the abundance of charge carriers and viscosity are important and typical resistivities lie below 1 Ωm. It can take a significant amount of melt

fraction, at least as much as 10%, for the bulk resistivity to drop to a value below 100 Ωm (Wannamaker, 1986). Melt dominated systems are too active in themselves to be appropriate for geothermal development, they are generally more useful acting as the deep heat source for a shallower reservoir. Iceland and New Zealand are unique exceptions because they resides on tectonic boundaries and thus have enormous geothermal gradient and capacity for thermal energy.

4.2.3 Brines and Pore Fluids

The resistivity of fluids depends upon the concentration of charge carriers (i.e. the salinity), the type of charge carriers, and the physical parameters of the solvent such as viscosity that allows the movement of ions. An increase in salinity naturally accompanies an increase in conductivity because of the abundance of charge carrying ions; the dependence is generally exponential except for very low salinities where relationship is positive linear (Unsworth & Rondenay, 2012). The temperature also affects the pore fluid conductivity and is especially important when considering fluids in a geothermal context. There exists an exponential dependence of saline fluid resistivity upon temperature, as demonstrated by Quist et al., (1970) in Figure 4.4, and by Ussher & Harvey (2000) in Figure 4.5. There are several factors that combine to give the resistivity value of the fluid. At a given fluid pressure, resistivity first drops as temperature is increased due to the decrease in viscosity of the fluid and charge carriers can move more easily. Above some critical temperature, in this case near to ~300°C, a minimum is reached after which the resistivity increases once more. The increased temperature makes the density of charge carriers fall, so fluid less capable to carry charge and therefore the resistivity rises. The balance between charge carrier mobility and density defines two regimes, one where each is the dominant factor.
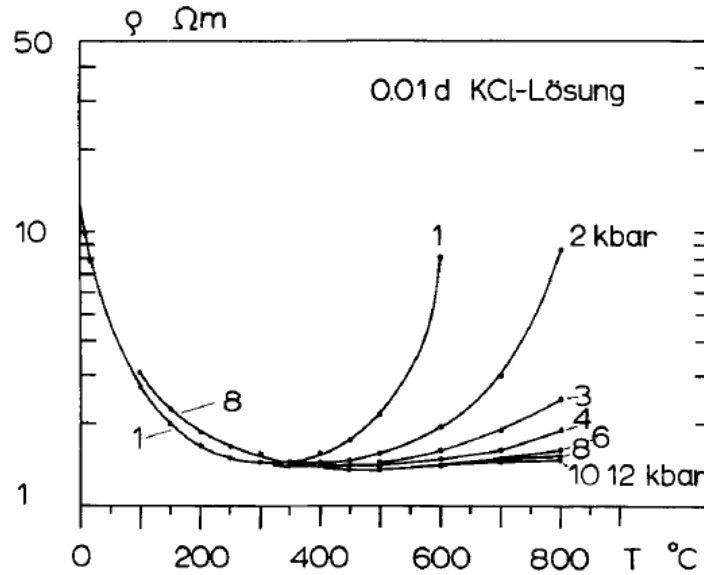
Figure 4.4: From Quist et al., (1970) redrawn by Berktold, (1983). Electrical conductivity plotted against temperature for a KCl solution at varying pressures.

At all but the highest pressures, it was found that the same pattern of high-low-high resistivity is observed (Ussher & Harvey, 2000). When pressure is increased to levels perhaps found in the deep crust, a balance is found, as the charge carriers are physically forced closer together. High pressure therefore mitigates the high temperature increase in resistivity by not allowing the ions to separate through in the low-density regime; the resistivity value reaches a minimum and stabilizes. Vapour dominated, rather than fluid dominated, reservoirs may have a much higher resistivity because the low density gas cannot support a current, but the region surrounding the steam zone may contain detectable and conductive condensate (Berktold, 1983).

If salinity of the fluid is allowed to vary, as in the NaCl brine considered in Figure 4.5, the curve is simply shifted upwards or downwards. The salinity, increasing logarithmically, shifts the shape of the resistivity vs. temperature curve from Figure 4.4. A fluid at a particular salinity when heated will experience first a drop in resistivity,

followed by a rebound after ~300°C. Because of the geological uniqueness in the variety of geothermal zones typical pore fluid parameters cannot be known exactly. Knowledge of pressure, salinity, and expected temperature in the target area must be known in order to constrain predictions upon fluid resistivity. Typical geothermal fluids will have a salinity between 1000 and 100 000 ppm, and a resistivity between 1 and 10 Ωm, somewhat above the 0.2 Ωm of seawater (Berktold, 1983; Ussher & Harvey, 2000).
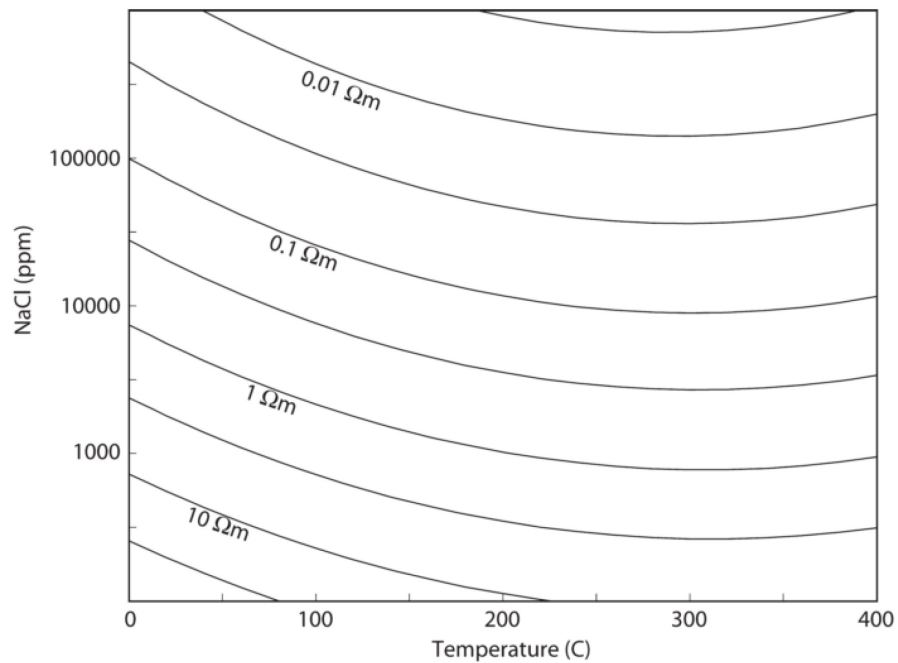
Figure 4.5: From Ussher & Harvey (2000), redrawn by Unsworth & Rondenay (2012). This is a contour plot of electrical resistivity as a function of both fluid temperature and salinity, at constant pressure.

4.2.4 Clay Minerals and the Electrical Double Layer

Hydrothermal metamorphism of the host rock can produces a variety of clay minerals. The presence of clay can significantly increase the conductivity and it is therefore important to understand the mechanism. Spichak & Manzella (2009) give a review of which clay minerals are produced at specific temperatures, and the associated

resistivities. Clay minerals are conductive because of the so-called electrical double layer (EDL) of cations that forms at the water/clay interface and provides another path for electric current conduction. Temperature is the major factor controlling clay mineralogy. At temperatures below 200ºC the highly conductive clay smectite is the predominant alteration mineral that is produced, and it is therefore the most likely to be found outside the reservoir itself and away from the highest temperatures. Typical smectite resistivities are on the order of ~10 Ωm, with chlorite and illite resistivities several times larger (Flóvenz, 2005; Pellerin et al., 1996). Inside the reservoir, the hot fluid of a hydrothermal system the alteration minerals are generally the less conductive illite or chlorite which are created at higher temperatures, above ~220ºC conductive smectite is not created at all (Ussher & Harvey, 2000). The ions in solution are able to travel along the interconnected clay film with less resistance than the viscosity of the solvent provides. Unless the salinity of the pore fluid is very high then Flóvenz (2005) showed that the clay EDL to be the dominant mechanism contributing to the bulk conductivity measurement, for both smectite and the more resistive chlorite zones.

Conductance (the product of conductivity and thickness) is by definition non-unique, this means that without *a priori* information, it is impossible to determine the true Earth structure. Laboratory measurements on the resistivity of typical geothermal-zone rocks are important because it equips the interpreter with some degree of expectation of the resistivity structure. The next section will examine the manner in which the previously discussed factors interact in typical geothermal zones.

4.3   Bulk Resistivity in Geothermal Zones

4.3.1   Fluid Saturated Rocks

The results described above must be combined to predict the resistivity of fluid saturated rocks. The study of the importance of rock porosity (and therefore presence of pore fluid) upon electrical resistivity of rocks was first established by Archie (1942). Archie's Law states that the bulk resistivity of a fully fluid saturated rock can be related to the resistivity of the pore fluid and the details of the porosity.

$$\rho = C\rho_w \Phi^{-m}$$

(4.1)

At constant temperature, the resistivity ρ of the rock is defined by the resistivity of the fluid ρ_w, the porosity Φ, and the two constants m, the cementation factor relates to permeability, and C is an empirically determined constant. An assumption of Archie's Law is that the host rock resistivity is so high that it can be ignored; only the conductive phase of the total rock is considered. At high temperatures and for certain rock matrices, however, it may not be appropriate to dismiss the conductivity of the rock grains outright. Equation (4.1) also assumes that the only efficient conduction pathway is via the pore fluid, this means that Archie's law is not appropriate for rocks containing conductive clay minerals, as explored above. Studies on porous rocks from geothermal fields in New Zealand and the Philippines by Caldwell (1986) suggest that a power law dependence of this form is appropriate, however, simple extrapolation of the equation may not be appropriate as empirical constants were shown to be quite different from the sedimentary rock formulation. The effect of clay minerals and temperature variations cannot be ignored when studying geothermal systems.

Modifications made by Glover et al., (2000) allowed the resistive phase to be included in Archie's Law. The result is a removal of the condition that the rock matrix must be infinitely resistive, partial melt and clay conductive pathways may be considered. If the porosity of a rock is quite low then Archie's law will necessarily predict very high resistivity values and will eventually overestimate true resistivity (since at the extreme it trends to infinity). Another way to approach resistivity evaluation of composite media is to relate it to the parallel and series circuit models. The brick-layer model for a two phase system is based on the observation that the bulk resistivity is significantly different if the current is forced through the resistive phase or allowed to follow a parallel path through the conductive phase. Any given rock may lie somewhere in between and therefore, with differing weights, the effective resistivity will be a linear sum of the parallel and series representations. This approach is only valid for melt fractions below 10% (Partzsch et al., 2000). For the case of larger melt fractions corresponding to a full interconnected melt network, the Modified Brick Layer Model (MBLM) was presented by Schilling et al., (1997) to include melt fractions up to and including 100%.

Although the country rock varies, the resistivity in geothermal zones is controlled primarily by the cation exchange capacity of any present clays, and second by the saline fluid following an Archie's Law relationship (Caldwell, 1986) which may be common in many geothermal systems. It is therefore possible to determine some expected values for resistivity from typical salinity and porosity values found in known reservoirs. Ussher & Harvey (2000) noted that any water occupying pore spaces in a reservoir will likely have at least some natural salinity and may gain in this respect from liberated ions from the host rock. The exact species of dissolved anion and cation might differ, but Na and Cl are good proxies for resistivity estimates. Salinities reported by Ussher & Harvey (2000) range from ~2000 ppm in the Wairakei geothermal field in New Zealand to near

~200 000 ppm in Salton Sea in California and display a constant temperature resistivity change of nearly two magnitudes. Schill et al., (2010) used 100 g/L, or ~100 000 ppm, when modelling brine in the Rhine graben geothermal zone. At the most resistive the pore fluids are expected to be on the order of 10 Ωm, however, which is still a conductive target compared with Precambrian basement rocks which are often have resistivities of several thousand Ωm. Geothermal reservoirs can be identified at a wide range of porosities. Hydrothermal systems can be supported in regions of high porosity but even low porosity if there is significant permeability, perhaps due to extensive fractures and EGS by definition exist where there is little to no natural porosity or permeability Berktold (1983). Caldwell (1986) performed resistivity analyses on rocks representative of Philippean and New Zealand geothermal sites that with porosities ranging from 3.1% in altered andesite to 58% in altered ignimbrite.

4.3.2   Hydrothermal Reservoirs

There is a consistently observed sharp resistivity transition in high-temperature reservoirs, this was studied for basaltic thermal zones in Iceland by Flóvenz (2005). Unaltered rock samples were shown to have resistivities values completely dependent upon the pore fluid parameters while samples containing any type of alteration clay mineral rendered the pore fluid conduction pathway by comparison unimportant. This means that in high temperature reservoirs the conductivity is driven not by the pore fluid or salinity at all, but rather by the efficiency of the EDL conduction. The previous studies, among many others, have allowed the development of conceptual resistivity models of geothermal and hydrothermal areas. An ideal hydrothermal system, example shown in Figure 4.3, has first a source of heat, a host rock with requisite fluid filled fractures/pores, and a cap rock to isolate the system that will likely be made of conductive alteration

products. The zone at the top of the hydrothermal system will have very low resistivity smectite clays due to the typical 70°C - 200°C temperatures (Ussher & Harvey, 2000). The hottest parts of the geothermal reservoir may have the highest resistivity values. High-temperature alteration minerals like illite and chlorite are not as conductive as the low-temperature smectite, and deeper regions may naturally have less porosity.

By relating resistivity measurements to the known pattern of alteration clays it can be possible to make temperature estimates with accuracy. A borehole log of resistivity in this sort of area can be used to confidently predict temperature via resistivity in areas near the well or that are geologically similar. The clay above the hydrothermal fluids can form an effective seal and prevent dissipation of the reservoir. It is a drawback to EM methods like MT that they have difficulty imaging structure beneath highly conductive targets. Resolution is reduced because the signals used in MT decay very quickly in conductive media. Another important caveat is that the hydrothermal alteration materials will remain high conductivity targets even once the high-temperature fluids have been exhausted.

4.3.3 Hot Dry Rock and EGS

Shankland & Ander (1983) looked at the correlation between high heat flow regions and the presence of high-conductivity layers in the crust detected with MT and found a positive result. These studies led the authors to conclude that electrical conductivity and temperature of the minerals can indeed be related and therefore anomalously conductive regions of the upper mantle may be interpreted as regions of anomalously high temperature, perhaps the sources of geothermal reservoirs not associated with plate mechanisms. If there has been an upwelling of magma it will appear relatively conductive if the temperature is high enough for some of the intrusion to remain molten, this is the case in the Puhimau thermal region in Hawaii as studied by Bartel & Jacobson (1987).

The authors found that the thermal region could be linked to a conductive region around 5 Ωm, which was interpreted as a solidifying intrusion that had acted as the source of heat. Spichak et al., (2011) sought to make this large-scale correlation effective on a local scale, trying to measure temperatures at depth by way of shallow borehole temperature measurements. An indirect geothermometer of this sort requires that the main parameter controlling rock resistivity is only temperature, which is a large assumption to make. There may be some one-to-one correlation between temperature and resistivity of the mineral grains that make up rocks but any such conclusions must be made very carefully due to the many other factors that may affect measured resistivity can be much more influential.

There is also the possibility of conductive minerals such as graphite, interconnected films of which are commonly interpreted as a source of conductivity in the deep, dry and brittle lower crust of Alberta (e.g. Eaton, 2004; Türkoğlu et al., 2009; Boerner, 1999; Mareschal et al., 1995). The chemical structure of the carbon atoms in graphite is such that a weak π-bond, allowing movement of the electron and thus electrical conduction, bonds one of the four valence electrons to its neighbours. The source of crustal graphite deposits is generally thought to be CO_2-rich fluids which can precipitate graphite onto the rock surface (Katsube & Mareschal, 1993). Graphite can prove to be very conductive, a laboratory value of 10^{-5} Ωm was found by Duba & Shankland (1982), meaning that high conductivities need not necessarily be due to saline pore fluids, partial melts, or high temperatures.

4.4 Electromagnetic Exploration in Geothermal Zones

It has been shown in the previous sections that geothermal resources are often associated with a variety of electrical resistivity signatures. EM geophysical exploration methods are

therefore useful exploration tools for geothermal systems. Over last 50 years there have been many case studies of EM geothermal exploration being used successfully. This section will discuss examples of EM geothermal exploration with a focus upon MT, which is of great use especially when the reservoirs are at depths of several kilometers.

Upper mantle conductivity anomalies found with electromagnetic exploration have been correlated with expected high upper mantle temperatures. An early example are the conductive lineaments that were found beneath, and just east of, the African Rift zone in Kenya with magnetic transfer functions by Banks & Ottey (1974). Inversions of the data defined two 10 Ωm regions that were interpreted to be regions of high melt concentration in the upper mantle. Their interpretation was corroborated by seismological evidence and the surmised location of the anomalies agreed with locations of recent volcanism.

Geothermal fields both in and outside of volcanic zones in Iceland have been identified using primarily shallow methods such as transient electromagnetism (TEM) and direct current (DC) resistivity (Eysteinsson et al., 1994). For example, Figure 4.6 shows resistivity cross sections calculated with DC resistivity and TEM data in the Nesjavillir geothermal field in Iceland studied by Arnason & Flovenz (1992). Both EM methods give the same general shape, and correlate very well with the isotherms measured in nearby boreholes. The cross pattern represents a zone of high resistivity underlying low resistivity in a region of high temperature interpreted as the location when the cause of conductivity changes in the geothermal reservoir.
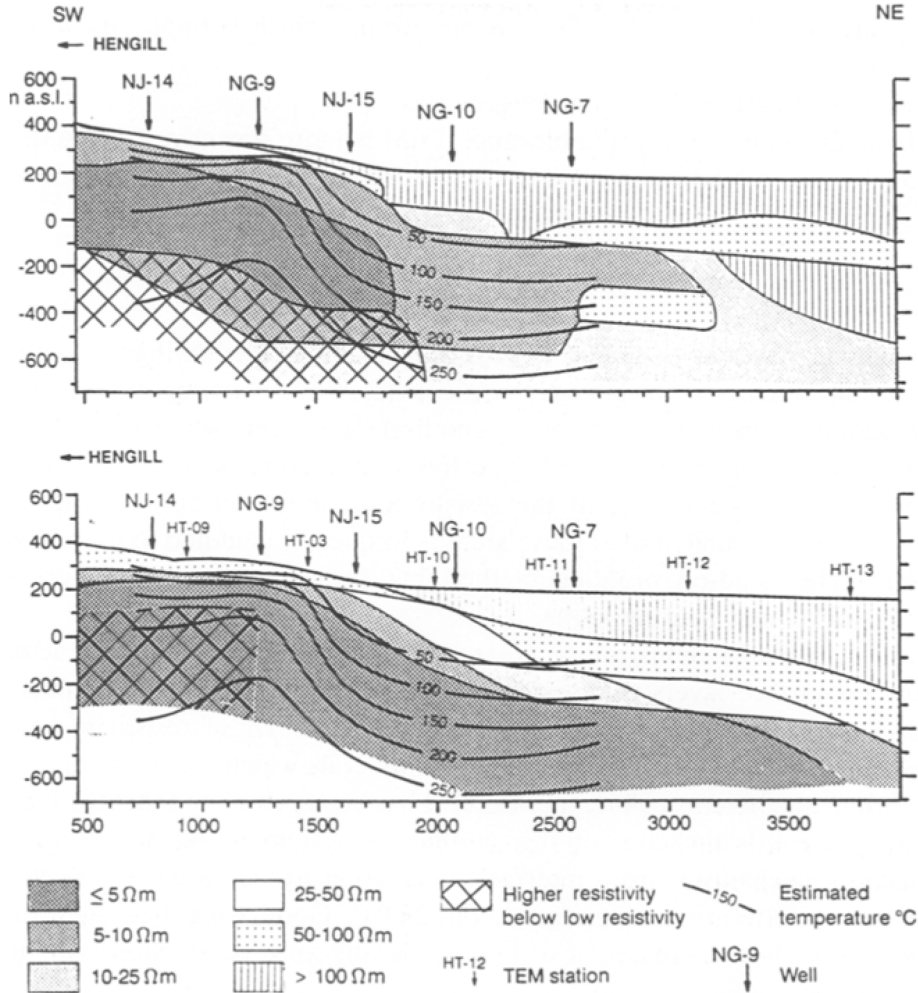
Figure 4.6: From Arnason & Flovenz (1992). 2-D direct current model (Above) compared with a 1-D TEM inversion (Below) in the Nesjavillir geothermal field in Iceland. Colour fills represent resistivity contours and cross pattern indicates inferred location of geothermal reservoir.

Flovenz & Karlsdottir (2000) used TEM in Northern Iceland to improve upon low-resolution DC resistivity studies. The EM method showed that sequences of basalt, and their temperatures, encountered by boreholes had unique resistivity values that could be mapped. Their 1-D TEM inversion resulted in a resistivity cross section that was able to resolve the single fluid pathway that acted as the source of all the Eyjafjordur geothermal fields. The authors interpreted one high-pressure upwelling of hot material in a fractures basement causing fluids to flow laterally and source several surface manifestations.

The Taupo volcanic zone (TVZ) in New Zealand has been successfully studied with electromagnetic methods. The geoelectric structure is characterized by a surface layer several kilometers thick of low density pyroclastic material that lie above low resistivity shallow basement rocks that are thought to be filled with high temperature geothermal fluids resulting in rocks of ~10 Ωm, down from the ~300 Ωm of the surface rocks (Bibby et al., 1995). The TVZ is therefore an ideal target for EM methods since geothermal targets are the conductors that should be detected directly. The TVZ structure had been defined by gravity surveys (Reilly, 1972) which noticed a general -350 mGal anomaly in the TVZ down to 2.5 km depth, and by seismic refraction studies e.g. Robinson et al., (1981) who detected a low velocity zone at least 1.5 km/s slower than the underlying basement coinciding with the extent of the TVZ to a depth of ~2 km. The seismic data were corroborated with resistivity studies, and Schlumberger DC resistivity arrays have been able to define near surface structures associated with more than 20 geothermal systems in and around the TVZ (Bibby & Risk, 2005). Bibby et al., (1995) used DC resistivity to map near surface hydrothermal structures and speculated that a vertical convection cell sourced each field, with cold water returning to depth in between. 2-D MT exploration by Ingham (1991) examined the TVZ down to 6 km depth and contributed to defining the lateral extent of the of the geothermal source structure, but the bottom of the conductive region could not be imaged. Advancements were made by Bertrand et al., (2012) who used a grid of broadband MT sites to develop two and three dimensional resistivity models that investigated the connection between the near surface hydrothermal systems and their magmatic sources up to depths of 10 km. The authors were for the first time able to image the magmatic sources of the hydrothermal systems and the individual fluid pathways that drive the thermal expressions of the TVZ. The New Zealand case is not isolated. MT soundings have revealed conductivity anomalies

beneath geothermal systems in many places worldwide due to its impressive depth penetration as well as lateral resistivity resolution. Correlations between electrical conductivity revealed by MT and geothermal zones such as that in Figure 4.7 from Sandberg & Hohmann (1982) have provided proofs of concept.
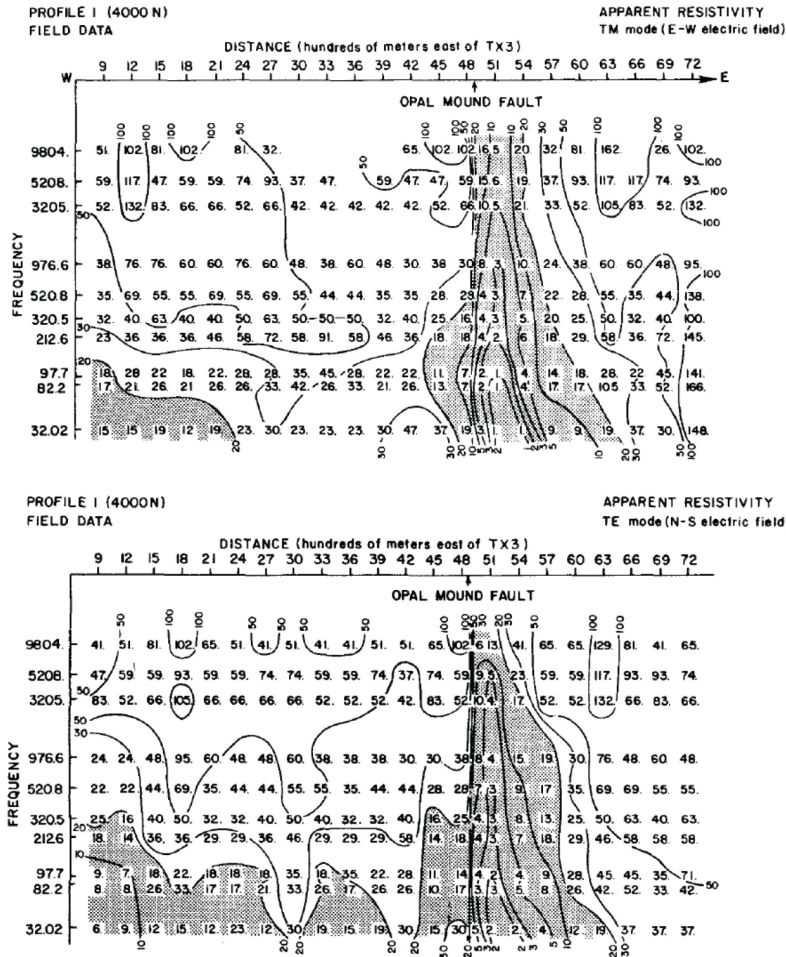
Figure 4.7: From Sandberg & Hohmann (1982). This is a MT survey with Transverse Magnetic (top) and Transverse Electric (bottom) mode frequency pseudosections of audio-magnetotelluric data from the Roosevelt Hot Springs geothermal region in Utah, USA. Shaded regions are below 20Ωm apparent resistivity. Location of the Opal Mound Fault feeding the geothermal reservoir is provided.

Jiracek et al., (1996) studied the Jemez volcanic zone in New Mexico with MT in an attempt to trace crustal isotherms. Their study region is particularly suitable for MT

temperature mapping because of the sharp change in temperatures observed in the region with good control by more than 60 geothermal wells drilled to depths up to 4.5 km. A clear correlation was found between the isotherms projected from well logs and the depth to a conductive region in the upper crust. The Puga geothermal field in India was studied with a series of broadband MT stations by Harinarayana et al., (2006). The location of a shallow conductive body (5-25 Ωm) several hundred metres thick was related to the hot water of the coincident geothermal reservoir, resting on top of the resistive basement rocks. The conductive zone generally terminated at the location of the bounding faults to the thermal zone, further corroborating the validity of the MT result. A deeper, previously unknown conductive anomaly was discovered beginning at 2 km and exhibiting low resistivities of less than 10 Ωm and was interpreted as the cooling magma chambers that act as a source of heat for the geothermal reservoir. MT studies by Wannamaker (2007) were also able to characterize the source of a geothermal reservoir in the Dixie Valley geothermal region, Nevada. A nearly vertical conductive hydrothermal conduit imaged in the MT inversion (Figure 4.8); the Dixie Valley field is already power producing. The vertical low resistivity structure was linked to high temperature fluids that connect to the surface thermal manifestations. The transition to high resistivity at the borders of the anomaly is the interface with basement rocks, corroborated by the extant wells 41-22 and 62-21. The results successfully image the magmatic source of the thermal fluids in the Dixie Valley.
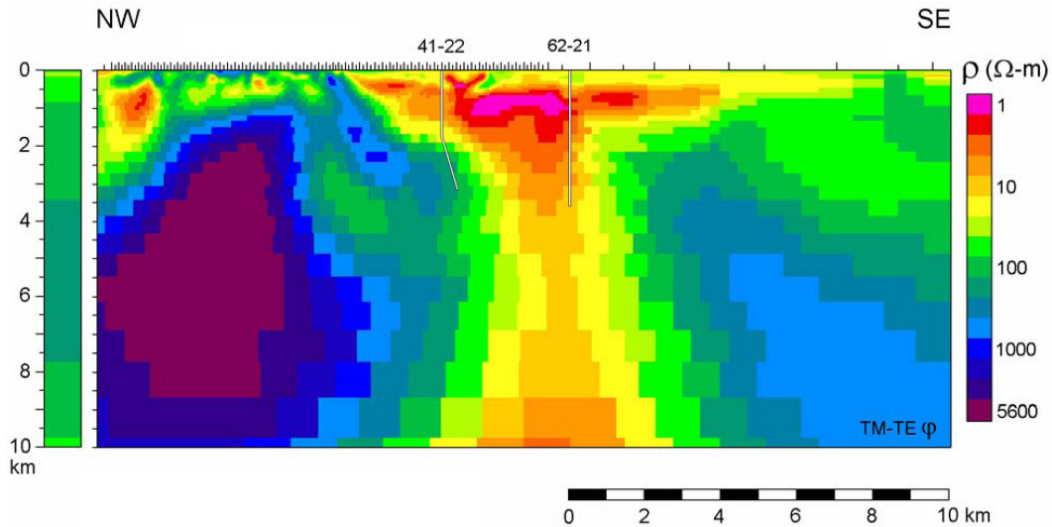
Figure 4.8: From Wannamaker (2007). Figure is a 2-D MT inversion of 120 MT sites across the Dixie Valley geothermal field. Deep wells are present and indicated by "41-22" and "62-21".

Another example of MT being used to investigate geothermal sources comes from the Coso field in California studied by Newman et al., (2008). The imaged high conductivity anomaly was related to the classic arrangement of smectite clays sitting above the less conductive hydrothermal reservoir that was known and already exploited. The full 3-D inversion of the author's MT grid was found that a series of faults acted as the major fluid and heat pathway from depth and bounded individual regions of hydrothermal fluids, which all likely have the same heat source.

Electromagnetic methods, and MT for deep targets, are a very useful especially when used in conjunction with other geophysical techniques, such as seismic reflection and gravity, as the confluence of different measurement parameters can elicit a focus upon the most conducive geothermal regions in a study area (Iovnetti et al., 2009). The conductivity signature of geothermal reservoirs is due to a complicated combination of factors. EM methods of exploration, by measuring conductivity directly and providing

information at depths far greater than other techniques have been of particular use in the search for suitable geothermal zones.

4.5   Geothermal Exploration With MT for EGS

The target in regions suitable for EGS development is driven solely by temperature changes. It is therefore desirable to be able to map high temperatures at depth remotely, without expensive well logs. Secondary to temperature it is important to be able to map extant fractures and the path of possible future fractures by analyzing the geoeletric strike. If there isn't a well known geothermal conductivity model, as there is for hydrothermal systems, then any potential conductive sources, such as graphite films, must be considered as well.

A current example of EGS exploration involving MT is the Soultz-Sous-Forêt geothermal zone in Eastern France, which was examined with MT by Spichak & Geiermann (2010). The authors attempted to extrapolate temperatures at depth by comparing MT resistivity measurements with temperature well logs. Schill et al., (2010) attempted to assess the feasibility of other EGS sites in the Upper Rhine Valley by combining MT with density analysis from gravity data. Their 2-D MT inversions, combined with 3-D gravity data inversions, revealed a 2 km deep conductor that was interpreted as saline geothermal fluid residing in fault structures in the granitic basement rocks with an estimated porosity of only 1%.

Conductivity anomalies can arise from many factors; geological studies must be incorporated so that the thermal nature of the rocks in the study region is known. Relevant information includes thermal conductivity, heat flow, and geothermal gradient data. Structural mapping of any possible fracture zones and fluid pathways can provide

possible explanations of the EM resistivity data so that final interpretations, and possible temperature connections, can be made in confidence.

EGS development can require the inducement of fractures as an artificial fluid transport path. Knowledge of the stress state and maximum/minimum stress directions is very important for predicting how such a venture will proceed. The stress direction will control to some degree the orientation of artificial fractures. MT can provide information on the existence and strength of any geoelectric strike of the area as well as any electrical anisotropy, which will work in concert with the stress directions. The determination of the preferred direction and fabric can then be compared to the present day stress direction. The comparison between these directions will affect the propagation of artificial fractures.

Dimensionality and directionality of the electrical structure in the region will be determined in the following chapter. This will aid geological interpretations and allow inversions of the resistivity data. The applicability of 2-D and 3-D inversions will then be discussed and performed where appropriate. The presence of electrical anisotropy will be investigated and the ramifications of inferred widespread anisotropy will influence greatly the final geological interpretations.

Chapter 5

Magnetotelluric Data Analysis

For the purpose of geothermal exploration in the Fort McMurray (FMC) region, magnetotelluric (MT) data were collected, and their analysis will be described in this section. The directionality and the degree of distortion present in the MT data, as well as the implications for the state of the deep crust beneath the Athabasca oilsands region will be presented.

5.1   Data Collection

Data collection in the study area included 94 broadband magnetotelluric sites collected by Phoenix Geophysics and the University of Alberta MT group in 2012. These stations were supplemented with one long period site from the Lithoprobe Alberta Basement Transect collected in the late 1990s (Boerner et al., 2000). At all magnetotelluric stations, electric fields were recorded by measuring the voltage between two non-polarizing electrodes connected with telluric dipoles approximately 100 m long. A total of 5 electrodes were used, 1 at the end of the each of the 4 wires and 1 as a ground close to the instrument. Each electrode was coupled to the Earth by burying it and covering the semi-permeable ceramic bottom with bentonite mud. The measurement of the magnetic field uses different sensors based on the period (or frequency) of the signal being measured. For broadband MT stations, the period band is 0.001 s - 1000 s. Broadband instruments measure the magnetic field with three induction coils that are oriented in the North-South, East-West and vertical directions. These sensors are buried to keep them still and reduce the noise caused by diurnal thermal effects. Long-period MT instruments

record signals from 1 - 10000 s with the three orthogonal magnetic field components recorded using three fluxgate magnetometers buried in a single casing.

The MT sites were placed on two roughly parallel East-West profiles with a site spacing of 500 m, separated by a North-South distance of approximately 20 km as shown in Figure 5.1. The Northern profile was named "FMC North" (FMCn) and the Southern profile "Tower Road" (TR).
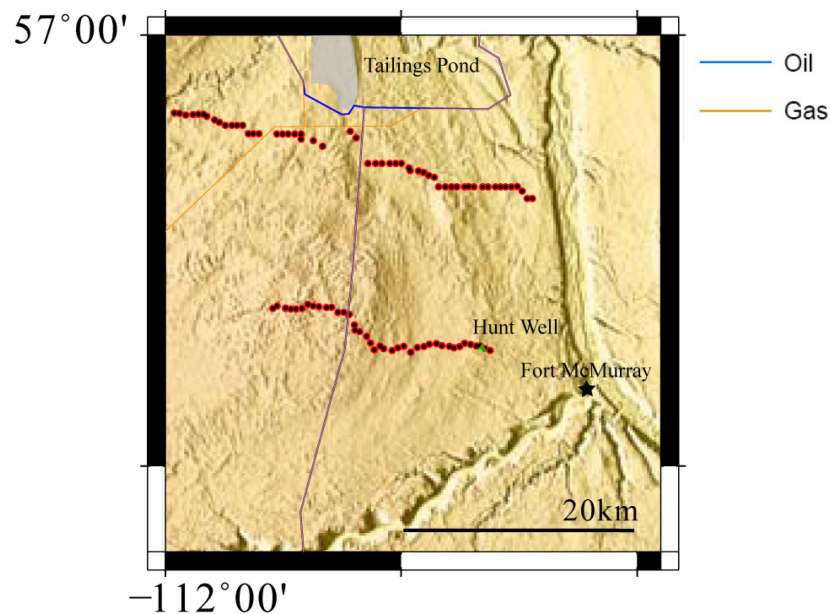
Figure 5.1: Map of the 93 broadband and 1 long period MT stations in the FMC region for this project.. Location of Fort McMurray, the 2.3 km deep Hunt well and a nearby tailings pond are identified. The location of oil and gas pipelines comes from the Pipeline Infrastructure map of Canada from National Resources Canada atlas.gc.ca.

The Lithoprobe long-period site recorded at a continuous 8 Hz sampling rate. The Phoenix Geophysics broadband stations recorded at 2400 Hz for 2 seconds once every 10-minute segment to capture the highest frequency signals and maintain a continuous recording at 150 Hz for lower frequency signals. The University of Alberta broadband stations used three recording bands: 2 discontinuous and 1 continuous. The discontinuous

bands recorded with a sample rate of 2400 Hz for 2 seconds at the beginning of every

other minute. At the beginning of the intervening minutes, the instrument recorded for 16

seconds with a sample rate of 150 Hz. The continuous recording used a sample rate of

15 Hz. No significant differences in the processed data were found to result from the two

different recording schemes.
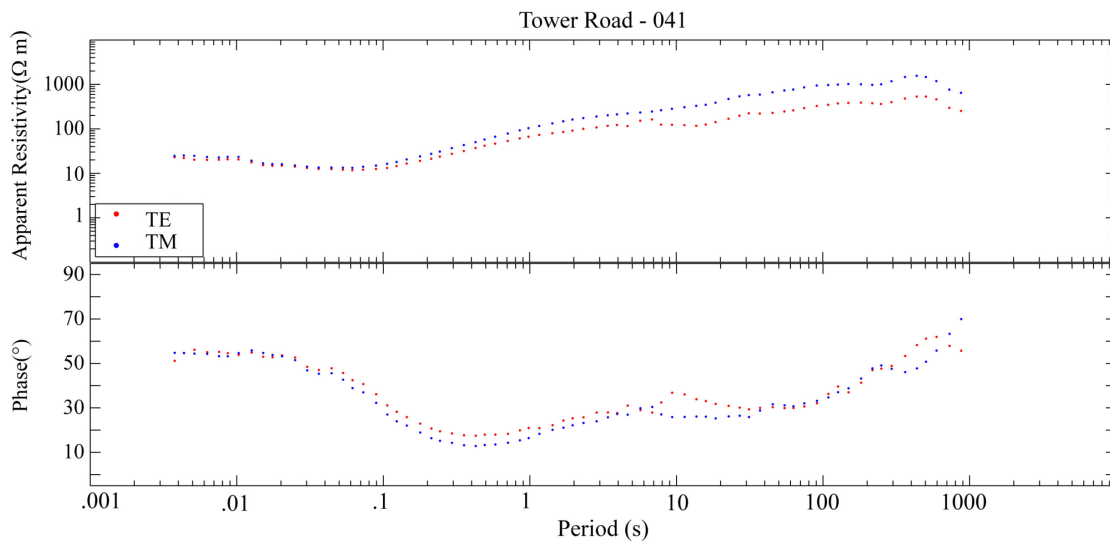
Figure 5.2: A typical MT sounding from the FMC region that is characterized by relatively 1-D MT data, station TR041. The top panel shows the apparent resistivity as a function of period while the bottom panel shows the phase, each calculated from the complex impedance tensor. This sounding is presented in geographic coordinates (0° rotation).

As discussed in Chapter 2, MT data are generally recorded in the time domain, but

interpreted in the frequency domain. This means that processing must use a Fourier

transform to generate frequency domain estimates of impedance. The processing involved

robust estimation of geomagnetic transfer functions as described by

Egbert & Booker (1986), and signal periods ranged from 0.001 s to 1000 s. The

processed data from all sites is typified by the sounding shown in Figure 5.2 that shows

how apparent resistivity and phase vary with period. As with most of the soundings

collected in this study, this sounding shows a low apparent resistivity at short period (shallow depth) that can be identified as being due to the low resistivity rocks of the sedimentary basin. At longer period, the apparent resistivity rises, indicating the presence of resistive crystalline rocks at greater depth. The two curves denote apparent resistivity computed with the north-south and east-west electric fields, the TE and TM modes, respectively, from Chapter 2. When these two curves coincide, it suggests a 1-D resistivity structure. At longer periods the curves diverge, indicating possible 2-D or 3-D resistivity structure. At the very longest periods, the apparent resistivity begins to fall, perhaps due to the presence of the Asthenosphere.

To obtain an accurate representation of the Earth's resistivity structure the dimensionality must first be understood. If there is a geoelectric fabric to the Earth then the direction of that fabric must be found. Correct interpretation of these qualities can be made more difficult by the presence of distortion and in some cases data may be unusable entirely. The characteristics of the FMC data are analyzed in the following sections before any data inversion or interpretation takes place.

5.2   Dimensionality and directionality of the FMC MT data

Dimensionality analysis of MT data is the determination of whether a 1-D, 2-D or 3-D resistivity model is required to fit the data. Several methods will be used to investigate this property of the FMC data. The goal of this analysis is to determine the direction of the geoelectric fabric at each station and each recorded period band and then look for consistencies between stations. The methods outlined in Chapter 2 will be used.

5.2.1   Tensor Decomposition

 As outlined in Chapter 2 tensor decomposition assumes that the regional resistivity structure is 2-D and that the data are distorted in a frequency independent manner by near surface structures. Tensor decomposition is an inverse problem that finds the 2-D impedance and distortion parameters that give the best statistical fit to the data (McNeice & Jones, 2001). The strike direction determined by this method has an inherent 90° ambiguity and other geological or geophysical evidence must be used to choose between them.

The first step in tensor decomposition of the FMC data is the separate decomposition of each period band. Since depth of investigation increases with period, this gives an initial impression of how the strike direction varies with depth as shown in Figure 5.3. Comparisons may be made between stations to determine how strike direction varies throughout the region. The rose diagrams show results for all stations on both profiles in one plot. The red and blue regions represent the two possible strike directions from the 90° ambiguity. The maps include the station locations and the strike direction pertaining to the blue sector in the rose diagram. The length of the coloured bar shows the phase split which is a measure of how non 1-D the data can be considered. The color of the bar refers to the r.m.s. misfit of the decomposition, and is a measure of whether the assumption that the data are 2-D is valid (see Chapter 2 for an explanation). Colours plotted green have a misfit close to 1 and are statistically acceptable. If the data are only approximately 2-D, then the decomposition can be somewhat unstable but large line lengths and consistent orientation coupled with low r.m.s. misfit values indicate a successful decomposition.
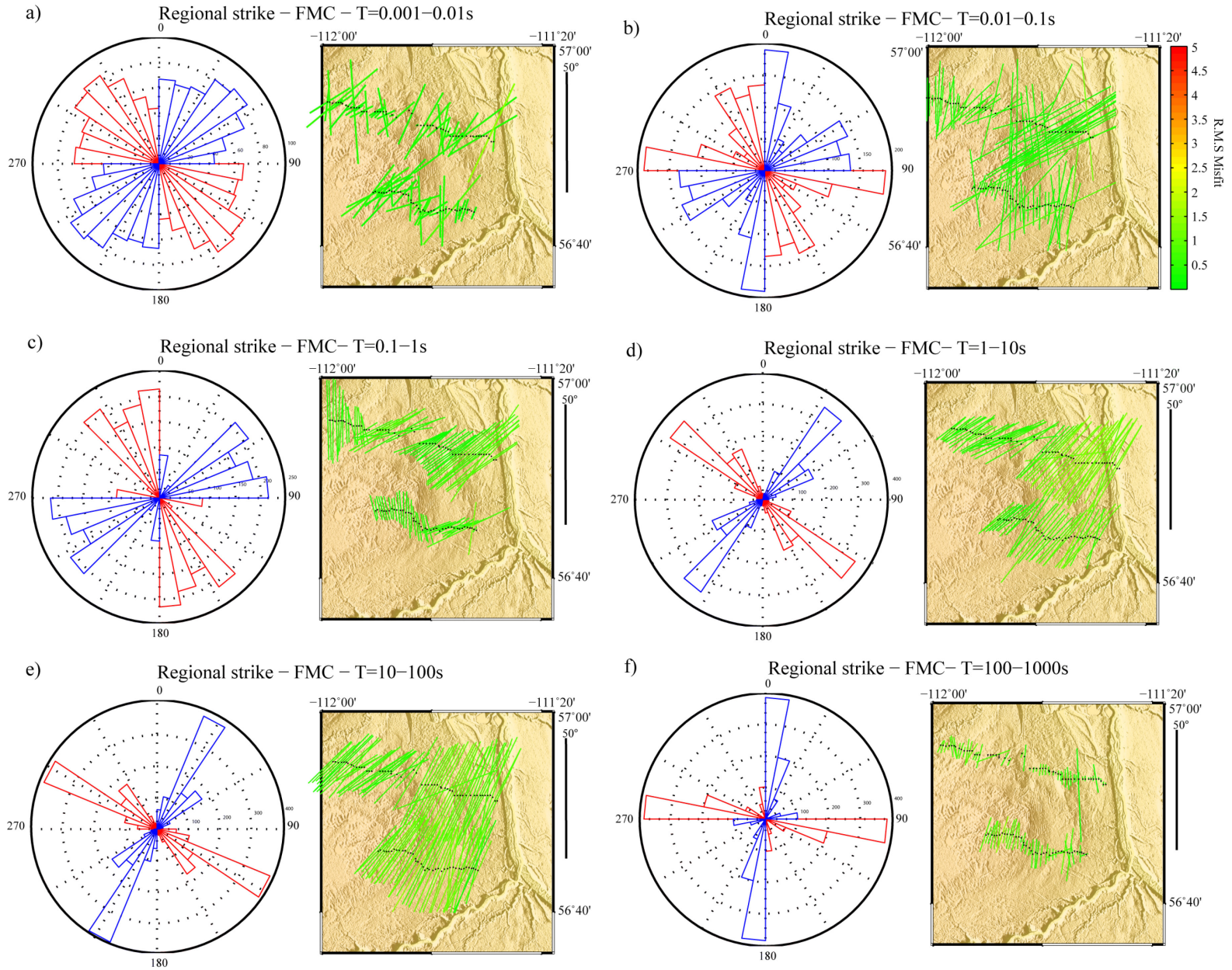
Figure 5.3: Groom-Bailey tensor decomposition for 6 period bands. The rose diagrams show the strike directions for all stations, and blue and red indicate the two equivalent strike directions from the 90° ambiguity in tensor decomposition. The map shows the location of each station and its strike direction from the blue regions of the rose diagram. Length of the lines corresponds to the split between TE and TM modes in the decomposed 2-D tensor, a scale bar for 50° split is shown on the right. Colour relates to the r.m.s misfit of the decomposition from the assumed two-dimensional model, green is r.m.s.=1.

The r.m.s. misfit of the decompositions is close to 1 at all stations and in all period bands. Note that in these decompositions, the algorithm has determined the best-fit strike direction for each station and each period band individually. The agreement between stations is remarkable and shows that Earth resistivity structure is spatially uniform over the survey area. It should be noted that if data quality for a particular period range is too low, the decomposition can fail and give a result of 0°, this effect is most likely to be seen in the shortest and longest period bands, Figure 5.3 (a) and (f).

The first two images, Figure 5.3 (a) and (b), were computed from short period EM signals that penetrate no further than the base of sedimentary basin. At these shallow depths, there is no preferred direction and therefore no consistent strike direction is found by the tensor decomposition. The implication is that a 1-D resistivity structure is being sampled by data in the period range 0.01 s to 0.1 s.

Figure 5.3 (c), (d) and (e) show the decomposition result of data in the period range 0.1 s - 100 s. At these periods the strike directions begin to show a systematic variation across the survey area. Figure 5.3 (c) does not have as large a split as (d) or (e) and may indicate that 0.1 s to 1 s is a band of transition from 1-D to higher dimensional resistivity structure.

Figure 5.3 (d) and (e) show that in the period band 1 s - 100 s there is very well defined 2-D strike direction over the entire region. MT stations at these period bands seem to display a strike direction near to N40°E in the East and closer to N60°E in the West. These period bands are said to have a 2-D strike, and directional dependence.

Figure 5.3 (f) shows that for data in the periods range 100 s and 1000 s there is no well-defined strike direction. Short (small phase splits) and inconsistent line lengths mean that despite the low r.m.s. misfit no regional strike direction is discernible. Both Jones &

Munro (2002) and Nieuwenhuis (2011) showed with long-period MT stations that for periods beyond 1000 s in Alberta complicated 3-D effects become important. This is consistent with these data; at some point between 100 s and 1000 s the FMC data no longer characterized by a well-defined strike direction.

The second step in tensor decomposition is to find the best strike direction for data at all period bands at once; the results are shown in Figure 5.4. This is still an unconstrained decomposition because the code is able to find the best-fit strike direction for each station individually. The four rose diagrams show the tensor decomposition results for the whole survey (top) and for the individual subgroups (bottom). Two distinct strike direction regimes can be identified:

(1) Stations on the TR and FMCn East profiles have a strike direction of N40°E.

(2) Stations on the FMCn West profile have a strike direction of approximately N60°E.

In each group there is very little spread in the rose diagrams, indicating similar results at every station. The r.m.s. misfit increases slightly to the East in the FMC region, reaching a value of approximately ~2, which is still a reasonable fit.
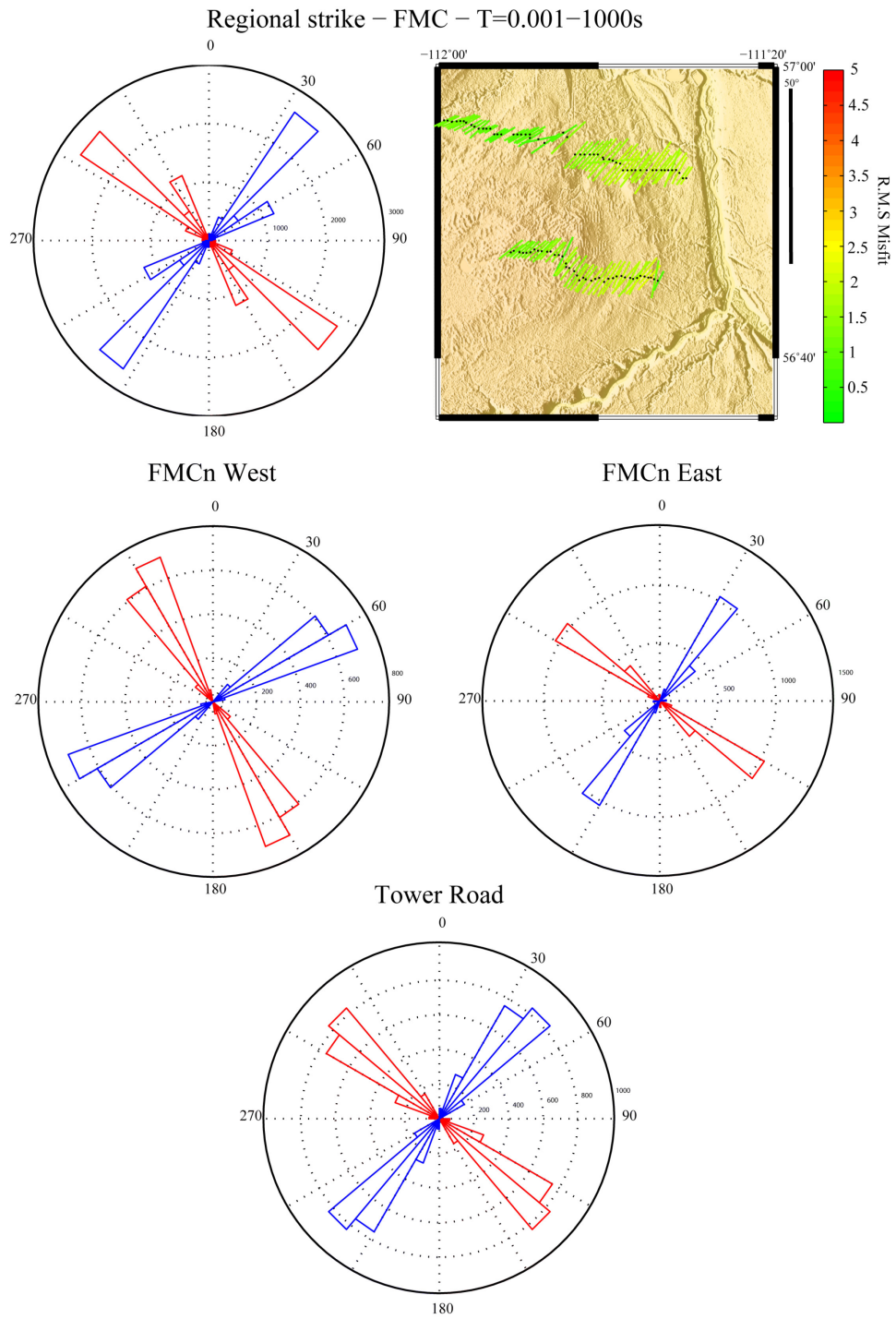
Figure 5.4: Best-fitting regional strike in the FMC region, periods from 0.001 - 1000 s were used for each station. The top left image is the rose diagram including the strike direction of every station, blue and red indicate the two equivalent strike directions coming from the 90° ambiguity in tensor decomposition; the right image is the map view of the tensor decomposition, similar to Figure 5.3 but for all period bands at once. A scale bar of 50°, and a color scale of the r.m.s. misfit, are presented next to the top right image. The lower three rose diagrams are for each profile individually.

The distortion parameters estimated by the unconstrained decomposition in Figure 5.4 are shown in Figure 5.5. Twist and shear angles are plotted in the upper panel and have acceptably low values with only a few outliers. The Easternmost four stations on TR are severely distorted, which could be due to their close proximity to the 2.5 km deep Hunt well. The first 1 km of the Hunt well from the surface has a steel casing, which is very conductive. Current channeling is a known distortion effect in MT data (Chapter 2) and channeling of electric currents along the casing could have distorted the recorded MT data. The bottom panel shows the r.m.s. misfit of the decomposed 2-D tensor to the original impedance tensor at each site. A low r.m.s. misfit combined with low distortion parameters is a validation of the assumptions made in tensor decomposition. On both the FMCn and TR profiles, the r.m.s. misfit increases to the East, meaning stronger distortion is required to fit the data than in the West. The FMCn profile shows a noticeable split almost exactly halfway along the profile, while on each side of the split the misfit is relatively constant. The result of this second step of tensor decomposition is that there appears to be a well-defined strike direction for each station, and a 2-D regional impedance structure appears to exist.
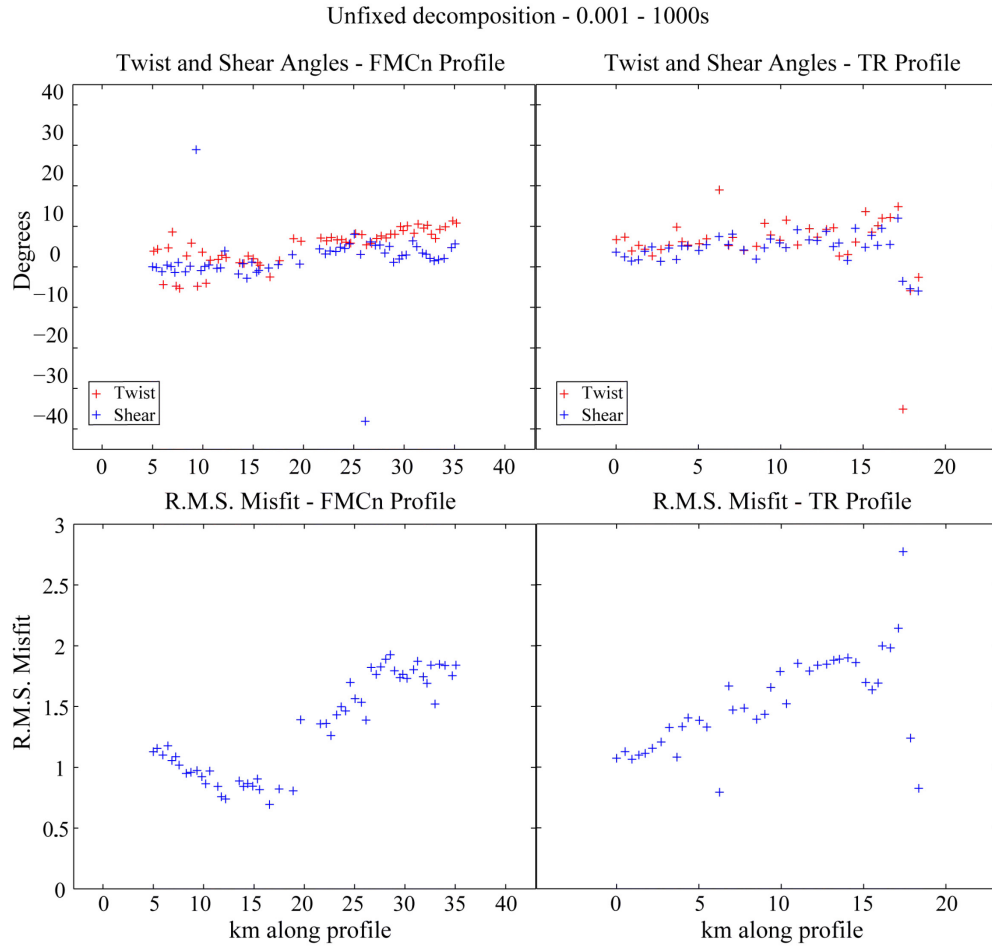
Figure 5.5: (Top) The twist and shear angles estimated from the tensor decomposition for both the FMCn and TR profiles. (Bottom) r.m.s. misfit of the 2-D decomposition compared to the original data. All results calculated using all periods with no bound parameters. The final four stations on TR are subject to unique distortion levels likely because of their proximity to the Hunt well.

The third step in tensor decomposition is to perform tensor decomposition for all MT stations and all frequencies simultaneously to find a single strike direction for all stations at once. If a 2-D interpretation is appropriate for these MT data, then a common strike direction at all stations and frequencies must be found. This is a constrained decomposition because the strike direction is fixed to a set of angles ranging from N20°E to N80°E in 3° increments. At each angle the misfit for all frequencies and stations was

95

computed. A plot of r.m.s. misfit as a function of constrained strike direction is shown in

Figure 5.6. The full period band, 0.01s to 1000s, was used in this decomposition.
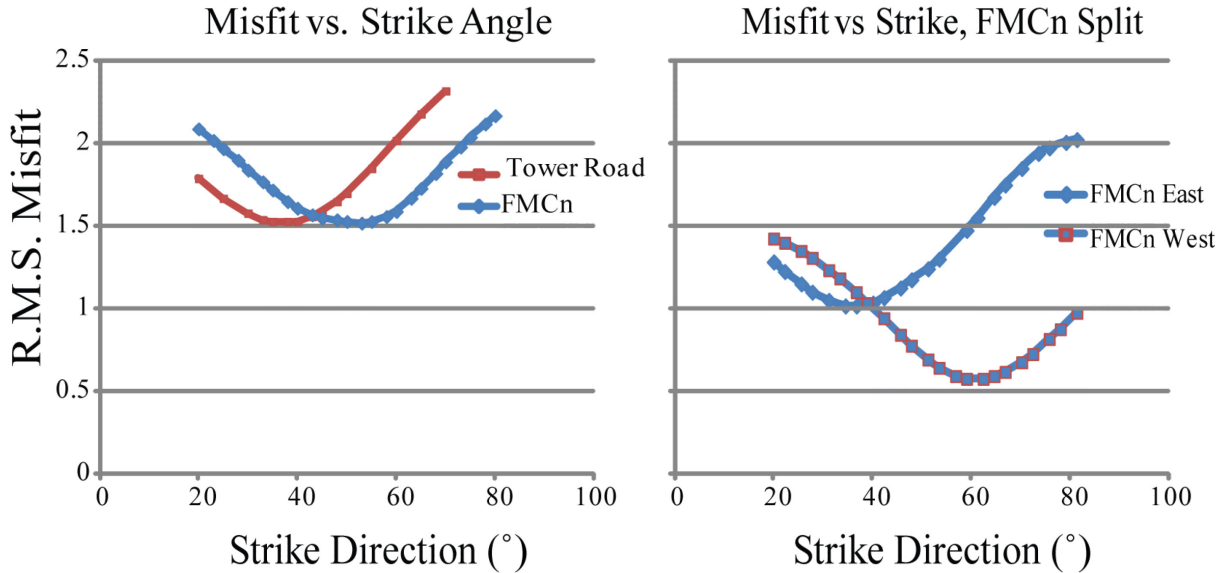
Figure 5.6: Plots of r.m.s. misfit for the multi-station tensor decomposition at a variety of imposed strike angles. The left image shows the misfit as a function of strike angle averaged over the Northern and Southern profiles separately. There is a difference between the two minima of nearly 20°. The right image was produced by splitting the Northern profile into two parts station FMCn135.

The left image in Figure 5.6 shows the r.m.s. misfit when all stations on the TR and

FMCn profile were analysed together. The right panel shows the r.m.s. when the FMCn

profile is split into Eastern and Western halves as with the rose diagrams in Figure 5.5.

The Tower Road profile has a lowest misfit for a strike direction of N40°E and the FMCn

profile has a minimum misfit for a strike direction of N57°E. The source of this

difference can be understood when the FMCn profile is split into East and West

segments, as shown in Figure 5.6. The strike direction of FMCn East agrees well with the

strike direction of the TR profile, N40°E, however it can be seen that the FMCn West

profile has its lowest misfit with a strike direction N63°E. The distortion parameters for

the best-fit strike directions in Figure 5.6 are plotted in Figure 5.7. Two distinct groups

appear in the distortion parameters between the stations of FMCn East and FMCn West.

This is strong evidence for splitting the single FMCn profile into two separate profiles for

further analysis.
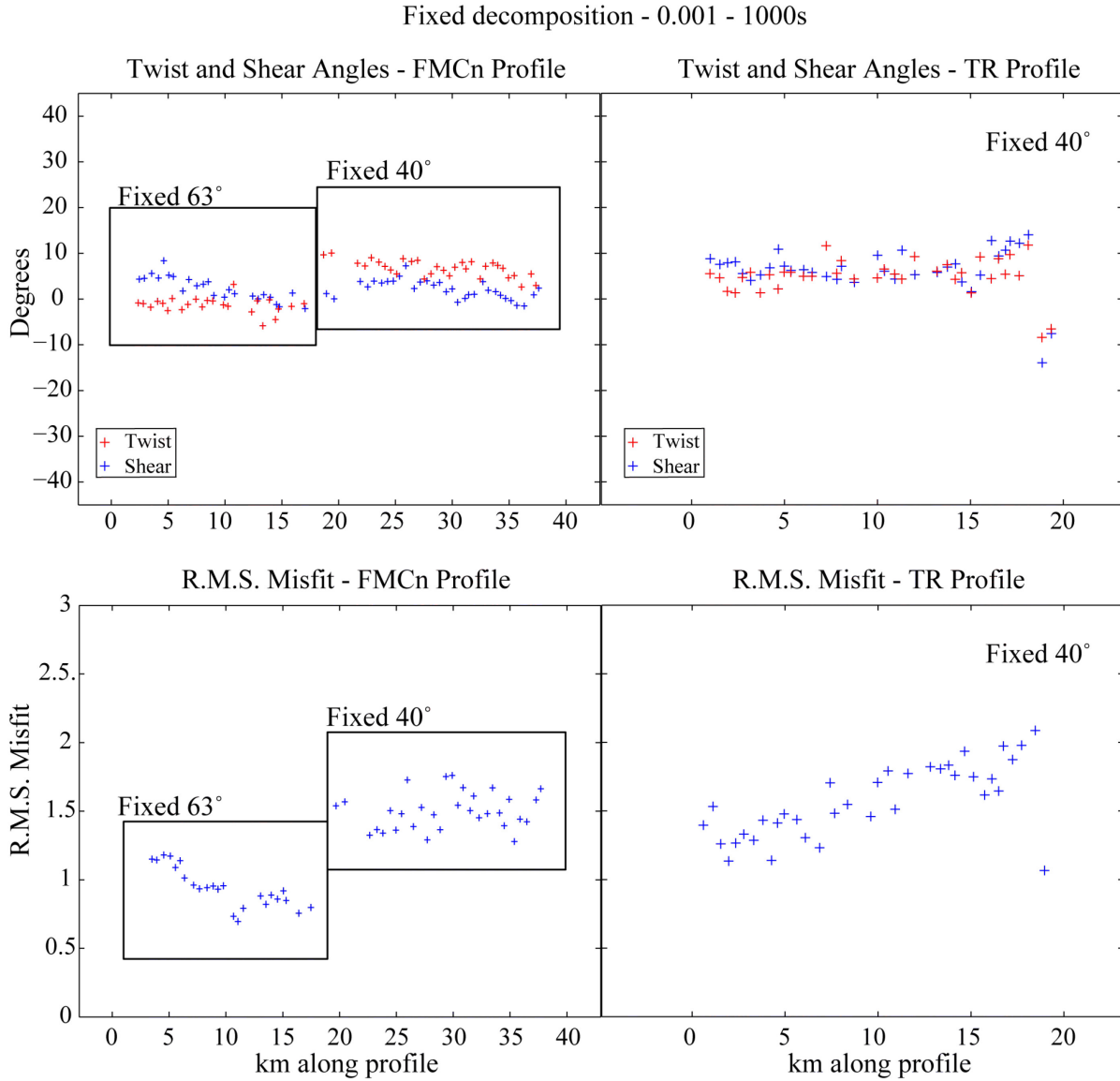
Figure 5.7: (Top) the twist and shear angles estimated from the tensor decomposition in for both the Northern and Southern profiles with the best fit strike imposed. (Bottom) individual station results for r.m.s. misfit of the decomposition to the original data the average of which was the lowest for any strike direction. FMCn is easily split based on these parameters. Distortion parameters are shifted upwards slightly from the low values in the Western half and the r.m.s. clearly has two separate regimes in FMCn. TR has an increase in r.m.s. with easting but no unreasonable values.

Recall that there is a 90° ambiguity in the strike direction determined from tensor decomposition. The strike directions results from Figure 5.6 of N40°E and N63°E could equivalently have been N50°W and N27°W. Previous MT studies in Alberta (Boerner et

al., 2000; Jones & Munro, 2002; Nieuwenhuis, 2011) used the orientation of geological boundaries and induction vector directions to choose the value of N45°E, as opposed to N45°W. This preference is also used in this thesis.

5.2.2   Induction Vectors

The induction vectors, presented in chapter 2, can be valuable when investigating MT data dimensionality. They are calculated from the vertical magnetic field data and are sensitive to lateral changes in Earth resistivity structure and can sometimes be used to resolve the 90° ambiguity in strike direction derived from tensor decomposition (See Chapter 2). In this thesis, the induction vectors are plotted using the Wiese convention (Wiese, 1962), in which induction vectors are plotted to point away from conductors.

Figure 5.8 shows the induction vectors for both the TR (a) and full FMCn (b) profiles as pseudosections. The upper image shows the induction vectors plotted in map view with their true geographic orientations, and north upward. The location of pipelines that cross the profiles (Figure 5.1) are indicated. The lower, coloured, images show the full magnitude of the induction vectors. Recall that over a 1-D Earth the vertical magnetic field component is zero, and thus the induction vectors have zero magnitude.

a)

FMCn - Induction Vector Pseudosections

b)

Tower Road- Induction Vector Pseudosections
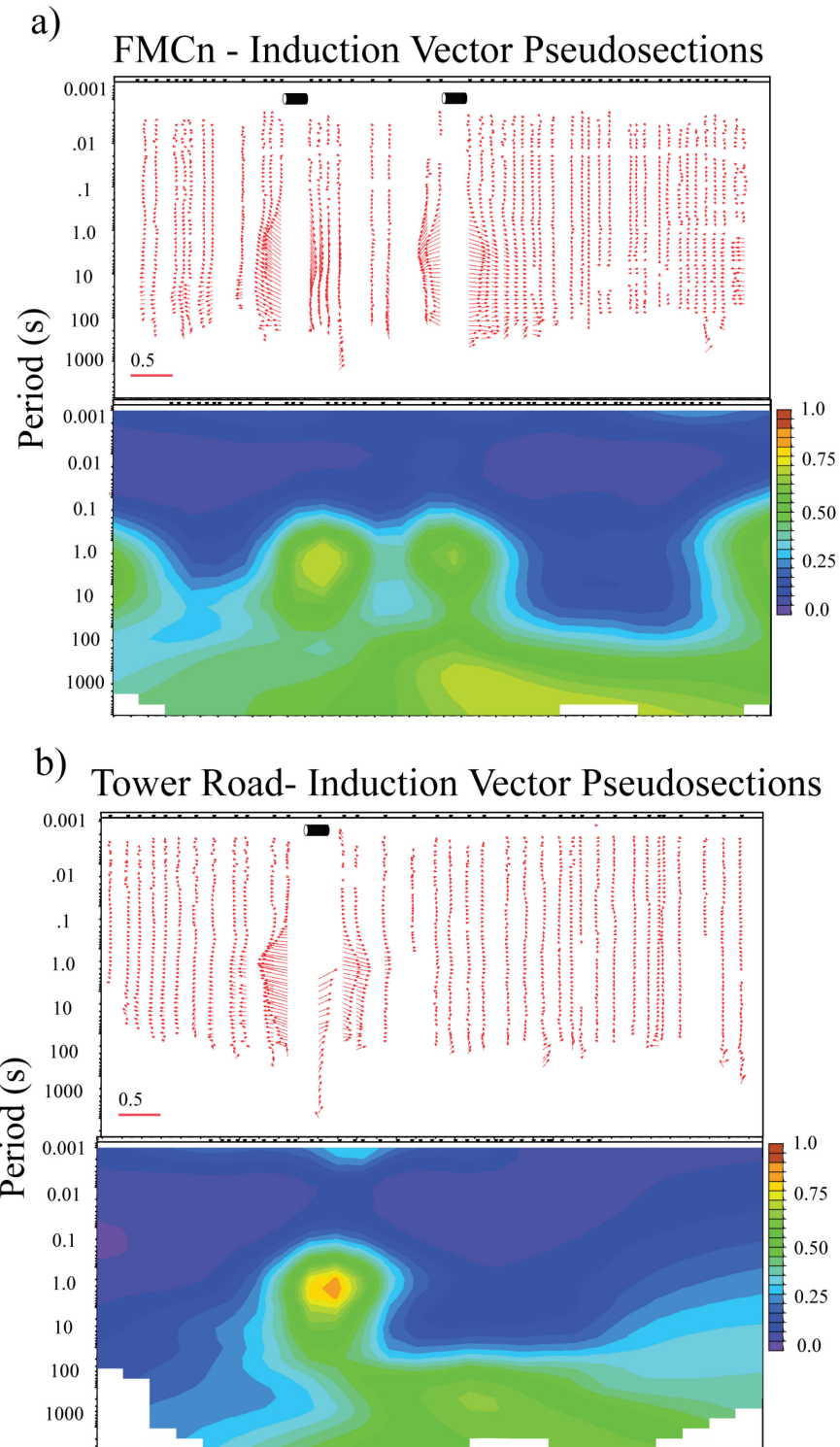
Figure 5.8: Real components of the induction vector pseudosections for the FMCn line (a) and the Tower Road line (b). Upper image is the vectors in map orientation using Wiese convention (pointing away from conductors). Scale arrow is in the bottom left. The lower image is the interpolated magnitude of the vector in the profile plane. Location of the pipeline trace across each profile is represented by the black pipeline symbol near the top of (a) and (b).

The pipeline symbols near the top of Figure 5.8 (a) and (b) show the location of the intersection of the pipeline network of Alberta (map view in Figure 5.1) with the profiles. The orientation of the induction vectors are generally parallel to the profile when they are non-zero, which corroborates the East of North choice of strike above. There are three regions of very high magnitude values (~0.8) that stand out and occur at the same point as changes in direction, indicating the presence of conductors.

The correlation of the large magnitude induction vector reversals and the pipeline locations in both profiles is impossible to ignore. Each of the three large magnitude reversals in the induction vectors data can be associated with an oil or gas pipeline. It is unclear why the shallow gas and oil pipelines in the region should create signals that affect the tipper at such long periods but there can be no doubt that the major cause of the large magnitude induction vectors in the center of the profiles are these pipelines. Because of the pipeline noise, much of the induction vector data was removed so that only those vertical magnetic field transfer functions that contained true regional structure information remained. Figure 5.9 is the pipeline noise edited version of Figure 5.8.

After editing the data influenced by pipelines, the remaining data in Figure 5.9 is characterized by low magnitude induction vectors (< 0.2) with no consistent orientation. This implies that there is limited lateral variation in conductivity at the depths sampled by the measured data in the period band 0.001 s - 100 s. Near to a period of 100 s there is an increase in magnitude of the induction vectors although their orientation is scattered and likely due to noise. These low magnitude induction vectors do little to help in strike determination.

a)

b)
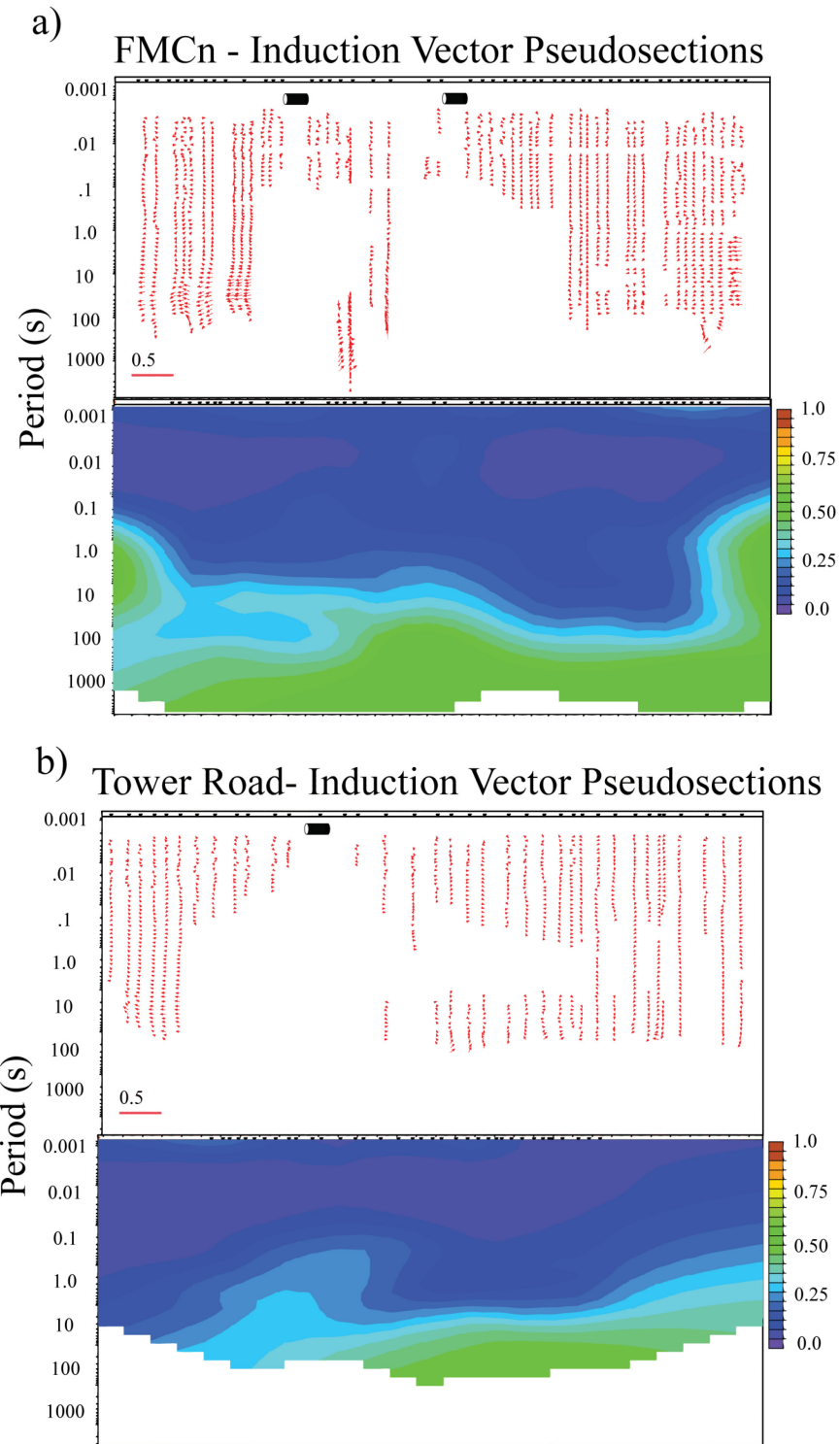
Figure 5.9: Real component induction vector pseudosections for the FMCn line (a) and the Tower Road line (b) post editing of the pipeline effect. Vectors mapped using Wiese convention (points away from conductors). Scale arrow is in the bottom left. The lower image is the interpolated magnitude of the vector in the profile plane. Location of the pipeline trace across each profile is represented by the black pipeline symbol near the top of (a) and (b).

The absence of large magnitude induction vectors, or reversals, shows that there cannot be any major conductors in the study area and that any lateral changes in resistivity must be quite small. Off-profile features could also affect the measured induction vectors, but no such effects are seen.

This observation raises the question of how the tensor decomposition can define a suitable 2-D resistivity structure, while the induction vectors seem to require just a 1-D resistivity structure? One possibility is that off-profile resistivity structure is causing the effect and its induction vector signature is masked by the pipeline noise. Alternatively, as discussed in Chapter 2, this effect may be due to the presence of electrical anisotropy. Electrical anisotropy could cause a strong split between the TE and TM modes while producing small induction vectors (Heise et al., 2006).

5.2.3   Phase Tensors

The phase tensor is a useful tool for dimensionality analysis. Refer to Chapter 2 for a discussion of the underlying theory. The ellipticity of the phase ellipse reflects the split between TE and TM modes. A large split means that ellipticity is large and implies a small error in the azimuth of φ_{max} (Caldwell et al., 2004). The major axis of the ellipse has an azimuth, α, which points in the direction of the maximum inductive current. The skew, β, is a measure of the asymmetry of the phase tensor itself; a skew value above 5° is generally considered to indicate 3-D resistivity structure, although Caldwell et al., (2004) interpreted 3-D with skew values of 3°. Pseudosections of the phase tensor ellipses for both the FMCn and TR profiles are presented below in Figure 5.10 and Figure 5.11.
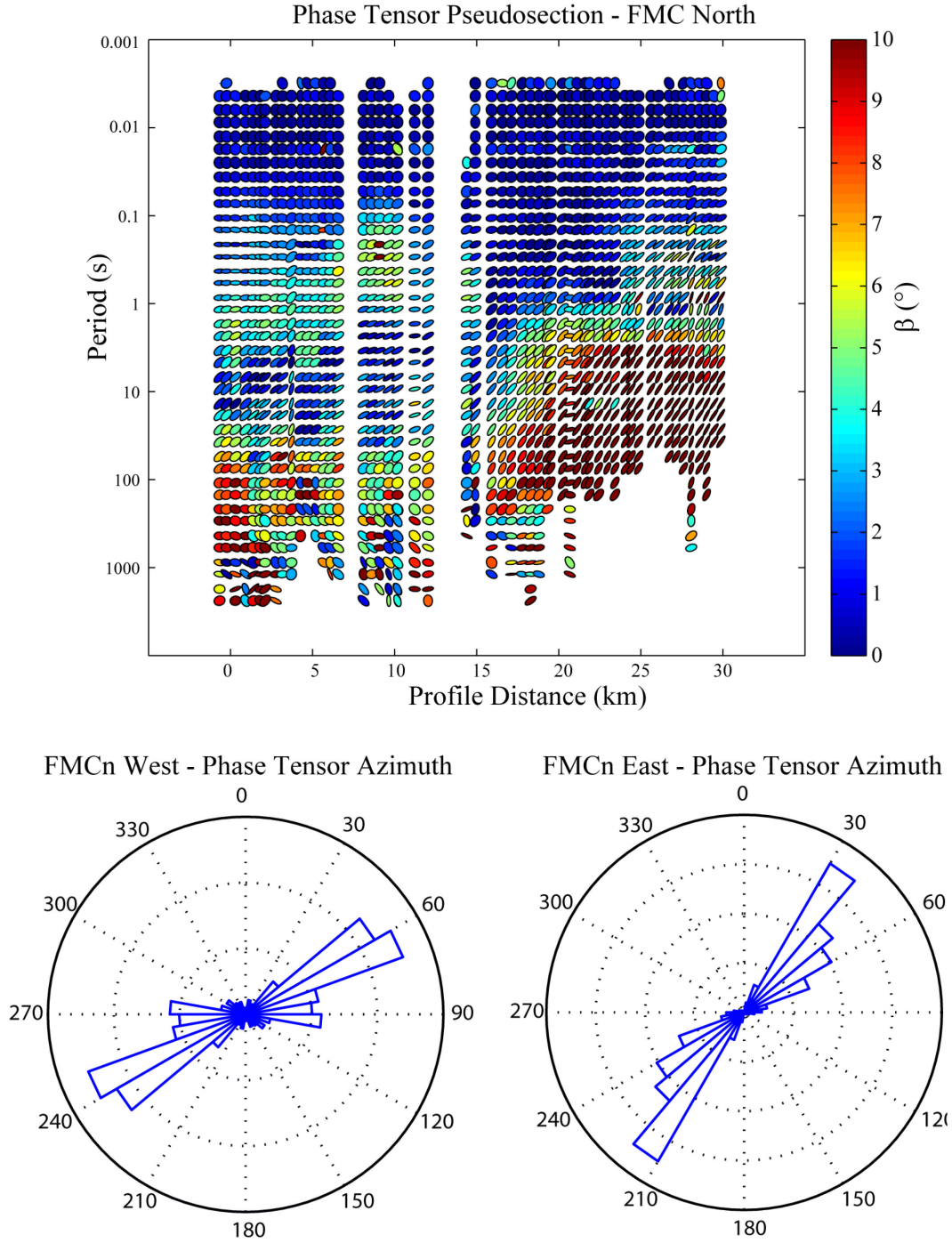
Figure 5.10: Phase tensor information for the full FMCn profile presented as a pseudo section (above) and the orientation of the major axis of the phase tensor ellipses presented as a rose diagram (below). The azimuth can be unstable unless φ_{max} and φ_{min} differ substantially, here the minimum is set to 5° to ensure the diagram portrays a true non 1-D strike angle.
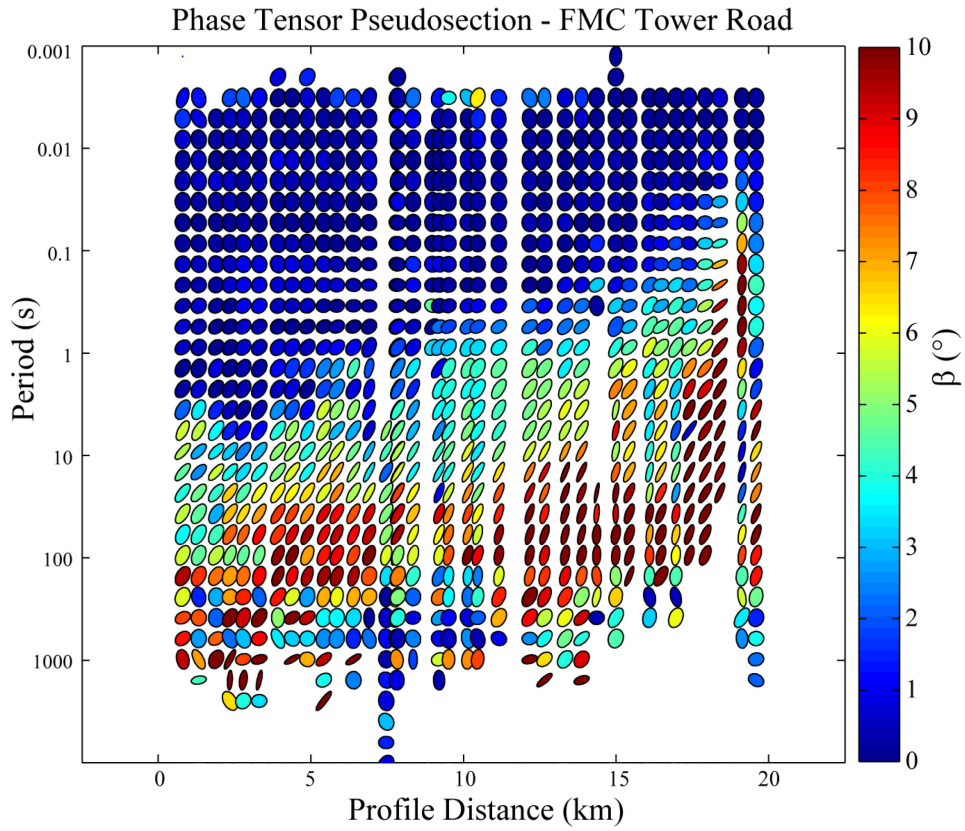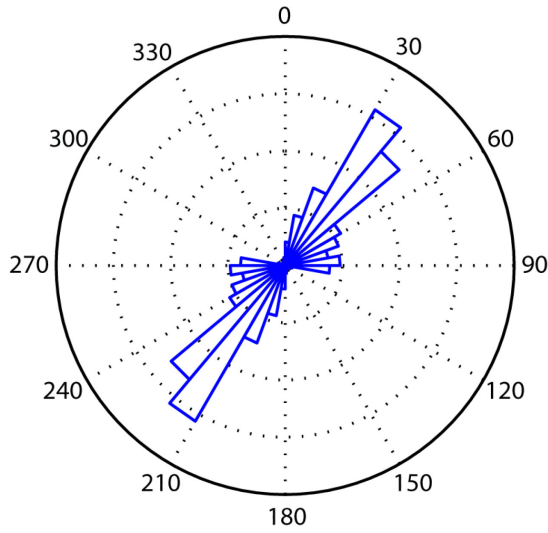
Figure 5.11: Phase tensor information for the TR profile presented as a pseudo section (above) and the orientation of the major axis of the phase tensor ellipses presented as a Rose diagram (below). The azimuth can be unstable unless φ_{max} and φ_{min} differ substantially, here the minimum is set to 5° to ensure the diagram portrays a true non 1-D strike angle

A small value of β is by itself insufficient to interpret 2-D Earth structure; consistency of the phase tensor ellipse azimuth both spatially and with frequency is required.

5.2.4   FMCn East and Tower Road profiles

At periods shorter than 1 s on the TR and FMCn East profiles, the phase ellipses are generally circular and have skew values near to 1°. This combined with the low magnitude IVs and lack of consistent strike direction at these periods from tensor decomposition (Figure 5.3) support a shallow 1-D resistivity structure.

The period bands that had well-defined strike directions in the tensor decomposition can also be seen in the phase tensor data from 1 s to ~300 s. Ellipticity becomes large beginning at a period of 1 s and stays large. The skew angle increases from 0° to more than 10°. The azimuth of the ellipses aligns near to N40°E, as seen in the rose diagrams of Figure 5.10 and Figure 5.11. The azimuths of the phase ellipses do not change by 90° as if they were crossing an interface, instead they maintain their azimuths as if they are sampling a basement halfspace (Chapter 2). It seems clear that FMCn East and TR phase tensor ellipses result from the same Earth structure.

5.2.5   FMCn West profile

The FMCn West phase tensor ellipses do not have the same character as those from FMCn East and TR. No transition of ellipticity or skew begins at 1 s and skew values do not become large until very long periods where 3-D structure may be expected. There is a smaller, shallow, feature that seems to dominate the band 0.5 to 5 s, although it is confined to the FMCn West profile. The rose diagram of phase tensor azimuths for FMCn West matches the 2-D tensor decomposition strike results (~N60°E). The phase tensor features on FMCn West seem to be unique to the profile and not related to the FMCn East

and TR profiles. This is consistent with the tensor decomposition results that put FMCn West apart from FMCn East and TR.

5.2.6   Discussion

It is remarkable that the rose diagrams of phase tensor azimuths match closely with the rose diagrams of the tensor decomposition strike angle in every sub-region. It would seem that the source of the high skew, constant azimuth phase tensors and the 2-D decomposition strike is the same.

If there is little 3-D distortion (low β) then α alone defines the orientation of the ellipse. The skew causes the azimuth of the ellipse to align to α-β instead the equivalent 2-D ellipse that would have an azimuth of α (Heise et al., 2006). Therefore the match between the tensor decomposition strike direction and the phase tensor azimuth incorporates the effect of the skew β on the phase ellipses. The distortion that is causing the high skew values may not be distortion at all, but a systematic signal from some complicated Earth structure that is interpretable.

5.3   Summary of Dimensionality and Directionality

The tensor decomposition showed strong evidence of two-dimensional resistivity structure in all three subgroups of the FMC region. A geoelectric fabric was found to exist at periods longer than 1 s, aligning N40°E for FMCn East and TR, and N63°E for FMCn West (Figure 5.6).

The induction vectors were shown to have been heavily affected by presence of both gas and oil pipelines. After the pipeline effect was removed only the very low magnitude induction vectors in Figure 5.9 remained, making large off-profile conductors or lateral resistivity changes unlikely.

The phase tensors had similar azimuths to these strike directions for all three profiles. The ellipticity and skew value patterns in the phase tensor data suggested that FMCn East and TR sampled the same Earth structure while FMCn West is unique, and less distorted. The split between the FMC subgroups is visualized in Figure 5.12.
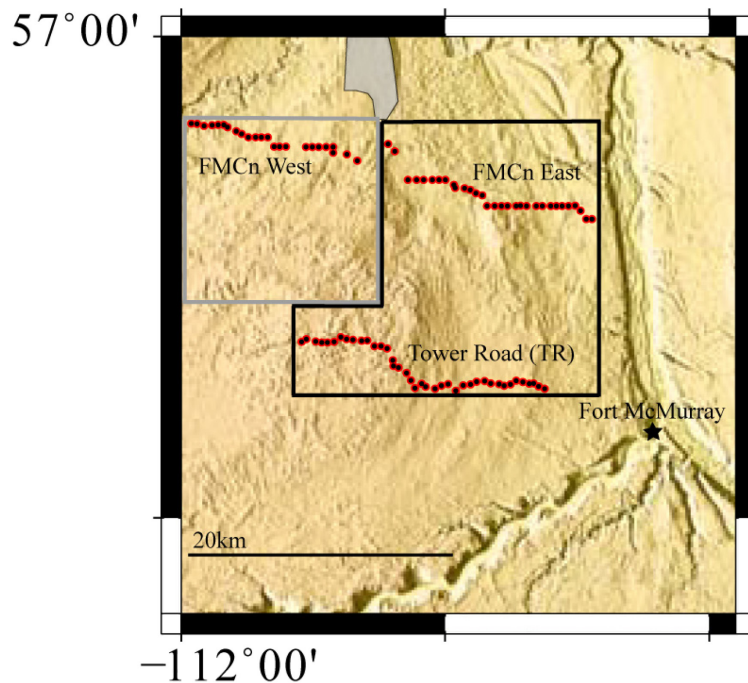
Figure 5.12: Sub-regions within FMC study area defined by strike angle of 2-D decomposition as well as the azimuths and skew of phase ellipses.

The skew values of the phase tensor ellipses from the FMCn East and TR profiles are very large, more than large enough to generally reflect 3-D structure. Skew values change the azimuth of phase tensor ellipses. The azimuths in Figure 5.10 and Figure 5.11 matched the tensor decomposition strike directions, *after being rotated by the skew value*, and for every site in the FMCn East and TR profiles. It is possible that the high skew values do not reflect 3-D structure but consistent and interpretable 2-D resistivity structure.

Chapter 6

Isotropic Inversions of the Fort McMurray Magnetotelluric Data

Chapter 5 showed that the FMC magnetotelluric data were possibly consistent with a 2-D Earth resistivity structure. The next stage is to invert the MT data to find a resistivity model that fits the observed MT data to within a specified statistical tolerance. Inversion is the determination of Earth resistivity structure from measured MT data. An isotropic 2-D inversion assumes that the undistorted impedance tensor is anti-diagonal and that each rock has only one resistivity value (see discussion in Chapter 2).
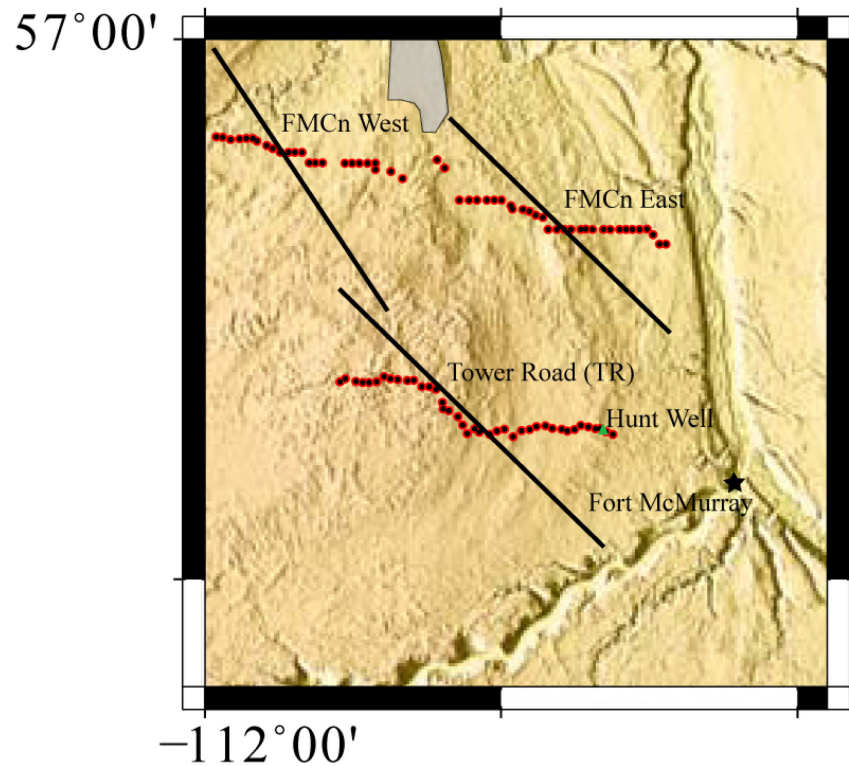
Figure 6.1: Location of the three 2-D MT profiles. The red dots show the location of the all of the MT stations in the FMC region. The black lines are oriented perpendicular to the strikes of each section, N40°E for FMCn East and TR, N63°E for FMCn West. The Hunt Well is indicated by the green triangle

109

Data exhibiting distortion and scatter were removed so that only the MT data meeting the requirements for two-dimensionality were included in the inversions. The MT station located directly beside the Hunt Well experienced severe distortion and was not included in further 2-D analysis; it was the only site that was fully excluded.

The non-linear conjugate gradients (NLCG) algorithm developed by Rodi & Mackie (2001) was used for all the 2-D isotropic inversions. As discussed in Chapter 2, if the subsurface resistivity structure is two-dimensional, then Maxwell's equations decouple into two distinct modes defined by the direction of the electric current flow, i.e., the Transverse Electric and Transverse Magnetic mode. The TM mode has electric currents that flow perpendicular to the strike direction, while the TE mode has electric currents flowing parallel to the strike direction. Each mode is first inverted separately, as each is sensitive to different things, and then jointly with along with the tipper data.

The NLCG inversion algorithm attempts to minimize an objective function that includes both the normalized data misfit and the spatial smoothness of the resistivity model. The inversion process is a compromise between the spatial smoothness of the inversion model and the data fit. A very rough model may have a low r.m.s. misfit, but is likely fitting noise as well as signal, while an overly smooth model may miss important details of the resistivity structure. The choice of model in this spectrum is controlled by the variable τ, which allows a spatially rough, low r.m.s. misfit model if it is small and a spatially smooth, high r.m.s. misfit model is it is large. Performing a number of inversions and plotting the model roughness against the r.m.s misfit gives a trade-off curve between the two parameters. The optimal τ is at the point of maximum curvature. An example of L-curve analysis is shown in Figure 6.2 for a joint inversion of the TE and TM modes

together in the FMCn East profile. A similar analysis was done for every inversion. The inversions were initially run over the period band 0.001 s to 1000 s, which includes the data that was identified to exhibit a 2-D strike in Chapter 5, between periods of 1 s and ~300 s.
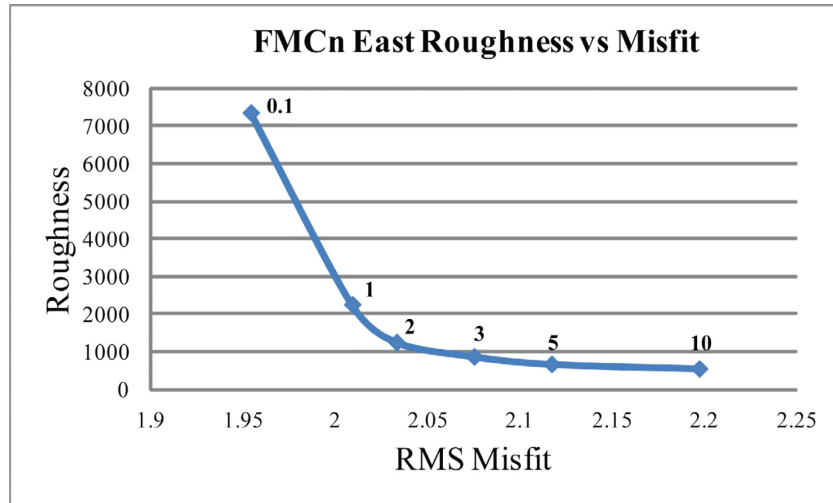
Figure 6.2: Tradeoff L-curve example for the FMCn East profile. Tau values are printed above each point. Large values of tau cause large misfit values due to over smoothing while small values of tau result in very rough models with small misfits. Best choice tradeoff between roughness and r.m.s. misfit is at the point of maximum curvature. In this case the best choice of tau falls between 1 and 3 so 2 was chosen.

The error floor is the minimum allowable error in MT data. If the error bars on a particular data point are smaller than the error floor then they are increased to be equal to the value of the error floor. Changing the values of the error floor parameters can have major effects on the resulting inversion model. A large error floor may cause structure to be ignored, and an unrealistically small error floor can imply accuracy in the data point that is not appropriate. Error floors of 10% for the apparent resistivity and 5% for the phase were used in all inversions as well as 0.05 for the tipper data. These are relatively small values but the FMC data is quite smooth and large error floors were not found to be necessary. The phase error floor was chosen to be lower, since phase data is not affected

by galvanic distortion and therefore should be given more weight in the inversion. The following sections present first the MT data for each profile in pseudosection format, and then introduce the 2-D isotropic inversion models.

6.1   FMC Data Pseudosections

The sounding curves for the three profiles were rotated to their respective best-fit strike directions found in Chapter 5, which were N40°E for FMCn East and TR, N63°E for FMCn West. The data were then projected onto the profiles from Figure 6.1. The station spacing was ~500 m for all profiles. The data are presented as pseudosections in Figure 6.3, Figure 6.4, and Figure 6.5, below.
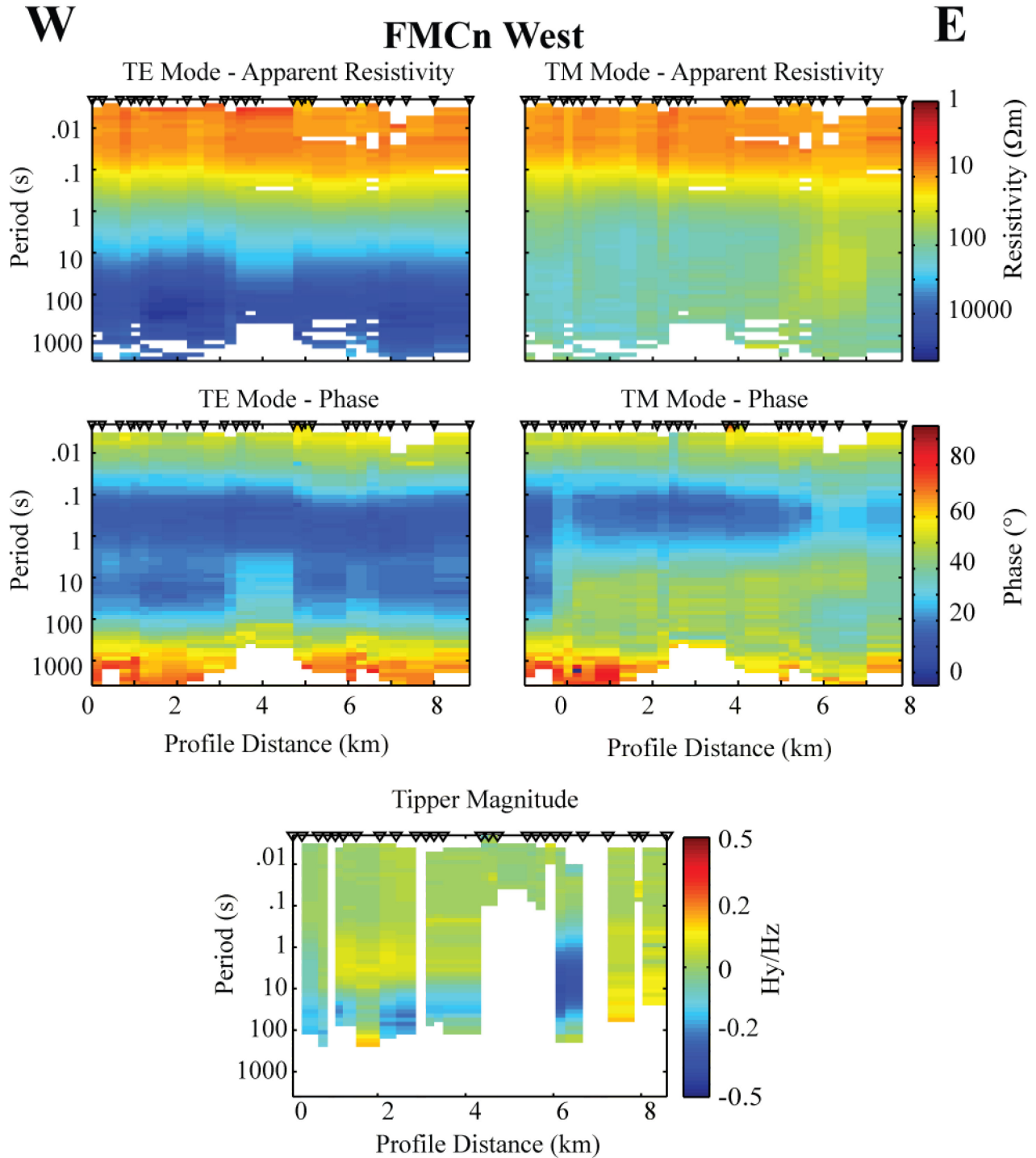
Figure 6.3: The apparent resistivity, phase, and tipper data from FMCn West presented as pseudo sections with signal period. Triangles show the locations of the MT stations after projection onto the profile. The TE and TM mode match until 1 s after which the TM mode is more conductive by an order of magnitude across the profile. Tipper data has been edited to remove pipeline effects and shows no large magnitude features whatsoever. The white areas represent either manually masked or uncollected data.
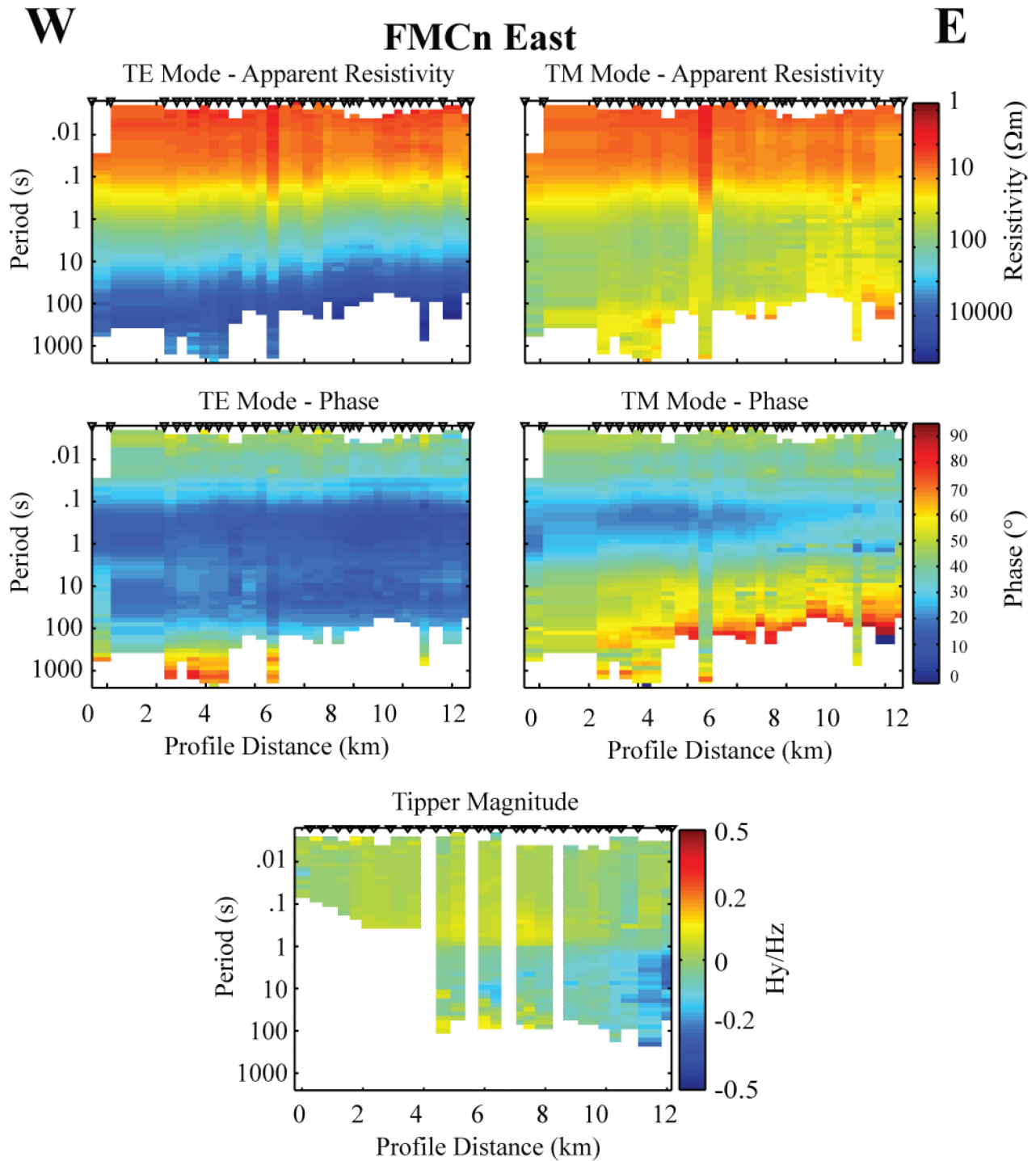
Figure 6.4: The apparent resistivity, phase, and tipper data from FMCn East presented as pseudo sections with signal period. Triangles show the locations of the MT stations after projection onto the profile.

114
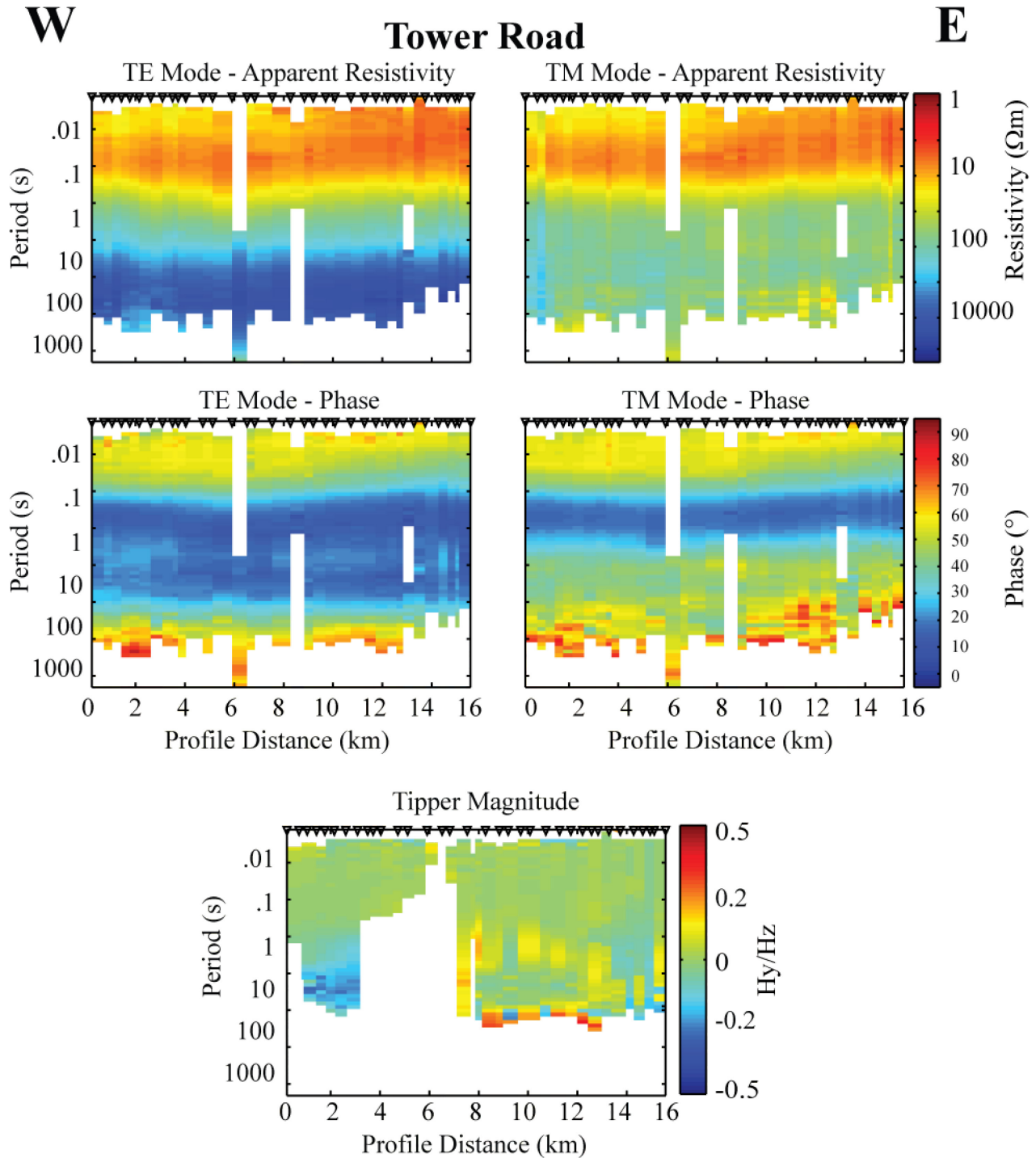
Figure 6.5: The apparent resistivity, phase, and tipper data from the Tower Road Profile presented as pseudo sections with signal period. Triangles show the locations of the MT stations after projection onto the profile. White space represents nonexistent or omitted data.

White spaces in the pseudosections represent non-existent or removed data. All three sets of pseudosections show very little change in the data from station to station. This suggests that the subsurface resistivity structure is quite one-dimensional.

Each set of pseudosections has low resistivity (~10 Ωm), at periods less than 0.1 s in both the TE and TM modes. A split between the TE and TM mode phase data starts at a period of ~1 s. At longer periods, the TE apparent resistivity continues to rise to several thousand Ωm, while the TM mode stabilizes between 50 and 100 Ωm. Much of the tipper data was removed due to the pipeline noise that was discussed in Chapter 5. The remaining induction vector data have relatively low magnitude throughout and do not exhibit any clear sign reversals.

The FMCn West profile has a less pronounced TE/TM mode split than the more Eastern profiles (FMCn East and TR). This could mean that the source of the mode split is more intense to the East and decreases to the West. At periods longer than 100 s for the FMCn East and TR profiles, the TM mode apparent resistivity drops abruptly and the phase begins to rise towards 90°. This is a not a 2-D isotropic effect, all data affected by this distortion were removed. This effect is only seen in the TM mode, but both modes were edited because the data has been rotated so any distortion present in the rotated data must have been originally present in *both* un-rotated modes.

These pseudo sections should be kept in mind when interpreting inversion models. Any feature appearing in the inversion models that is not required by the data are likely due to the application of inappropriate modelling techniques.

6.2   FMC 2-D Isotropic Inversion Results

The resistivity models obtained from the inversion of the FMC data are presented in Figure 6.6, Figure 6.7, and Figure 6.8. The associated r.m.s misfit measures how well the model response matches the measured MT data. Single TE and TM mode inversions are presented first, and then the combined TE, TM and H_Z results. The first TR inversions placed conductive features at the location of the Hunt well, indicating that the effect of the well had not been fully removed. The stations closest to the Hunt well were removed for the "Tower Road Short" and "TE TM HZ" inversions.
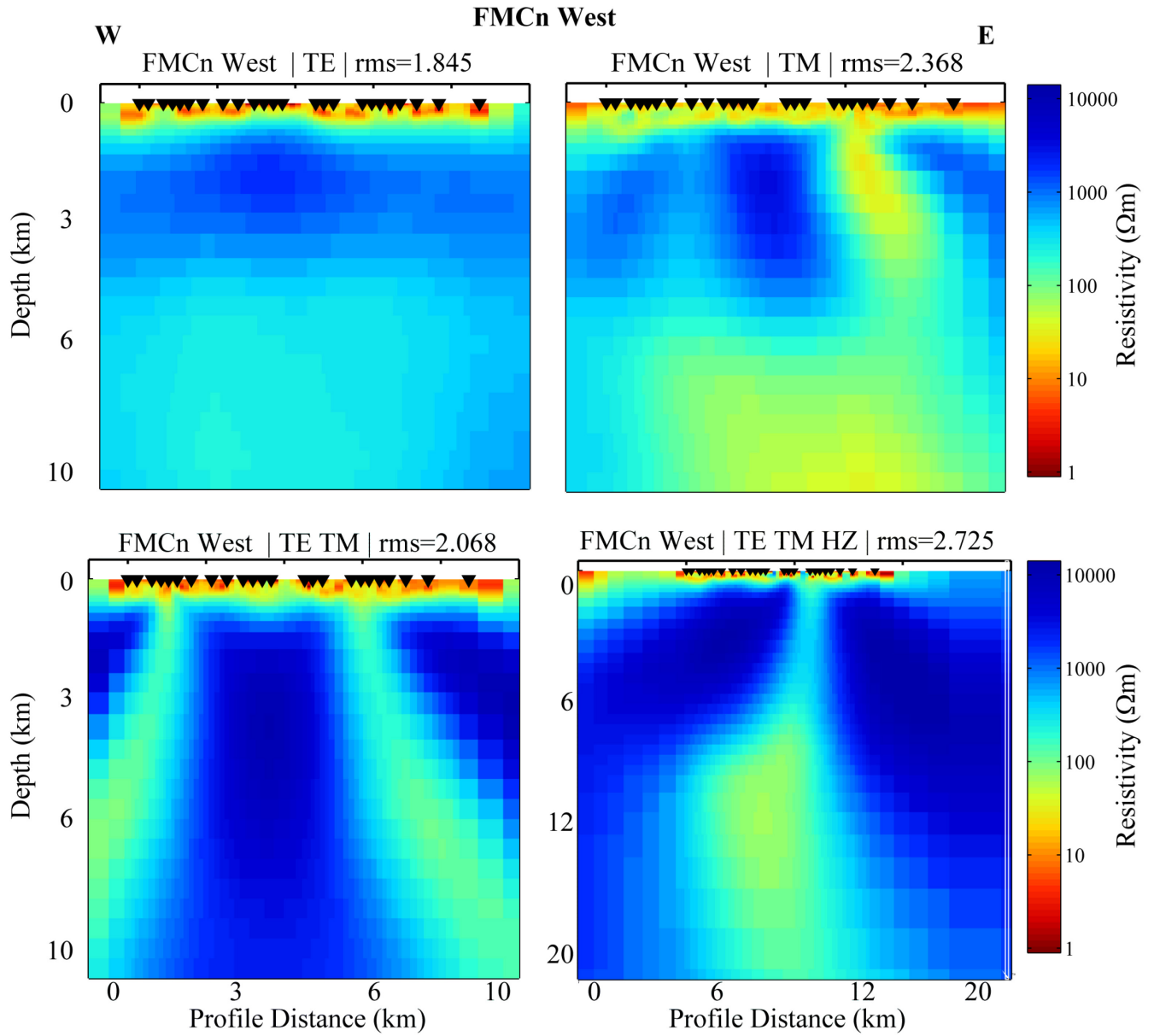
Figure 6.6: 2-D isotropic inversions of the data on from the FMCn West profile. Single mode inversions are shown in the upper two panels, joint mode and full data inversions are in the lower panels. Misfit from data, if not the resulting model, is acceptable in each case.
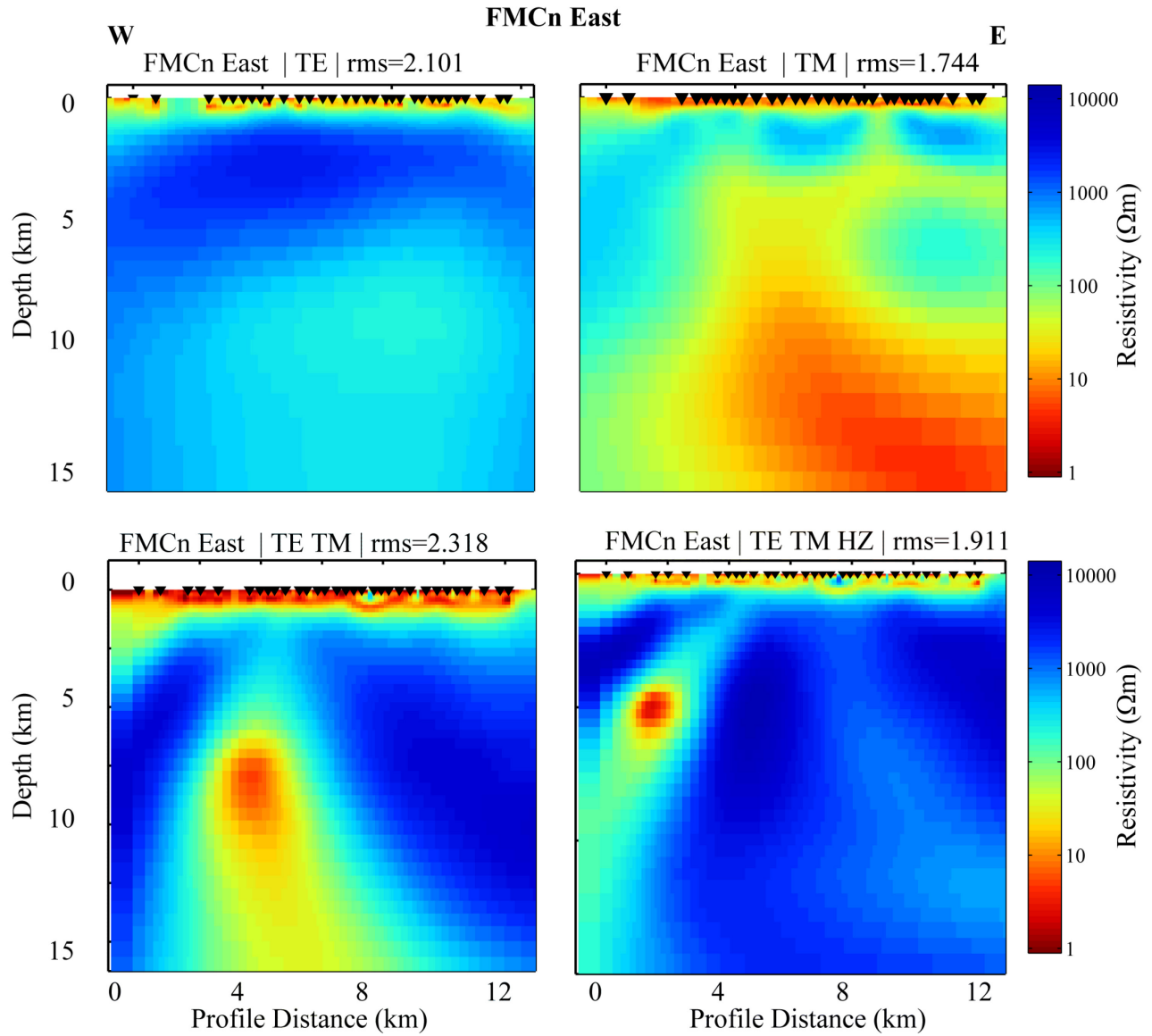
Figure 6.7: 2-D isotropic inversions of the data on from the FMCn East profile. Single mode inversions are shown in the upper two panels, joint mode and full data inversions are in the lower panels. All have reasonably low r.m.s misfit values although the proposed resistivity structure is unrealistic.
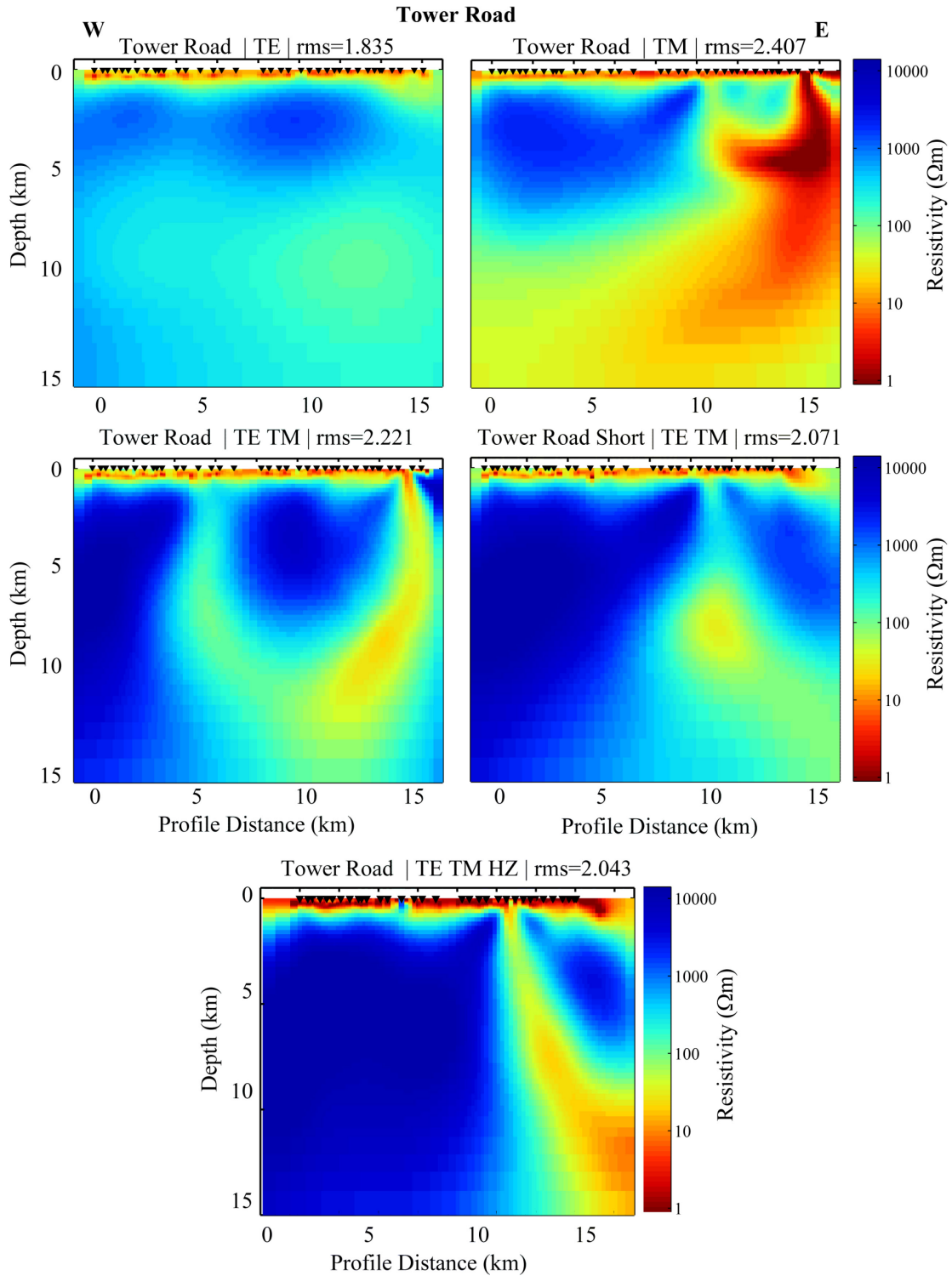
Figure 6.8: 2-D isotropic inversions of the data on the Tower Road profile. Single mode inversions are shown in the upper two panels, joint mode and full data inversions are in the lower panels. All have reasonably low r.m.s misfit values although the proposed structure is unrealistic. "Tower Road Short" refers to inversions in which the Easternmost four sites are removed due to extreme distortion effects.

An interesting characteristic that is shared between the inversions for all three profiles is the low resistivity of the TM mode inversion models compared to the TE mode inversion models. When the TE and TM mode data are inverted together, the inversion models introduce long vertical conductive features. These vertical features are able to reproduce the apparent resistivity split between the uniformly resistive TE and the uniformly conductive TM mode data as evidenced by the low r.m.s. misfit.

Inclusion of the H_Z data in the inversion tends to produce a model that localizes the conductive features in one area, either off-profile (as in FMCn East and TR) or very deep (as in FMCn West). This is because the low magnitude induction vector data from the previous section are incompatible with the vertical conductive dikes generated by the TE-TM inversions.

While the r.m.s. misfit values in all these models are acceptably low, the inversion has generated geologically unreasonable structures to fit the data. The vertical features that characterize the TE-TM joint inversion models are not obvious in the data pseudosections in section 6.1. In a 2-D sense, the long vertical features are conductive dikes that extend into and out of the page. By first excluding all data from periods longer than 1 s it can be seen whether the shallow, short period, MT data require the presence of these vertical features.

6.3   Reduced Bandwidth Inversions

Since the potentially anisotropic TE-TM mode split begins at approximately the same period at all stations (~1 s), isotropic 2-D inversions were performed using just the data in the period band 0.01 s - 1 s. The causes of the differences between the FMCn East and FMCn West profiles are not present at these short periods so all the FMCn stations were

inverted as a single profile. Depths are truncated at 5 km because at a period of 1 s MT is

not sensitive to greater depths. The shortened bandwidth inversions for FMCn and TR are

presented in Figure 6.9.
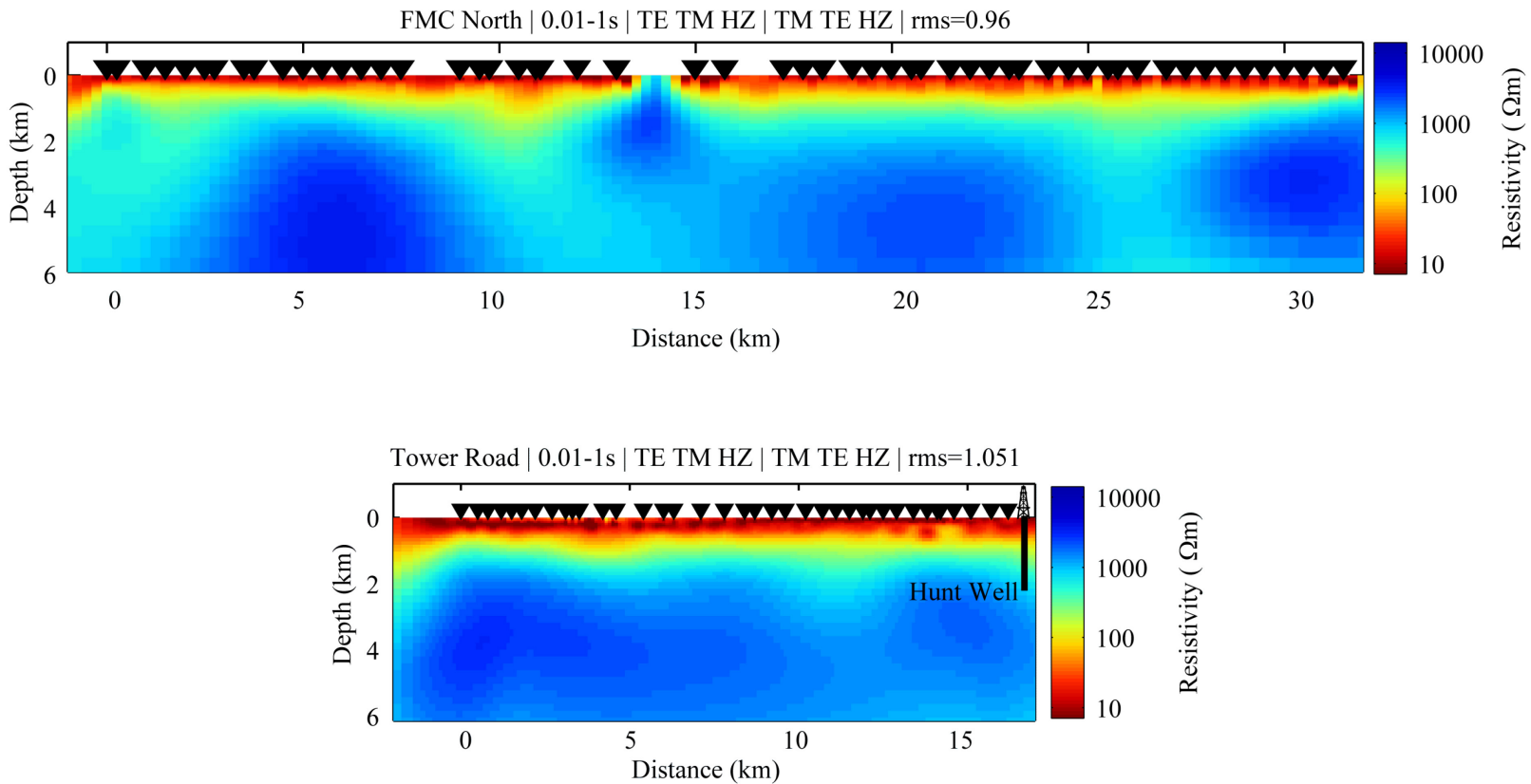
Figure 6.9: 2-D isotropic shortened bandwidth inversions for the full FMCn and the Tower Road profile. Only data at periods 0.01 - 1 s were used in the inversion. Both models have low r.m.s misfit values. Only very small lateral changes in resistivity are observed, the models are of a one-dimensional Earth.

The resistivity models for the FMCn and TR profiles are virtually identical. The WCSB

appears at the surface as a 10 Ωm layer. The Precambrian basement is highly resistive

and there is very little lateral change in resistivity structure. The r.m.s misfit is low and

these inversion models are consistent with the pseudosections presented in section 6.1.

The inversions presented in Figure 6.6, Figure 6.7, and Figure 6.8 contained vertical conductive features that began at shallow depths. No such features appear in the inversion models presented in Figure 6.9. It can be concluded that the long period (> 1 s) data created the vertical conductive dikes, not because they are present in the data, but as an indication of failure of the 2-D isotropic assumption for the data at those periods.

6.4   Summary

Two-dimensional isotropic inversions were applied to the FMC data in the period range 0.001 s - 1000 s. Most of the data from periods longer than 100 s was removed because it exhibited clearly non 2-D isotropic characteristics. The inversion models obtained for all three profiles contained obvious artefacts that were inconsistent with the pseudosections of the data and did not appear in shortened bandwidth inversions. This is believed to be due to crustal anisotropy below a depth of 4 - 5 km. Chapter 2 discussed how inversion of anisotropic MT data with an isotropic algorithm could produce vertical conductive artefacts, similar to the features observed in the FMC inversions.

The TM mode data in the profile pseudosections are less resistive than the TE data, when rotated to the GB strike direction, for all three profiles. In conjunction with the low IV magnitudes, the low resistivity TM mode also suggests the presence of electrical anisotropy. The degree to which the FMC data can be explained with electrical anisotropy will be explained in the following chapter. Anisotropic modelling will be considered, and the model that can best explain all of the features of the FMC data simultaneously will be presented.

Chapter 7

Anisotropic Analysis of the Fort McMurray Magnetotelluric Data

A number of previous studies have interpreted MT data with a subsurface model with anisotropic electrical resistivities and this characteristic of crustal rocks is often related to fossil shear zones in crystalline rocks (e.g. Yin et al., 2014; Eaton, 2004; Weckmann et al., 2003). Electrical anisotropy ranges from micro-anisotropy on the atomic scale, to the scale of individual grains, all the way to macro-anisotropy with length scale of metres or kilometers. Macro-anisotropy is not an intrinsic rock property, but consists of alternating conductive/resistive features, such as graphite films or dike swarms, below the resolvable length scale that can be detected with magnetotelluric signals. The physics of MT means that it is very difficult to determine the exact distribution of the anisotropic conducting phase if its spatial scale is smaller than the resolution limit of MT (Wannamaker, 2005).

Chapter 6 described the results of 2-D isotropic MT inversions and showed that the 2-D isotropic assumption was inappropriate for the FMC MT data. The goal of this chapter is to determine the extent to which the FMC data contains features that may indicate the presence of electrical anisotropy, and whether a 2-D anisotropic resistivity model can explain the data. The components of the MT data relevant to the detection of electrical anisotropy are:

- Out of quadrant phase, caused by current channelling.
- Phase tensor azimuths, skew, and ellipticity analysis
- Large phase splits combined with small magnitude induction arrows

7.1 Out of Quadrant Phase

From the discussion in Chapter 2, only the periods at which there is a TE/TM mode split may be sampling anisotropic structure. Within each profile the mode split begins at precisely the same period, which means that the resistivity structure does not vary in the horizontal direction. FMCn East and TR were grouped together in Chapter 5 by the discussion of strike and phase tensors, but the mode split begins at longer periods at stations on the TR profile. Tower Road shows the same features as FMCn East but at longer period and with less strength. Any explanation of the structure on the FMCn East profile can be extended to the TR profile.

The FMCn East and TR profiles both exhibit out of quadrant phase effects. These data points with out-of-quadrant phase were removed in Chapter 6 during the isotropic inversions. Figure 7.1 shows the unedited apparent resistivity and phase pseudosections for the FMCn East and TR profiles, and the OOQ phase effect is obvious as deep red and deep blue blocks in the pseudo sections at periods longer than 100 s, especially in the FMCn East profile. Recall from Chapter 5 that from West to East in the FMCn East profile there is an increase in distortional effects. The blue sections do not represent low phase values but rather phases above 180° that are wrapped around to -45°. The TR profile does not show the OOQ phase effect to the same degree as FMCn East, and sometimes the phase does not actually leave the quadrant, although it does increase sharply in a similar way. In FMCn West no such anomalous phase is observed whatsoever.
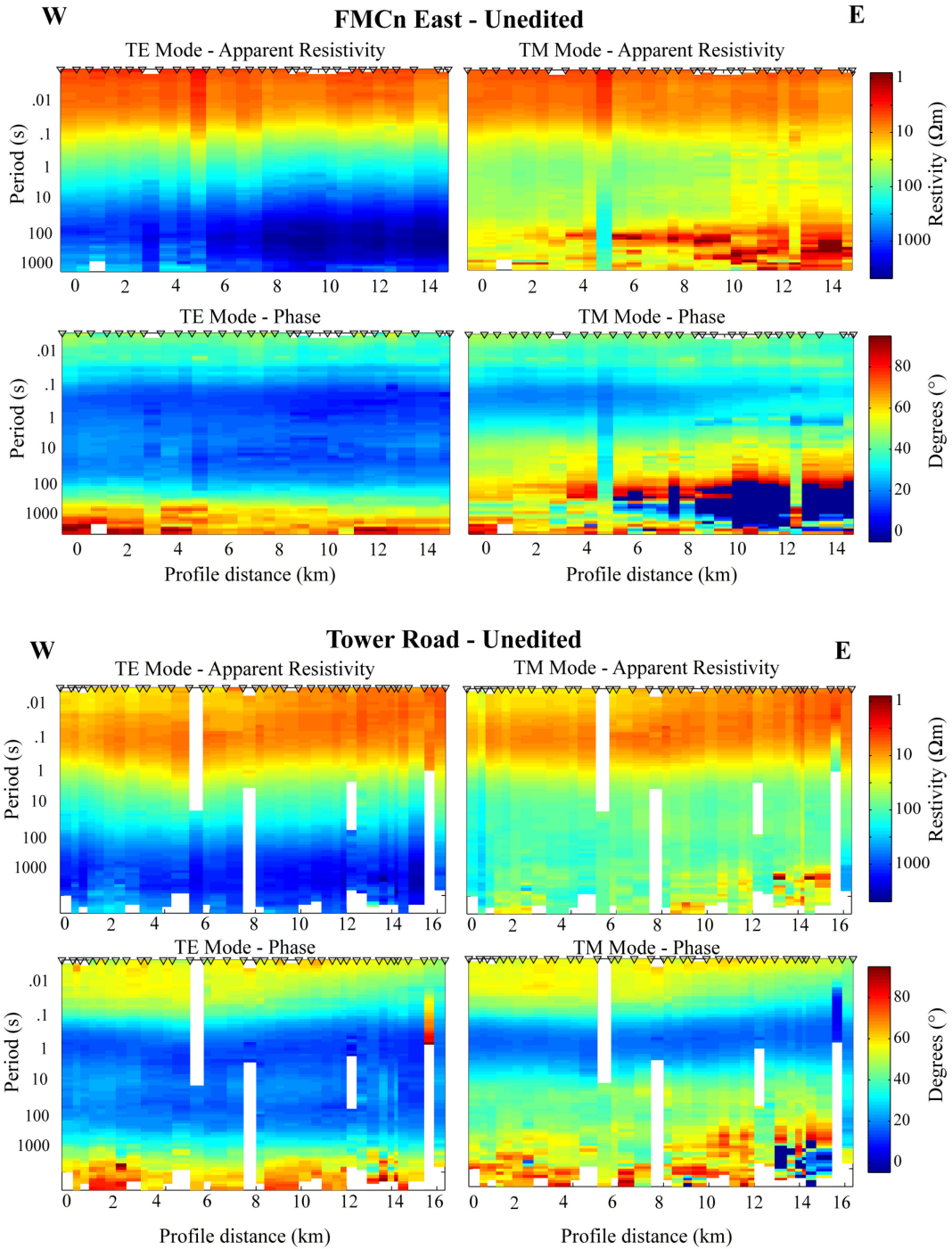
Figure 7.1: Resistivity and phase pseudosections, rotated to the Groom-Bailey defined geoelectric strike direction. Noisy data has been removed but all out of quadrant phase effects are maintained. Blue sections representing phases less than 0° phase occur when the phase exceeds 180° and is wrapped around. Anomalous region begins at ~100 s in the FMCn East profile and ~1000 s along Tower Road.

The stations that exhibit OOQ phase in Figure 7.1 do not do so every rotation angle, there is a rotation angle bandwidth at which OOQ phase is observed that is shared throughout the FMCn East and TR profiles. Figure 7.2 shows the TM mode phase for a representative station, FMCn 240, as a function of rotation angle. This can be compared with Figure 2.15 for the case of an outcropping anisotropic block discussed earlier. OOQ phase is observed at rotation angles between 25° and 60°, the maximum amount when rotated to the Groom-Bailey strike direction of 40°, found in Chapter 5.
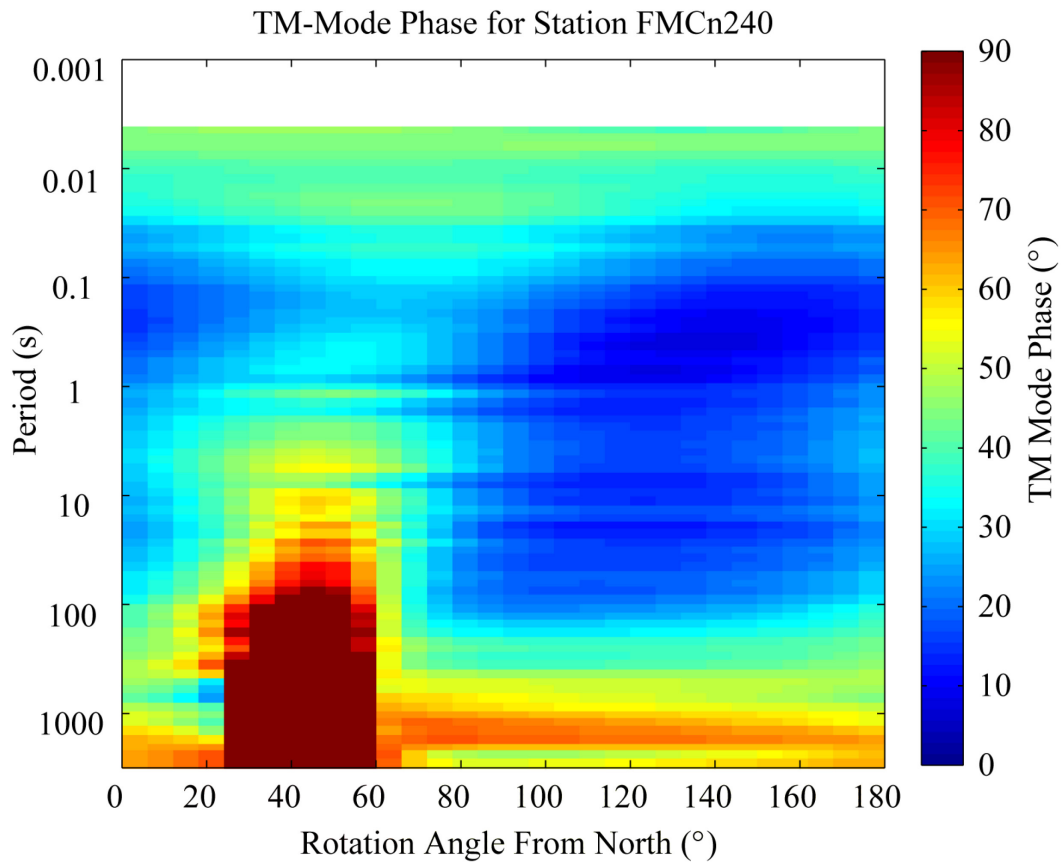
Figure 7.2: TM-mode phase for the station FMCn 240 presented for signal periods and rotation angles from 0-180° East of North. Bright red region shows the periods and rotation angles at which FMCn 240 exhibits out of quadrant phase.

Out of quadrant phase can be due to either 3-D or anisotropic 2-D resistivity structure, Figure 7.3 shows an MT sounding illustrating each of these effects for comparison with a typical MT sounding from this study. The 3-D example (Figure 7.3 middle) is from Jones et al., (1993) and was inferred to be due to surface charges on the highly resistive Nelson Batholith, note that it uses a different scale to plot phase and out of quadrant phase begins at -45°. The 2-D anisotropic example (Figure 7.3 left) is from the study by Heise & Pous (2003) that was described in Chapter 2.

All three studies associated with the curves in Figure 7.3 have a yx (TM) conductive mode, very small induction vector magnitudes in the affected region, and neighbouring stations that do not experience OOQ phase at all. There are several reasons why the 2-D anisotropic explanation is more appropriate for the FMC data:

1. The consistency of the resistivity and phase data between stations means that any 3-D conductor would have to be off-profile and the low magnitude induction vectors make off-profile conductors unlikely. The same qualities of the data are observed on the TR and the FMCn East profiles, which are physically separated by a larger distance (20 km) than the depth at which the OOQ phase begins (5 km).

2. Heise & Pous (2003) observed that the presence of the OOQ phase in their 2-D anisotropic model depended heavily upon the coordinate frame in which the data were displayed. The OOQ phase in the FMC data is also heavily coordinate frame dependant, as evidenced by Figure 7.2. At most rotation angles no OOQ phase is observed in either mode; if the effect were 3-D then OOQ phase would be observed at all rotation angles in either the TE or TM mode.
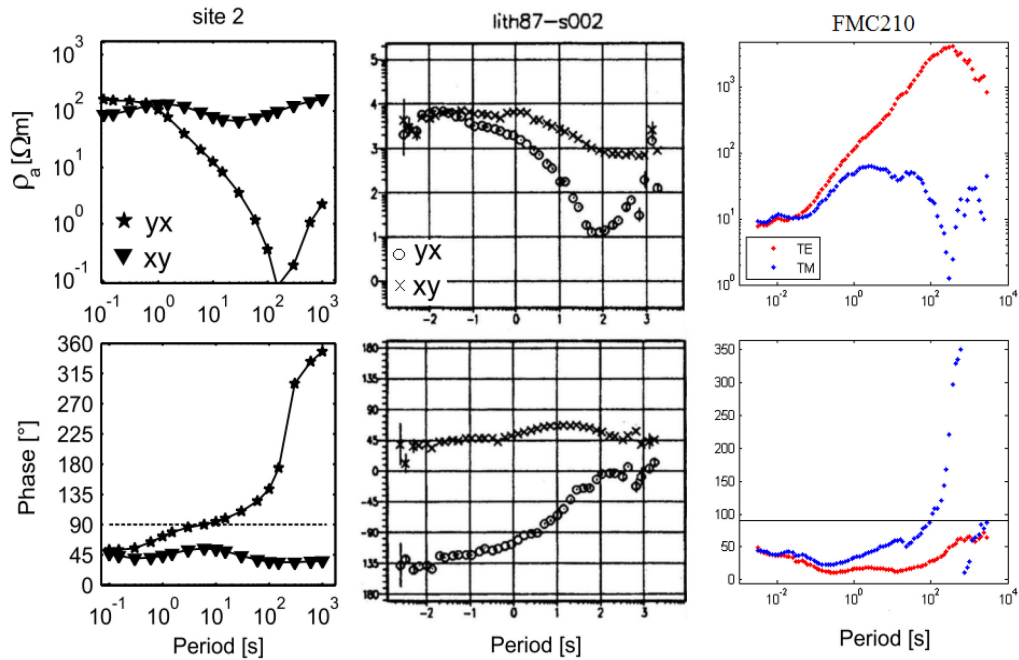
Figure 7.3: A comparison of OOQ phase observed at stations from Heise & Pous (2003), Jones et al., (1993), and this study. (Left) synthetic forward modelled station using 2-D interacting orthogonal, anisotropic blocks. (Middle) Data collected above the Nelson Batholith as part of the Lithoprobe study in 1987. (Right) Station FMC210 from the FMCn East profile in this study.

7.1.1   Implications for 2-D resistivity model

Anisotropy can produce OOQ phase because of the interaction of resistivity boundaries. The boundary may be between two regions with different anisotropies, as in the Heise & Pous (2003) study, or between anisotropic and isotropic regions, as in the example for a 'Pek-like' structure that was discussed in Chapter 2. Isotropic inversion of the period band 0.01 s - 1 s in Chapter 6 showed that the upper 5 km in the FMC region is isotropic and relatively 1-D. Therefore, the OOQ phase cannot be from a Pek-like nearly outcropping anisotropic block because that effect has disappeared by 3 km depth.

- The OOQ observed in the FMC MT data phase require two anisotropic regions with different orientations at depths no shallower than 5 km.

7.2 Phase Tensor Ellipses

The phase tensor pseudosections from the previous chapter are presented here again in Figure 7.4 and Figure 7.5. The red highlighted region indicates the zone of high skew and oriented phase tensor azimuths that dominate the FMCn East and TR profiles, and it is this region that will be the focus of this section. The TR high skew zone is similar but less pronounced in comparison to FMCn East and begins at a longer period; this is similar to the OOQ phase discussion in the previous section. The phase tensor ellipses from FMCn West do not have the same level of consistency in skew or azimuth between stations. The character of the phase tensor ellipses is clearly different for FMCn West than FMCn East.

The red region is characterized by extremely high skew values ($\beta > 10°$), consistent azimuths near N40°E, and a consistent level of phase split. There is a very sharp end to the high skew block near the center of the FMCn profile, where the FMCn East is divided from FMCn West. It is remarkable how the high skew zone terminates over a distance of less than 1 km. The high skew zone is coincident with the stations and periods that exhibit OOQ phase, as described in the previous section.

The phase split is observed over two decades (1 s - 100 s). The source of the split must be regional, since the same features are seen on data from both profiles, which are separated by a north-south distance of 20 km. It should be noted that phase ellipses have a high degree of ellipticity which implies that there is small error in the azimuth calculation (Caldwell et al., 2004). The direction of φ_{max} reflects the direction of maximum inductive current flow which means that the major axis of the ellipse will orient perpendicular to the highly conductive direction (Heise et al., 2006)
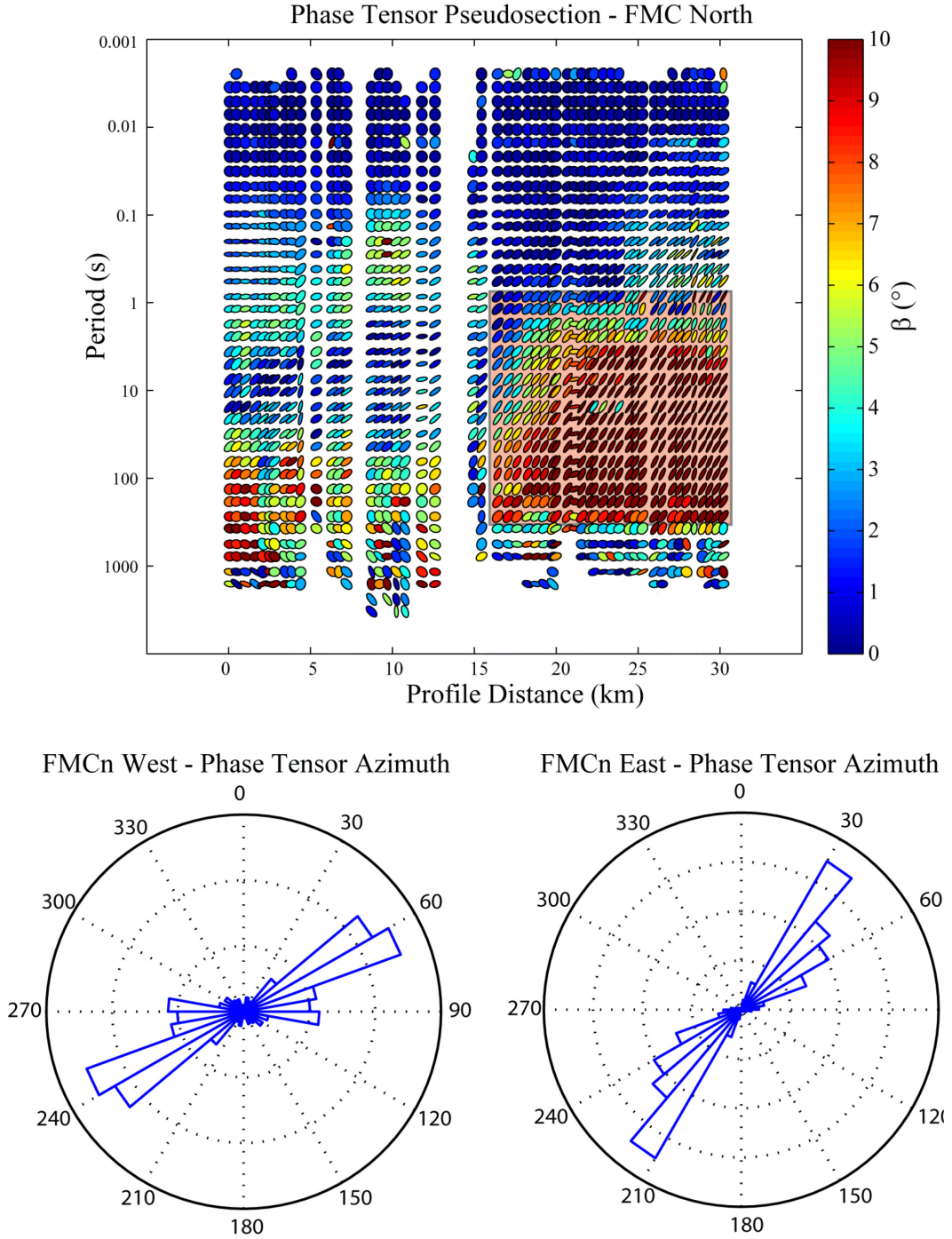
Figure 7.4: Phase tensor information for the full FMCn profile presented as a pseudo section (above) and the orientation of the major axis of the phase tensor ellipses presented as a Rose diagram (below). The azimuth can be unstable unless φ_{max} and φ_{min} differ substantially, here the minimum phase split is set to 5° to ensure the diagram portrays the true nature of the azimuths. The red region indicates the zone of high skew and oriented phase tensor azimuths.
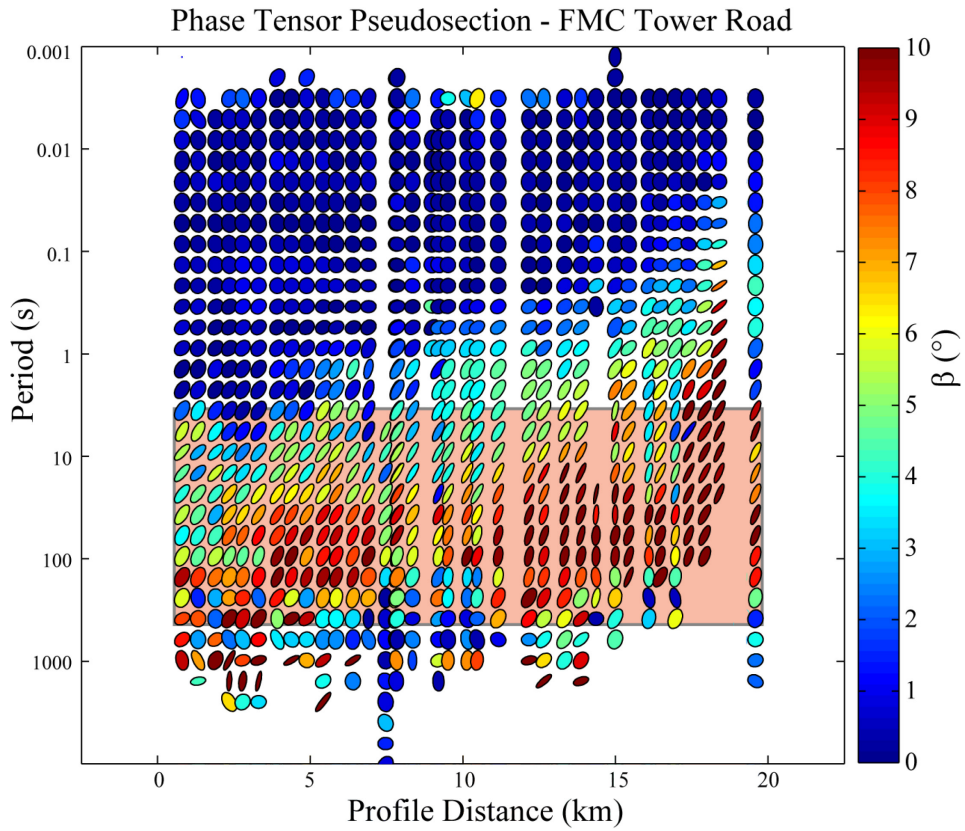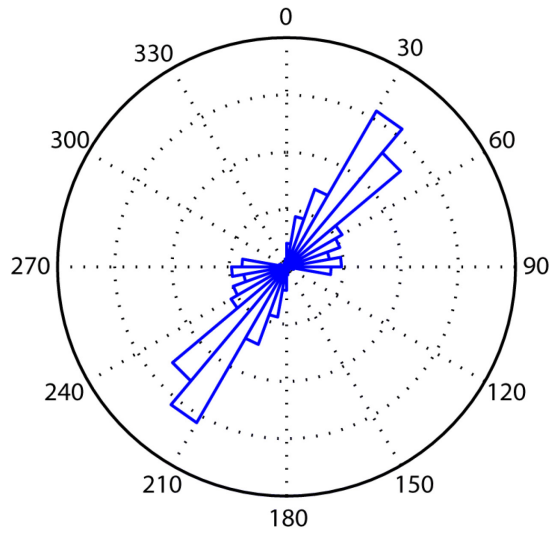
Figure 7.5: Phase tensor information for the Tower Road profile presented as a pseudo section (above) and the orientation of the major axis of the phase tensor ellipses presented as a Rose diagram (below). The azimuth can be unstable unless φ_{max} and φ_{min} differ substantially, here the minimum phase split is set to 5° to ensure the diagram portrays the true nature of the azimuths. The orange region indicates the zone of high skew and oriented phase tensor azimuths.

The calculation of the geoelectric strike in Chapter 5 was the main reason for dividing FMCn East and TR from FMCn West. Calculation of the GB strike direction involves minimizing the diagonal components on the impedance tensor (see explanation of Groom-Bailey strike in Chapter 2). This means that changes in the diagonal components Z_{xx} and Z_{yy} can cause changes in the calculated strike direction. The diagonal impedance tensor components correspond to the anti-diagonal phase tensor components, φ_{xy} and φ_{yx}, which are used to calculate the value of the skew β. Therefore the source of the high skew in the red regions of Figure 7.4 and Figure 7.5 is the reason that the strike direction was found to be different in the East than in the West.

7.2.1 Phase tensor implications for 2-D resistivity model

The high skew values are usually indicative of 3-D resistivity structure, however, as shown in Chapter 2, 2-D anisotropy is capable of creating high skew phase values if there are lateral resistivity structure boundaries (see Model-6, anisotropic prism in Figure 2.11).

The phase split of the ellipses is the same for all FMCn East and TR stations; this means that there must be a vertical boundary between the resistivity structures. The consistency of the azimuth of the phase ellipses means that the basement must extend deep enough to appear nearly as a halfspace. Recall from Chapter 2 that phase tensor ellipses will change orientation by 90° on either side of a conductive-resistive interface. Model-2 with an anisotropic basement is an example of phase tensors that do not experience the 90° flip, because the skin depth does not penetrate the bottom of the layer.

The implications of the phase tensor upon the 2-D resistivity model are:

- Lateral boundaries do not appear in the resistivity and phase pseudosections, so they must be between differing anisotropies.

- The basement beneath 5 km must extend deep enough to make the phase tensors maintain their azimuth from at least a period of 1 s - 100 s.

7.3   Phase Split and Induction Vectors

In Chapter 5, pseudosections of the phase split and the induction vectors for the FMCn and TR profiles were presented. Analysis of phase effects in the previous sections give no control over the actual resistivity values, they only have implications for resistivity contrasts. The shortened bandwidth inversions from Chapter 6 define the resistivity values in the upper 5 km. When rotated to the GB strike direction the TE mode apparent resistivity reaches more than 1000 Ωm, while the TM mode stays between 50 Ωm and 100 Ωm, this is true for all stations in the FMC region.

The induction vector pseudosections in Chapter 5 showed that there were no large magnitude induction vectors or clear reversals of induction vector direction in the regions not affected by pipeline noise. For stations in the high skew zone the IVs were still of small magnitude.

Heise & Pous (2001) noted that the direction of inductions arrows can be greatly affected by anisotropic structures, but inconsistently such that no evaluation of either anisotropic or regional 2-D strike direction is possible based on induction vectors. The phase splits must owe their existence largely to vertical changes in resistivity rather than a lateral ones (Caldwell et al., 2004).

7.3.1   Resistivity and IV implications for 2-D resistivity model

The resistivities used in the anisotropic regions must not create TE and TM mode resistivities that do not match those observed in the FMC data.

- The forward model response must match, with reasonable r.m.s. misfit, the measured FMC data.

- The forward modelled induction vectors must have small magnitudes at the same periods and stations that the measured data has small magnitudes. There is no control in the regions that were removed due to the pipeline noise.

7.4   Comparison of Distortion Effects Between Profiles

The resistivity, phase and phase tensor parameters for a typical site from each of the three profiles are presented in Figure 7.6. The uppermost panel of Figure 7.6 shows the apparent resistivity values of the yx and xy mode after rotation to Groom-Bailey strike direction. The xx and yy apparent resistivities are not plotted, but are represented in the other panels via the phase tensor skew and azimuth.

The second panel shows the azimuth of the phase tensor major axis as a function of period. The dotted line gives the direction of the theoretical, undistorted, azimuth that would be observed if $\beta = 0$; recall from Chapter 2 that azimuth is the value of α- β. The azimuth is the direction of maximum inductive current flow.

The third panel shows the observed yx and xy impedance phase in red and blue, plotted with the value of the phase tensor φ_{max} and φ_{min} as dotted lines. The dotted and coloured lines will have the same value in the case that the data is 1-D or 2-D isotropic (Caldwell et al., 2004).

The fourth panel shows the phase tensor skew, β, as a function of period. The skew plot is useful for seeing exactly what features in the data are correlated with the increase of distortion.

The final panel plots the induction vector magnitude perpendicular to the GB strike direction (y-component of IV). This is the component that would react to conductors perpendicular to the profile.
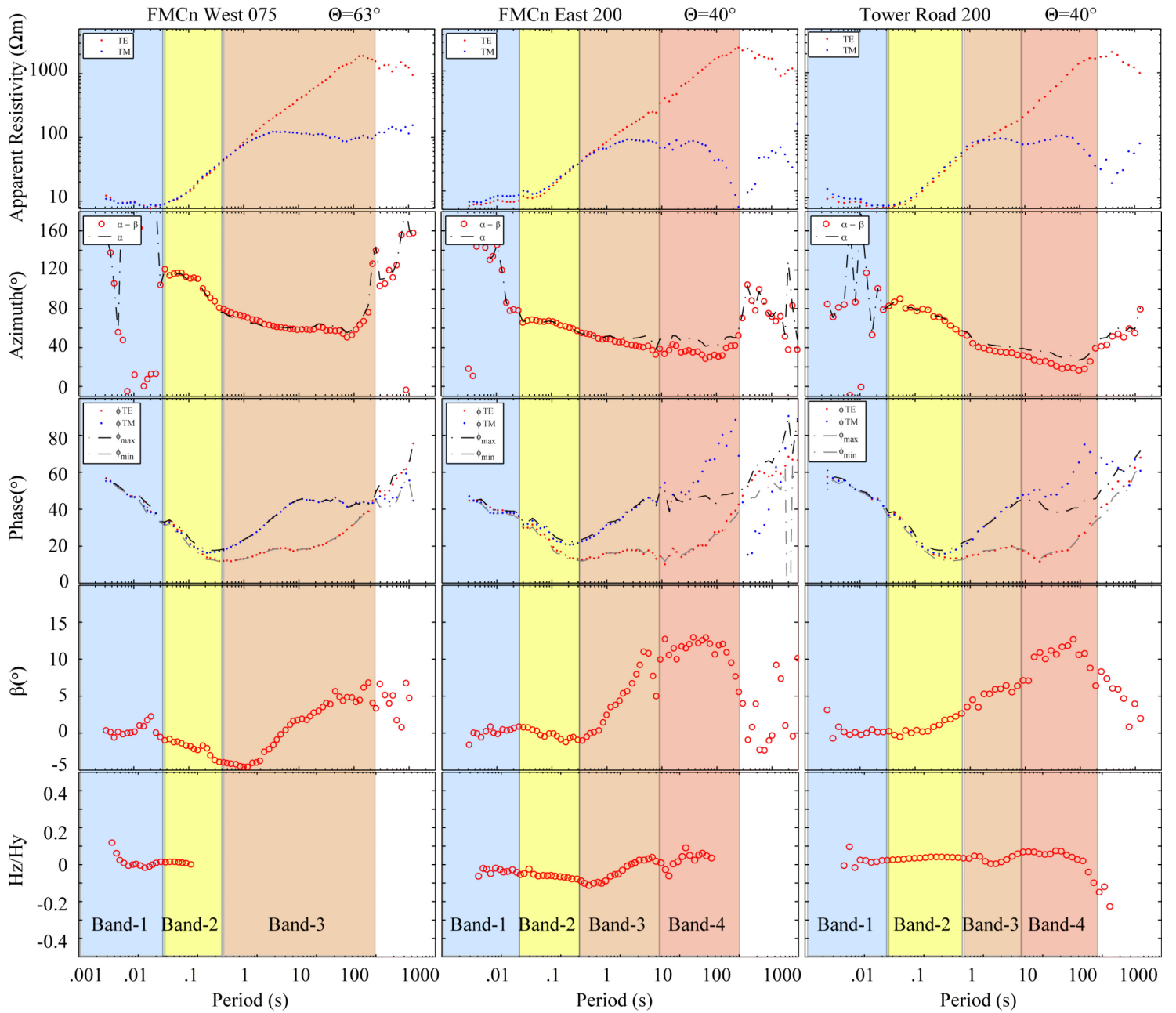
Figure 7.6: Phase tensor and distortional parameters from three stations typifying each of the three identified regions. (Left) FMCn West (Middle) FMCn East (Right) Tower Road. Upper panel is the TE/TM apparent resistivity post rotation to azimuthal coordinates. Second panel shows the ideal phase tensor azimuth as a function of period (red) and the distorted result due to skew (dashed line). Panel three plots the values of φ_{max} and φ_{min} against the natural TE/TM phase. Panel four shows the change in phase tensor skew β as a function of period. Panel 5 is the y-component tipper magnitude.

7.4.1　Band 1 (blue)

The blue region is characterized by ~10 Ωm resistivity, no phase split, no clear phase tensor azimuth, and low skew values. Varying azimuths are indicative of 1-D structure. Similar results were found for the GB strike direction for the periods 0.01 s - 0.1 s in Chapter 5. This band can be identified with the low resistivity rocks of the WCSB.

7.4.2　Band 2 (Yellow)

Data from the yellow band is clearly sampling the much more resistive rocks, but continues to exhibit low 2-D distortion, and phase split is minimal. Apparent resistivity rises sharply in this band, implying true resistivity values upwards of 1000 Ωm. This band can be identified with the electrically isotropic rocks of the crystalline Precambrian basement. Data up to the end of the yellow band were inverted successfully with the reduced bandwidth inversions in Chapter 6.

7.4.3　Band 3 (Orange)

The orange band encompasses the beginning of the phase split until either the impedance phase departs from the φ_{max} and φ_{min} values, or the phase split ends. The phase tensor azimuth varies smoothly in this band; there is clearly a fabric, a preferred orientation, to the Earth's resistivity structure in this and the subsequent red band.

The plot of β in the fourth panel shows reasonably low values until the phases split. All three stations have an increase in skew through the orange band. The skew increases in the FMCn West station as well, even though it never has OOQ phase. This means that the source of the phase split and the source of the OOQ phase are not the same.

7.4.4   Band 4 (Red)

The red period band begins when the phase starts to leave the quadrant and has the highest skew values, despite a very consistent phase tensor azimuth. Note that the red region does not appear in the FMCn West site (Left image in Figure 7.6). The impedance phase curve departs from the principal values of Φ when it begins to leave the quadrant. This is the result of non 2-D isotropic distortion (Caldwell et al., 2004). The previous section showed that the OOQ phase must be from the interaction of two anisotropic regions at 5 km depth. Only the TM mode is affected by the OOQ phase, and the TE mode remains smooth and never departs from the dotted phase tensor curve. This is evidence for a 2-D anisotropic solution, because if the source of the OOQ phase were extreme noise there would not be one smooth mode.

The variation of azimuth in the second panel is very smooth with period, even when the skew values in panel four reach very large values. A wildly changing azimuth would be evidence of 3-D structure or noise. The end of the smooth azimuth region coincides with the point that the phase finally leaves the quadrant.

The skew stops rising in band-4 (red), it plateaus between ~10°-15°. These skew values are much higher than the FMCn West station, which does not have a red band region. It must be that the source of the OOQ phase is also the source of the >10° skew values. As soon as the phase actually leaves the quadrant the skew value falls dramatically, back to acceptably 1-D or 2-D values.

7.4.5   Implications for 2-D resistivity model

Comparisons between representative stations from the FMCn West, FMCn East and TR profiles have shown that there are at least two separate distortional effects present in the

data: the source of the phase split, and the source of the OOQ phase. It was shown previously that there are at least two anisotropies interacting at depths greater than 5 km.

- The source of the phase split (orange band) exists at all stations in the FMC region
- The source of the OOQ phase (red band) only affects the FMCn East and TR stations, and is likely due to there being an interactions between two anisotropies in those profiles.

7.5   Anisotropic Forward Modeling

The goal of this section is to present the anisotropic 2-D resistivity model that best explains the features observed in the MT data described in the previous sections of this chapter. Anisotropic interpretations that do not use all four impedance tensor elements, and the induction vectors, may be inappropriate and can often result in terms of off profile 3-D conductors (Weckmann, 2006). The method used in this section is a 2-D forward modeling code from Pek & Verner (1997) which calculates all four elements of the impedance tensor. Cells in the inversion model mesh have up to 3 resistivities, one for each direction, as well as an anisotropic strike, dip, and slant. The anisotropic strike is a rotation about the z-axis and is therefore relative to the 2-D strike (which is always 0°, into the page); the anisotropic dip is measured relative to the new x-axis, after the strike rotation.

Only the forward model for the FMCn profile is presented here. The Tower Road data was shown to be similar to the FMCn East data so if the model explains FMCn East, then it implicitly explains Tower Road as well. The previous section explained the qualities the 2-D anisotropic model must have in order to adequately explain the data. A representation of the final model that succeeds in this is presented in Figure 7.7.
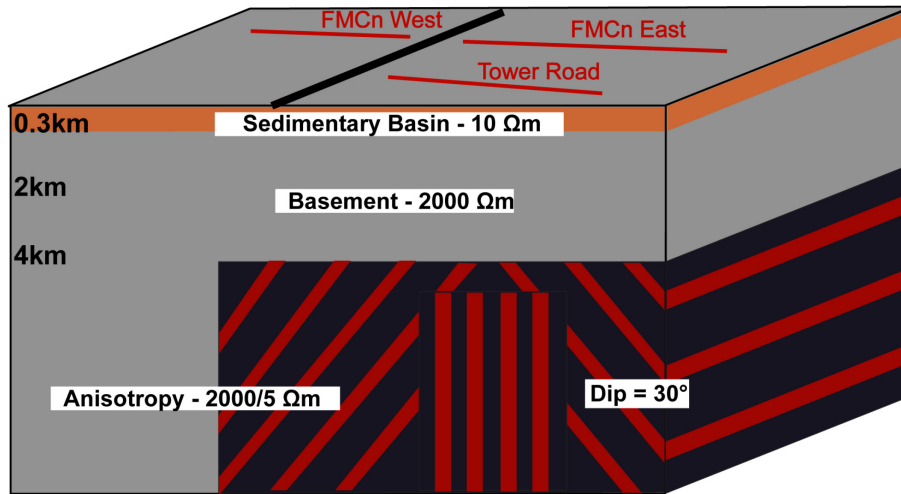
Figure 7.7: Block image of the final anisotropic forward model that best represents all the features of the data. MT profiles are shows in red on the surface, the Hunt well in yellow. Red indicates orientation of the of anisotropy. All anisotropic regions have an anisotropic strike of N63°E. There is dip lineated anisotropy on either side of the central, strike-lineated, anisotropic block. Dip is set to 40° from vertical on both sides.

The simplest model possible was sought, i.e. the one which can explain the most aspects of the measured MT data with the least number of model features. Hundreds of models were tried in order to set the parameters on the resistivity and orientation of the various anisotropic regions. The description of the final resistivity model is as follows:

- 0 km- 0.3 km. Low resistivity, (10 Ωm) isotropic surface layer of clastic sedimentary rocks of the WCSB. The thickness of the surface layer is set to 300 m to approximate the depth to the more resistive carbonate and evaporate sequences, which extend another 240 m as measured with logs from the Hunt Well from Chan (2013).

- 0.3 km - 5 km. High resistivity (3000 Ωm) layer of, isotropic, granitoid rocks from the Precambrian basement (Walsh, 2013). The depth to the base of this

layer can be approximately constrained to be 4 km using the skin depth equation (Chapter 2) and shortened bandwidth inversions in Chapter 6.

- Anisotropy begins at a depth of 5 km with resistivity ratio of 2000/5 Ωm. Stripes indicate the orientation of the anisotropy. The red stripes indicate the orientation of the anisotropy. An anisotropic block lies beneath the TR and FMCn East profiles and is flanked by anisotropic regions dipping away from the center at 40°. The anisotropic strike was set to N63°E for all anisotropic regions; the 2-D strike is 0°. This type of structure was found to be necessary to create the skew and OOQ phase simultaneously.

- R.M.S. misfit between the response of the forward model and the measured MT data is 2.7. This value was calculated from all four impedance tensor elements.

7.5.1   2-D resistivity model data fit

The qualities of the data described above are compared in this section to the data from the forward model in Figure 7.7. The left column is the measured MT data and the right column is the corresponding forward model result.
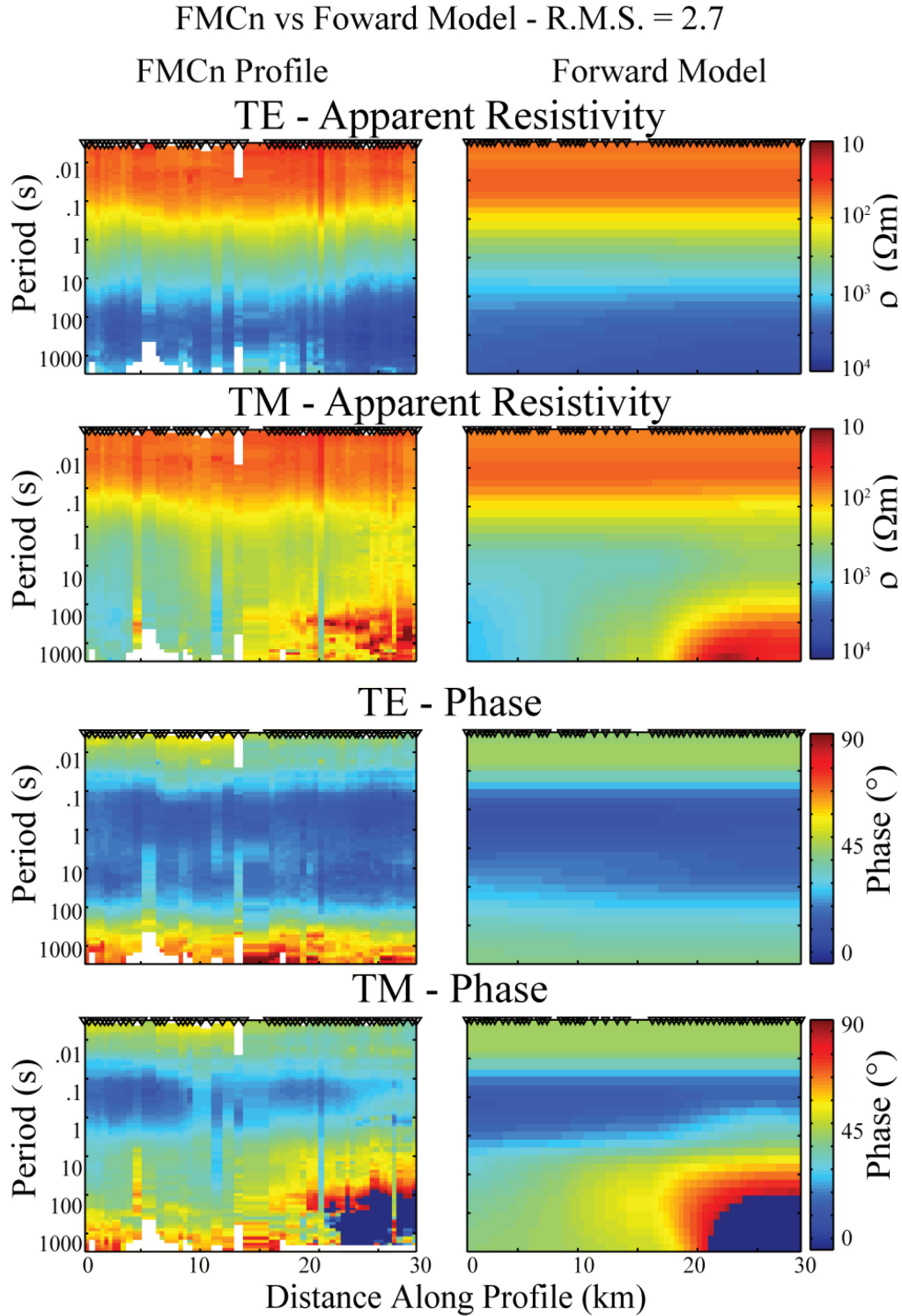
Figure 7.8: Apparent resistivity and phase comparisons between the measured data and the forward modelled data on the FMCn Profile. Data were rotated to N40°E in order to show the OOQ phase regions. R.M.S. misfit value was calculated from all four impedance tensor elements.

The forward model apparent resistivity and phase are shown in Figure 7.8. The model shows good agreement with the measured data for both the TE and TM modes. The OOQ phase extends approximately 20 km inward from the Eastern edge of the profile in both TM-phase pseudosections. Resistivity and phase values are comparable, as evidenced by the reasonably low r.m.s. misfit of 3.02. For periods longer than 500 s, the TE-mode in the model does not match the data well. At these periods, the shallow structure defined by the forward model is no longer applicable, and the data is likely 3-D; this is discussed in Chapter 5.
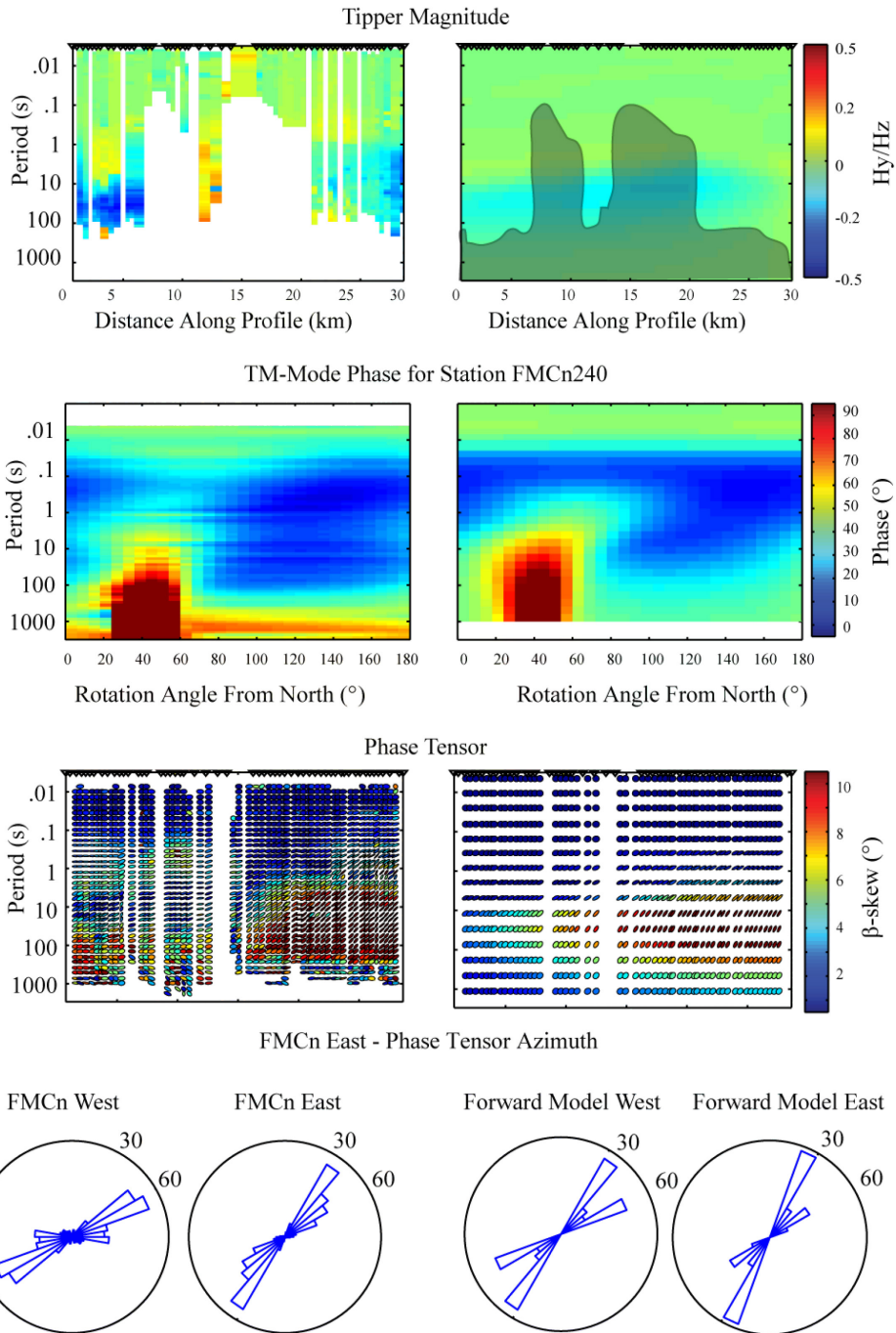
Figure 7.9: Tipper magnitude, OOQ phase rotation angle plot, and phase tensor parameters for the measured data and the forward modelled data on the FMCn Profile. Gray region on tipper magnitude plot indicates regions masked in the measured data. Rose diagrams indicating phase tensor azimuth are split into East and West to match the FMCn West/East split.

The tipper magnitude predicted by the forward model in Figure 7.9 is very low at all stations. There is a small increase in the East that is in agreement with the measured MT data, but it is much lower that the measured MT data in the West. Gray regions indicate the areas that were masked from the measured tipper data. The disagreement visible in the Western part of the profile indicates either that there is some resistivity structure unaccounted for in this model or that the pipeline noise was not fully removed from the tipper data.

The OOQ phase characteristics are compared using the same station as that shown in Figure 7.2, FMCn 240, and the corresponding forward modeled station in Figure 7.9. The OOQ phase rotation bandwidth matches quite well, being centered at N40°E, and the phase leaves the quadrant at the correct period (between 10 s and 50 s).

The forward modeled phase tensor ellipses have >10° skew values at the correct locations and begin at the period observed in the measured impedance data (~1 s). The high skew values disappear at periods greater than 500 s, which also matches the measured data. The model fails, however, to recreate the abrupt termination of the high skew block in the center of the profile, instead extending high skew values into the FMCn West region.

Similar to the phase tensor skews, the azimuth values in the forward model match those of the data only in the region corresponding to the FMCn East profile. The rose diagrams at the bottom of Figure 7.9 show the phase tensor azimuths, which are split into West and East in accordance with the FMCn West/East split. The Eastern rose diagram largely agrees with the measured data, and is aligned between N30°E and N40°E. The Western rose diagram has some agreement with the measured N60°E, but also displays significant influence from the Eastern N40°E azimuth.

A comparison of the FMCn East sounding in Figure 7.6 to the forward model sounding at the same location is presented in Figure 7.10. This underscores the agreement between the forward model and the measured data in the FMCn East profile. Agreement is very strong in all parameters presented in Figure 7.10 up to ~500 s, when the measured data cease to be 2-D.
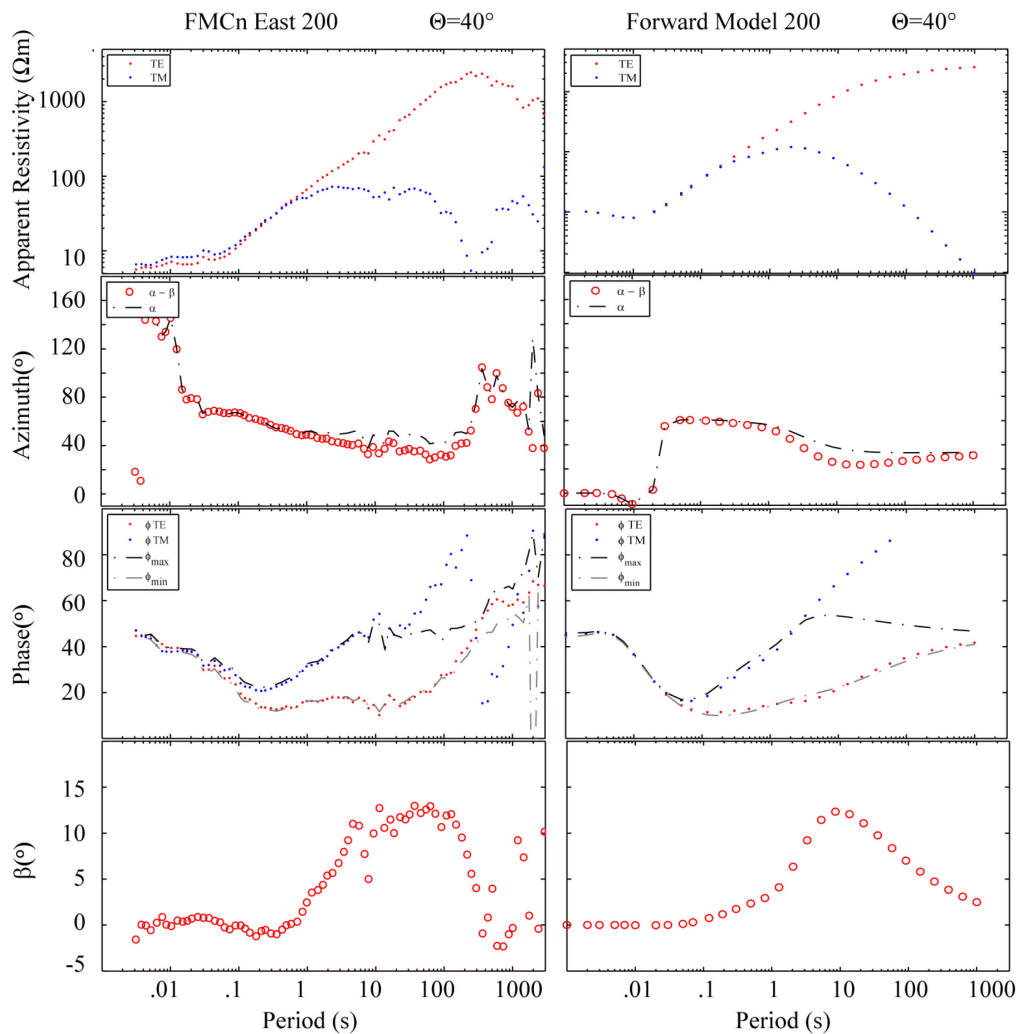
Figure 7.10: Sounding comparison between station FMCn East 200 (Left) and the forward model sounding at the same position (Right). Upper panel is the TE/TM apparent resistivity post rotation to azimuthal coordinates. Second panel shows the ideal phase tensor azimuth as a function of period (red) and the distorted result due to skew (dashed line). Panel three plots the values of φ_{max} and φ_{min} against the natural TE/TM phase. Panel four shows the change in phase tensor skew β as a function of period.

These comparisons show that the anisotropic resistivity model shown in Figure 7.7 can fit the observed MT data in the FMC region. The computed response fit the measured MT data with a low r.m.s. misfit, and give a good visual fit to the measured data in the key areas mentioned above, especially for the FMCn East (and by extension the southern TR) profile. Differences in the phase tensor azimuths and the tipper magnitudes on the FMCn West profile show that the model in Figure 7.7 can only partially account for the FMCn West data.

7.6   Summary

The 2-D anisotropic forward modelling technique used to create this model is non-unique, i.e., there are many resistivity models capable of fitting the measured data with the same r.m.s. misfit. Structural implications of the pattern of OOQ phase, phase tensor ellipses, induction vectors, and resistivity mode split were used to guide the development of the 2-D anisotropic resistivity model. By combining these implications a model was found that not only fits with a low r.m.s. misfit, but also matches the characteristics of the data. Possibilities for the geology and implications of this model for geothermal development will be explored in the next chapter.

Chapter 8

Discussion and Interpretation

The FMC magnetotelluric data have been processed and were found require an anisotropic resistivity structure beginning at a depth between 4 and 5 km. The relatively small station spacing and large number of stations collected in the FMC region during this project allows the anisotropy to be characterized in more detail than in many other previous MT surveys. As a part of Theme 4 of the Helmholtz-Alberta Initiative, this work provides information about the properties of the deep basement rocks that is needed to effectively develop engineered geothermal systems in Northern Alberta.

An anisotropic resistivity model was developed that was able to explain the complicated MT data from the FMC region. MT data from the Western part of the profile were not fit as well as data from the Eastern region. The FMCn East and Tower Road profiles were shown to be very similar, so it is likely that the same resistivity structure lies beneath them both, and by inference also between them. Hundreds of anisotropic resistivity models were investigated in order to find a model that gave an acceptable fit to the measured MT data. The final model contained a central anisotropic block with strike lineated anisotropy flanked by two regions of dip lineated anisotropy. The bulk resistivities of the anisotropic region were constrained by the data to be 2000 Ωm and 5 Ωm in orthogonal directions. The strike of the anisotropy was determined to be N63°E in order to match the phase tensor azimuths. The interaction between the dipping anisotropy and the non-dipping anisotropy was able to reproduce the N40°E azimuth observed in the FMCn East and TR profiles.

Chapter 8 – Discussion and Interpretation

8.1   Related Studies in the FMC Region

8.1.1   Seismic studies

Characterization of the seismic velocity structure of the basement rocks beneath the study area is described by Chan (2013). In this study, an existing deep seismic reflection profile, with resolution to a depth of 35 km, was combined with a new borehole seismic data in the Hunt Well and a high-resolution reflection profile along Tower Road that was designed to characterize the upper 1200 m of the Precambrian basement. Vertical seismic profiling revealed elastic anisotropy values of 12 - 15% from the surface to a depth of 797 m, and 16 - 18% in the depth range 797 m to 1777 m. The anisotropy increased in strength with depth, and was attributed to aligned fractures and the presence of a potential mafic dike between 797 m and 1777 m (Chan, 2013).

Eastward-dipping reflectors were identified in the seismic reflection profile from depths of 2 km to more than 20 km. The reflectors were interpreted as naturally occurring fractures that could be of interest to EGS development as a source of natural permeability. This seismic profile is coincident with the magnetotelluric Tower Road profile. The 2-D seismic and the magnetotelluric data are compared in Figure 8.1. The pink boxes show shallow and deep examples of the eastward-dipping seismic reflectors. The shortened bandwidth inversion of the electrically isotropic MT data from Figure 6.9 is compared to the seismic reflection data in Figure 8.1b. The final forward resistivity model from Figure 7.7 is compared to the seismic reflection data in Figure 8.1c.
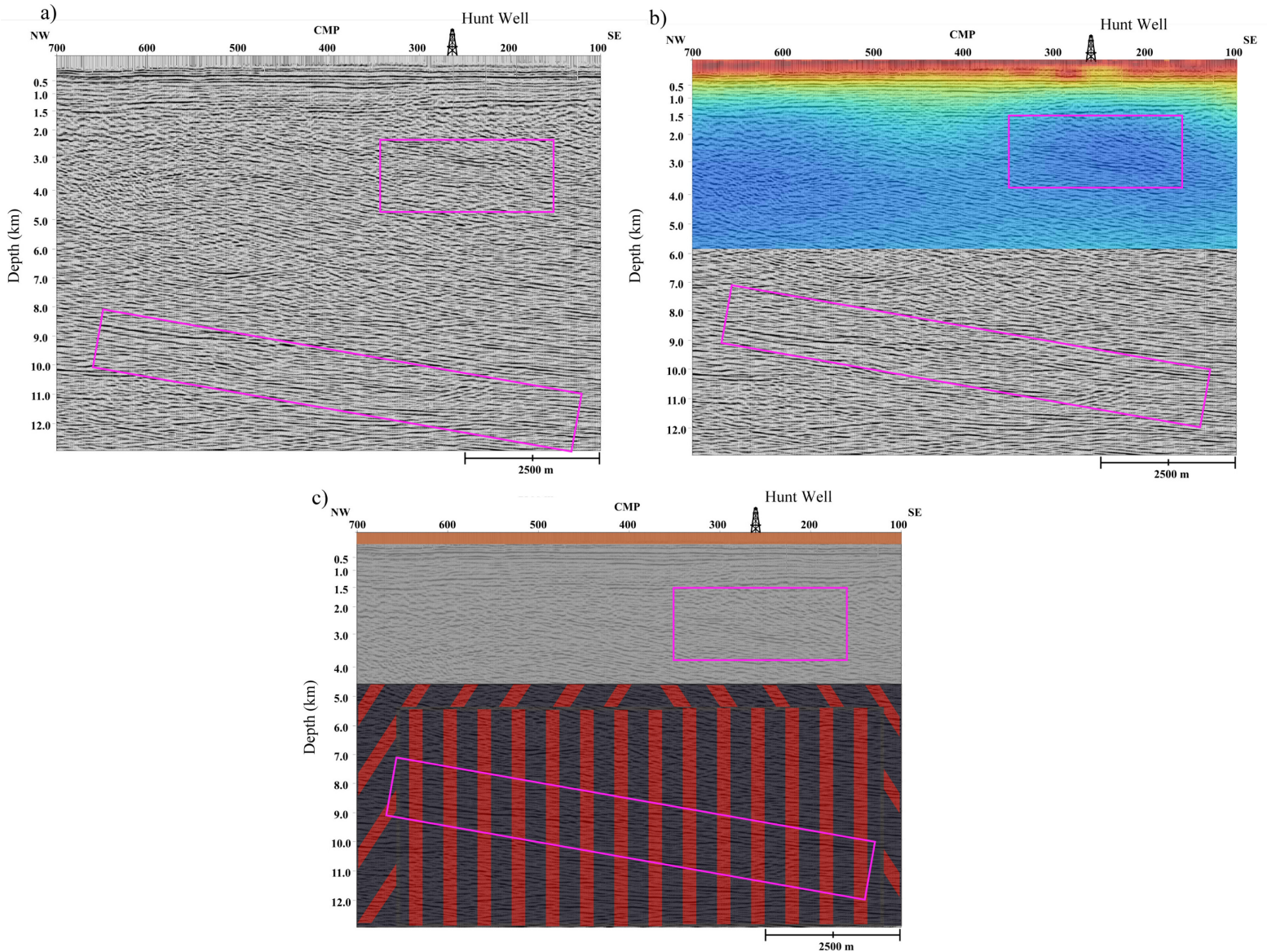
Figure 8.1: Seismic section coincident with the Tower Road MT profile. Location of the Hunt Well is indicated. Coloured boxes indicate the location of potential dipping reflectors, both shallow and deep, from (Chan, 2013). (b) comparison of seismic section with Tower Road shortened bandwidth inversion of the upper 4-5 km compared to seismic section. (c) Comparison of seismic section with forward model from Figure 7.7.

When comparing images of the subsurface derived from seismic and magnetotelluric data, it is important to understand the different manner in which each geophysical method images the subsurface. Seismic exploration uses signals that travel through the subsurface as elastic waves, and are sensitive to changes in acoustic velocity. The limit in vertical

151

resolution in seismic reflection data is one quarter of the dominant wavelength of the signal; this is called the Rayleigh criterion. It defines the minimum thickness of a layer that can be resolved with seismic reflection data. The Earth filters out short wavelength (higher frequency) seismic signals so that the minimum resolvable thickness increases with depth. Reflection data were recorded using signals from 10 to 160 Hz, and sonic and density well logs revealed an increase in velocity with depth from 4700 m/s to 7000 m/s (Chan, 2013). These values correspond to an approximate vertical resolution of ~10 m near the surface and ~200 m below a depth of 2.3 km.

MT exploration uses diffusive electromagnetic signals and measures resistivity structure over a volume that is defined by the skin depth, as discussed in Chapter 2. MT is thus more suited to imaging larger scale structures and determining the bulk properties, compared to seismic reflection. The seismic reflection data image the sub-horizontal layering of the WCSB at travel times of 100 -350 s. These layers occur at the same depths as the low resistivity values that characterize the same layer. Individual layers cannot be resolved with the MT but they have similar enough resistivity that they appear uniformly at 10 Ωm in the TR inversion.

The eastward-dipping reflectors in Figure 8.1 clearly have sufficient acoustic impedance contrast to give detectable seismic reflections. However, they don't have a sufficiently strong resistivity contrast to be imaged by the MT data. While the rocks were shown to be elastically anisotropic, their resistivity must not change appreciably. The deeper reflectors are likely below the spatial resolution level of MT at those depths, since the EM signals' skin depth would be over 5 km. Forward modelling of eastward-dipping conductors based on the geometry of the seismic reflectors did not reproduce the observed MT data.

It is possible that the resistivity structure of the eastward-dipping reflectors is more complicated than the velocity structure. Acoustic anisotropy is present in the Precambrian basement rocks starting near to the surface, and possibly at depth as well. The acoustic anisotropy could not be coincident with electrical anisotropy until a depth of 4 - 5 km, as shown in Chapter 7. If the two observations of anisotropy are caused by the same physical mechanism, then one can hypothesize that anisotropy is a feature characterizing much of the FMC Precambrian basement.

8.1.2   Geology and Geochemistry

Geological mapping of the study area were based on the detailed analysis of drill core samples described by Walsh (2013). Of these, 33 came from the Taltson Magmatic Zone, two from the Buffalo Head terrane and one from the Rimbey domain close to Fort McMurray. Comprehensive U-Pb dating and analysis of the radiogenic heat production (RHP) values of the samples was carried out (Walsh, 2013). Radiogenic heat production is dependent upon the concentration of uranium, thorium and potassium in the sample. It was found that the younger TMZ core samples had generally higher concentrations of uranium, thorium and potassium, and thus higher RHP values. Drill core analysis is highly detailed, but only samples a small amount of rock that is recovered near to the top of the Precambrian basement. MT is capable of imaging the resistivity structure at depths in the range 4 - 7 km, which have been suggested to be necessary for EGS development as determined by the geothermal gradient extrapolations.

The basement rocks from the Hunt Well were shown by Walsh (2013) to be hercynite gneiss overlying orthopyroxene, neither of which contained magnetite as an accessory mineral. This is consistent with the low aeromagnetic field values observed in this region in Chapter 3 and Figure 8.2. The age of the samples was mapped and a location near to

Fort McKay was suggested to be the most suitable location for EGS development based on geothermal gradient and practical heat transportation concerns (Walsh, 2013).

8.1.3   Gravity and aeromagnetic data

Potential field data can be used to link the MT results to regional scale geological structures (Boerner et al., 2000). A map of the Bouguer anomaly (GB) and the aeromagnetic residual field in the study area was presented in Figure 8.2. The Bouguer anomaly measures changes in the density of the crust, and has topographic effects removed. A contour map of the Bouguer anomaly in the FMC region is shown in Figure **8.2** (left). The maximum change in Bouguer anomaly between any two MT stations is 7 mGal, there is a general trend in the gravity data, increasing from West to East on the FMCn profile, but decreasing from West to East on the Tower Road profile. Rock density and resistivity are not usually correlated, and there is not expected to be a major change in density over a region this size without any topographic features. The lack of correlation between the gravity data and MT data in the FMC region is not surprising, but at least shows that there is no major mass deficit or excess that could be causing the MT observations.
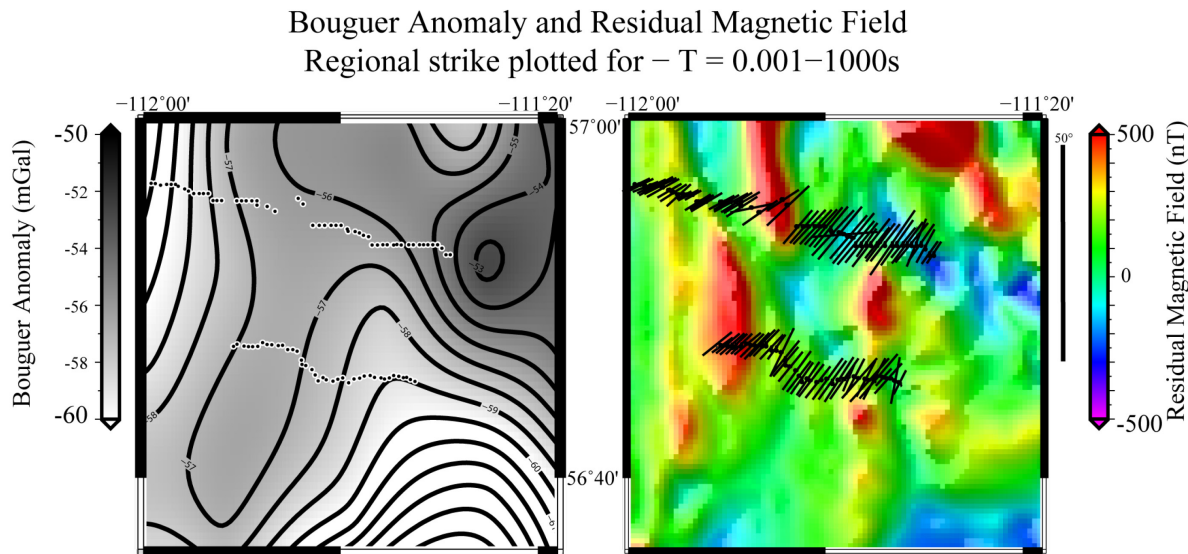
Figure 8.2: Bouguer anomaly contour map for the FMC region (Left). Residual magnetic field data for the FMC region combined with regional strike direction for each site (Right). Gravity and magnetic data downloaded from Natural Resources Canada.

The total residual magnetic field data in the study area are presented in Figure 8.2 (right). Along the Northern FMCn profile there is a possible correlation between the change in strike direction and the aeromagnetic high that intersects the FMCn profile. This could explain why the FMCn West data is so dissimilar to the FMCn East and TR data. The western-most sites on the TR profile also have a slight increase in the strike direction. The magnetic data do seem to be related to the MT data, the magnetic lows correspond generally to the FMCn East and TR profiles, and the magnetic high seems to separate FMCn East from FMCn West. This is not to say that the susceptibility of the rocks is affecting their resistivity, but there is a visual correlation that could be because the process that caused the change in susceptibility also altered the resistivity so as to produce the MT response analyzed in chapter 5. This process must also have only been active below 4 - 5 km depth, since the analysis in chapter 6 showed that FMCn East and West are nearly identical above that. These are clues that can be used to constraint, the process behind the MT anisotropy in the interpretation.

155

8.2   Integrated Interpretation

The seismic and geological results in the previous section, as well as the aeromagnetic data, can help to guide the interpretation of the MT data. The resistivity model developed in Chapter 7 included a high degree of electrical anisotropy. In this section, an explanation is sought for the anisotropy, and it will be seen that this can be a non-unique task. Using multiple techniques allows the origin of the anisotropy to be better understood rather than just using a single type of geophysical data.

MT data have been used in combination with other types of geophysical data in previous studies of anisotropy. For example, two separate seismic anisotropic directions were interpreted by Eaton (2004), for the Great Slave Lake shear zone using shear wave splitting. The fast direction was N30°E for the crustal structure and N60°E for the upper mantle. Yin et al., (2014) were able to detect electrical anisotropy in the GSLsz using MT data on three separate profiles extending from the Northwest Territories into Northwest Alberta. The GSLsz itself appeared as a resistive feature piercing a dipping conductor. The elevated conductivity was interpreted to be due to graphite films or sulphide minerals filling oriented fracture systems; shear zone deformation disrupted the interconnected network of conductive material in the resistive zones. MT resistivity data was able to characterize the cause of shear wave splitting, thought to be common in the lower crust (Boerner, 2000; Savage, 1999), which was also associated with electrical anisotropy (Heise et al., 2006).

When interpreting the FMC MT data and the inferred electrical anisotropy there are two questions to ask: What is the nature of the conducting phase causing the electrical anisotropy, and how was the anisotropy formed?

8.2.1   Nature of the conducting phase causing anisotropy

If the anisotropy is due to macro-anisotropy, then this requires aligned structures with alternating high and low electrical conductivity values. Low conductivity (high resistivity) is easy to explain, since crystalline rocks are naturally very resistive, and unweathered shield rocks are expected to have resistivities of at least 1000 Ωm (Palacky, 1987). Well logs from the Hunt well reported by Chan (2013) found resistivity values in the basement rocks between 800 and 1500 Ωm. The isotropic shortened bandwidth inversions in Figure 6.9 imaged a uniformly resistive basement with resistivity ~2000 Ωm. This led to the choice of 2000 Ωm for the resistive phase associated with the anisotropy, which fits the MT data very well.

The high conductivity of the conductive phase could be due to either ionic conduction, with ions moving through pore fluid, or electronic conduction, with electrons moving through a conductive material such as graphite or sulphide minerals (Jones et al., 1997). Electronic conduction generally results in much lower resistivities than ionic conduction.

The FMC electrical anisotropy has a high ratio (2000/5 Ωm) and must exist throughout the region sampled by the FMC MT data, a region with spatial extent of about 20 km x 20 km. The conductive direction of the anisotropy was set to 5 Ωm, which is similar to the resistivity values observed in other studies when graphite and sulphides were assumed to be the conducting phases (Jones et al., 1997; Katsube & Mareschal, 1993).

MT data was used to infer the presence of electrical anisotropy in the Trans-Hudson Orogen by Jones et al., (1997). This study proposed that the anisotropy was caused by sulphide minerals preferentially aligned parallel to the strike of the hinges of folds that were created during Paleoproterozoic subduction-related compression. This interpretation

was corroborated by analysis on rock samples from the THO where it was exposed at the surface in Northern Saskatchewan. The authors of this study found that sulphide minerals such as pyrite could produce a bulk resistivity along-strike in the range 3-8 Ωm, and orthogonal to strike in the range 2000 to 20000 Ωm. The trace of the THO was linked to seismic reflectors in Montana by Nelson et al., (1993) and MT inversions by Jones et al., (1993) showed high conductivity zones located directly above the seismic reflector. There is no obvious seismic reflector coincident with the electrically anisotropic region in the FMC region. Graphite films on grain boundaries are thought to be an important contributor to deep crustal conductivity (Mareschal et al., 1992). Graphite has a resistivity of 0.0001 Ωm and when present as interconnected sheets on grain boundaries it can cause electrical anisotropy, with the resistivity in the conductive direction reduced from more than 1000 Ωm to 15 Ωm (Katsube & Mareschal, 1993). This is a value is 10 times less than for the equivalent proportion of saline fluid with average mid-crustal salinity, which has a conductive direction resistivity of 87 Ωm (Katsube & Mareschal, 1993). Further analysis by Katsube & Mareschal (1993) showed that graphite can cause low resistivity values of the order of 5 Ωm if the graphite is deposited in the pore spaces of the rock during metamorphism. Porosity levels in the range 0.001% - 0.1% are common in Precambrian shield rocks at intermediate to deep crustal levels (Shankland & Ander, 1983). Such a small amount of conductive graphite would not appear on seismic surveys because it would not cause a significant acoustic velocity change. Katsube & Mareschal (1993) used an assumption of graphite film thickness at 1/20 of the average pore size, and this is far below the seismic resolution limit at this depth, as explained above. A visual representation of how a small amount of interconnected conductive material can greatly change the bulk resistivity of a rock is shown in Figure 8.3.
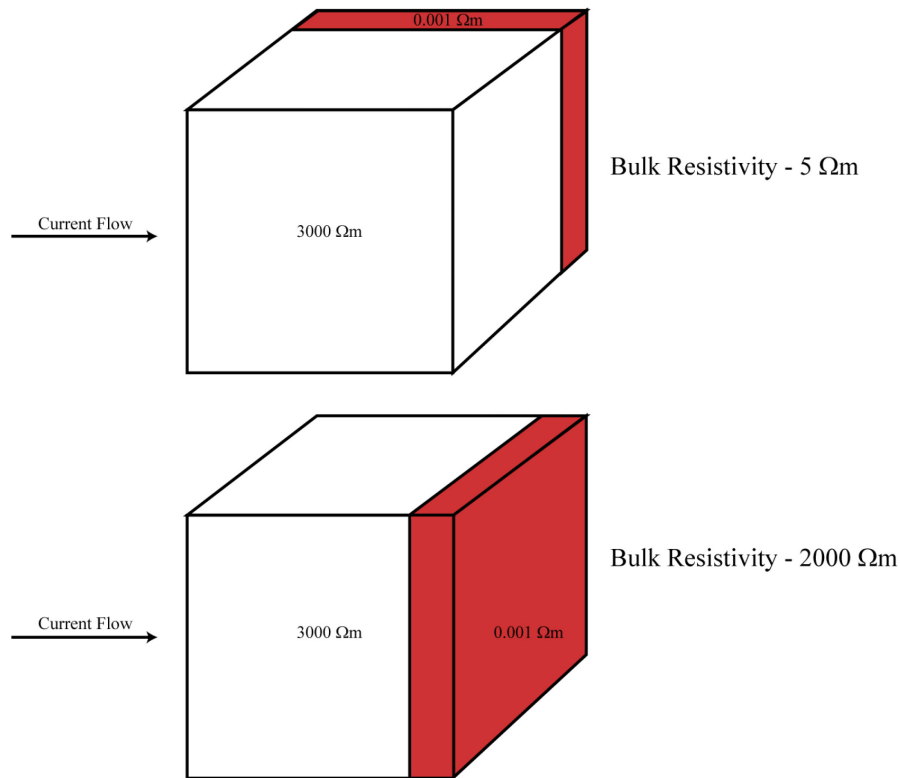
Figure 8.3: Bulk resistivity measurements made parallel and orthogonal to the direction of the conducting phase in a simplified anisotropy model. Resistive and conductive values are chosen to represent unweathered granite and graphite, respectively.

The very low resistivity in the conducting direction required by the FMC data is 5 Ωm, and this value suggests that ionic conduction in a regional fracture system is less likely than some form of electronic conduction. Further, the lack of a strong regional seismic response at the depths predicted to be electrically anisotropic suggests that a seismically reflective hinge feature containing sulphide minerals is unlikely in the FMC region, as was shown by Jones et al., (1997). For these reasons an interpretation of the conducting phase of the anisotropy being graphite is the most likely. Graphite could have been precipitated in the pore space and upon the grain surface of the basement rocks during metamorphic processes. Such deposition of graphite may not immediately produce anisotropy. Anisotropy would develop as deformation of the rocks caused the graphite in

the pores to become interconnected and oriented along some foliation. Metamorphism is naturally accompanied by high stresses that often cause foliations, or preferred directions, to develop. The next section will discuss evidence for such a deformation in the history of the FMC basement rocks.

8.2.2   Origin of the anisotropy

The stresses associated with deformation in ancient and modern shear zones have been shown to produce anisotropy in several rock properties e.g. resistivity, seismic velocities etc. (Eaton 2004; Weckmann et al., 2003; Yin et al., 2014). Geological studies of the exposed part of the CLsz 150 km north have mapped high-grade metamorphic mylonites that are strike-lineated in the center of the shear zone, and dip-lineated to either side (McDonough et al., 2000). The rocks that make up the CLsz are not electrically conductive, but they are anisotropic and that anisotropy was created and oriented by the stresses that formed the shear zone. Chapter 3 discussed how the deformation and stresses that created the Charles Lake shear zone are associated with the oxidation of magnetite to hematite so that the shear zone itself appears as a magnetic low on aeromagnetic surveys. The trace of the CLsz can be seen directly in the aeromagnetic data in Figure 3.4 from McDonough et al., (2000), it is indicated by the white outline.
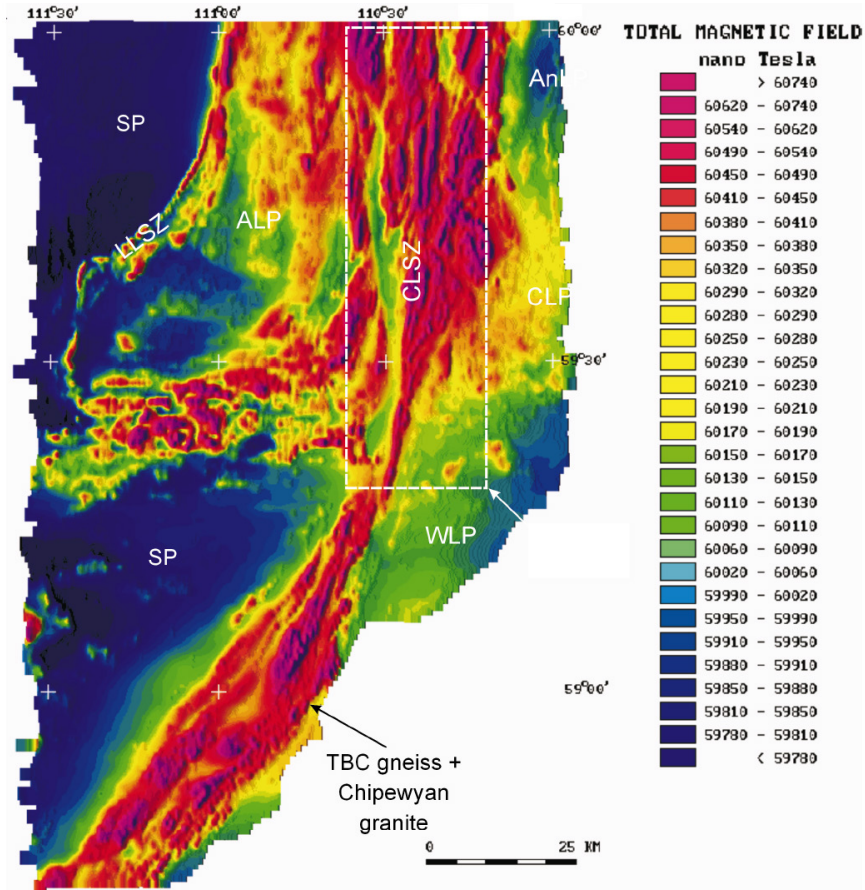
Figure 8.4: Total field aeromagnetic map for the exposed Canadian Shield in northern Alberta. ALP, Arch Lake pluton; AnLP, Andrew Lake pluton; CLSZ, Charles Lake shear zone; CLP, Colin Lake pluton; SP; Slave pluton, WLP, Wylie Lake pluton, TBC; Taltson basement complex. Modified from McDonough et al., (2000).

The rocks associated with the magnetic highs (TBC gneiss, and Chipewyan granite) continue southward, and can be traced beneath the sedimentary rocks of the WCSB with aeromagnetic data. An aeromagnetic map of the larger FMC region is shown in Figure **8.5**. The magnetic highs associated with the CLsz can be traced southward where they split into several North-South features with magnetic lows between them, these are indicated with the arrows in Figure 8.5. Two of the core samples analyzed by Walsh (2013), N02 and N03, are indicated by the brown circles near the Southern extent of the

magnetic high. These samples are nearly coincident with the center of the FMCn Profile, and exhibited TBC-like ages.

The FMC MT profiles lie just South of the termination of these magnetic high features. The FMCn East and TR profiles lie in the Southward extension of a linear North-South magnetic low (Figure 8.2 right) between two magnetic highs. The CLsz imparted multiple direction anisotropy to its constituent rocks. It is proposed in this thesis that similar shear stresses have been active further south and caused the multiple direction anisotropy observed in the MT data.
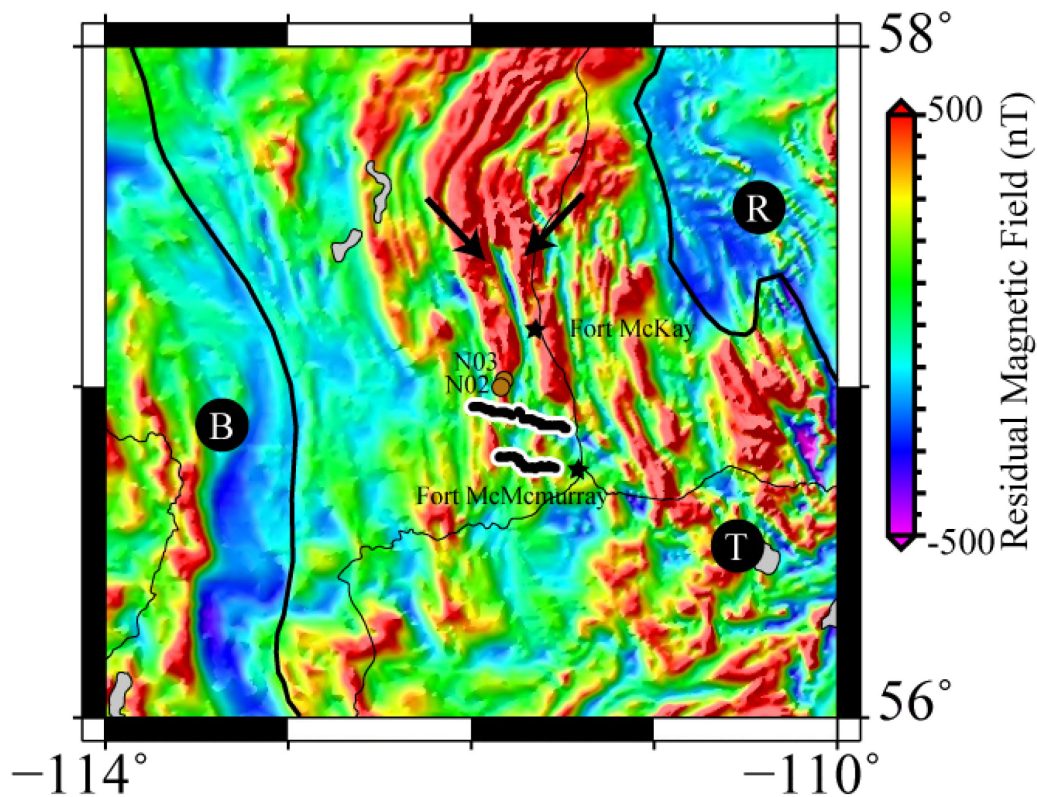
Figure 8.5: Residual field aeromagnetic data for the larger FMC region. MT profiles are indicated with white outlines. The location of Fort McMurray and Fort McKay are indicated. Letter symbols indicate geological provinces: T = Taltson Magmatic Zone, R = Rae Province, B = Buffalo Head Terrane. Brown circles indicate location of two core samples analyzed by Walsh (2013). Magnetic data downloaded from Natural Resources Canada.

8.3 Summary of MT Interpretation

The Fort McMurray MT data have shown that there is regionally extensive electrical anisotropy in the basement rocks starting at a depth of 4-5 km and extending over an area of at least 20 km x 20 km in the region between the FMCn and TR profiles. The conducting phase of the anisotropy is likely due to electrical conduction in conductive interconnected graphite films, which were deposited during metamorphic processes in the magmatic basement rocks. This interpretation is corroborated by the lack of strong seismic interface seen at the depths of the strong resistivity interface, which would likely accompany large amounts of fluid-filled fractures or accumulations of sulphide minerals, if they extended over the entirety of the region required by the MT data.

The MT data were shown to require at least two anisotropic directions. The final 2-D anisotropic resistivity model in Figure 7.7 fits the measured MT data quite well. The model is antiformal with the anisotropy strike lineated in the center, and dip lineated on either flank. Similar anisotropic directions were found in the rocks of the Charles Lake shear zone in the Canadian Shield of Alberta by McDonough et al., (2000). Aeromagnetic and core sample evidence showed it to be possible that the FMC electrical anisotropy is a result of similar shear zone stresses experiences in the CLsz. It was suggested by Walsh (2013) that a location near to Fort McKay would be the best choice for Athabasca oil sands EGS development based on RHP data and proximity to industrial processing. A supplemental MT survey west of Fort McKay, in the aeromagnetic low (Figure 8.5), would be useful in corroborating this interpretation.

8.4 Implications for Geothermal Development

For geothermal development, fluid must be made to flow through hot rock in order to extract the heat. Preferential pathways in the basement rocks are necessary for fluid to

flow from the injection well to production well. The geothermal gradient in Northern Alberta was determined by Majorowicz et al., (2012) to be ~21°/km based on precise well-bottom temperature measurement in the Hunt well of 47°C in the Precambrian basement rocks at 2.35 km depth (Chan, 2013). Models by Walsh (2013) indicated that drilling to a depth in the range 4 - 7 km would be necessary to reach the 80°C needed for economic EGS development. For this reason, an understanding of the stress state of the FMC basement rocks in the depth range 4 - 7 km depth is important, as it would help to predict the way in which induced fracture zones may propagate, and optimize fluid flow (Tester et al., 2006).

The FMC MT data showed that the resistivity structure of the crust was laterally uniform (Figure 6.3 - 6.5). A laterally uniform crust can be problematic for EGS; there are no natural zones of elevated permeability that can be exploited. Despite the laterally uniform structure, the MT data also showed a clear directional dependence beginning in the depth range 4 - 5 km , resulting from strong electrical anisotropy in the FMC basement rocks. This is within the range of depths required for economic EGS development (Hofmann et al., 2014). The directional dependence defined by the MT can be linked to the fabric of rocks. This fabric can then be related to the ancient stress state, and then compared to the modern stress state. The interaction between the fabric and the modern stress state of the rocks will affect the direction in which artificial fractures will be formed. The prevailing direction of maximum horizontal stress in Alberta is ~N40°E (Figure 3.6, from Grasby et al., 2012) and is associated with the Canadian Cordillera in the West, as well as other effects. Although borehole breakouts will align orthogonally, near to S40°E, fractures parallel to the maximum stress direction are the easiest to create. The strike of the anisotropy in the 2-D forward model was N63°E, but recall from Chapter 2 that the conductive direction is actually 90° away from the strike, at S27°E.

The Precambrian basement rocks were created long before the Canadian Cordillera generated the present day stress state, but the MT-inferred fabric of the mid-crustal FMC basement is nearly aligned with the dominant Alberta-scale stress direction. There are two axes of weakness that will affect the development of fractures in these rocks: the anisotropic fabric, along which graphite is interpreted to have been deposited, and the overall maximum stress direction. Both of these must be taken into account when considering the fracture initiation/enhancement for EGS development.

References

Archie, G. E. (1942). The electrical resistivity log as an aid in determining some reservoir characteristics. *Petroleum Transactions of AIME*, *146*, 54–62.

Arnason, K., & Flóvenz, Ó. G. (1992). Evaluation of Physical methods in Geothermal Exploration of Rifted Volcanic Crust. *Geothermal Resources Councils Transactions*, *16*, 207–214.

Banks, R. J., & Ottey, P. (1974). Geomagnetic Deep Sounding in and around the Kenya Rift Valley. *Geophysical Journal International*, *36*(2), 321–335.

Bartel, L. C., & Jacobson, R. D. (1987). Results of a controlled-source audiofrequency magnetotelluric survey at the Puhimau thermal area, Kilauea Volcano, Hawaii. *Geophysics*, *52*(5), 665–677.

Berktold, A. (1983). Electromagnetic studies in geothermal regions. *Geophysical Surveys*, *6*, 173–200.

Bertrand, E. A., Caldwell, T. G., Hill, G. J., Wallin, E. L., Bennie, S. L., Cozens, N., Onacha, S. A., et al. (2012). Magnetotelluric imaging of upper-crustal convection plumes beneath the Taupo Volcanic Zone, New Zealand. *Geophysical Research Letters*, *39*(2), 6.

Bibby, H. M., Caldwell, T. G., Davey, F. J., & Webb, T. H. (1995). Geophysical evidence on the structure of the Taupo Volcanic Zone and its hydrothermal circulation. *Journal of Volcanology and Geothermal Research*, *68*, 29–58.

Bibby, H. M., & Risk, G. F. (2005). Misinterpretation of electrical resistivity data in geothermal prospecting: a case study from the Taupo Volcanic Zone. *proceedings world geothemal congress 2005* (p. 8). Antalya, Turkey.

Boerner, D. E. (1999). Electrical Conductivity in the Precambrian Lithosphere of Western Canada. *Science*, *283*, 668–670.

Boerner, D. E., Kurtz, R. D., Craven, J. A., Ross, G. M., & Jones, F. W. (2000). A synthesis of electromagnetic studies in the Lithoprobe Alberta Basement Transect: constraints on Paleoproterozoic indentation tectonics. *Canadian Journal of Earth Sciences*, *37*(11), 1509–1534.

Burwash, R. A. (1979). Uranium and thorium in the Precambrian basement of western Canada. II. Petrologic and tectonic controls. *Canadian Journal of Earth Sciences*, *16*(3), 472–483.

Burwash, R. A., Baadsgaard, H., & Peterman, Z. E. (1962). Precambrian K-Ar ages from the Western Canada Sedimentary Basin. *Journal of Geophysical Research*, *67*, 1617–1625.

References

Burwash, R. A., & Cumming, G. L. (1976). Uranium and thorium in the Precambrian basement of western Canada. I. Abundance and distribution. *Canadian Journal of Earth Sciences*, *13*(2), 284–293.

Cagniard, L. (1953). Basic Theory of the Magneto-Telluric Method of Geophysical Prospecting. *Geophysics*, *18*(3), 65.

Caldwell, G. T., Pearson, C., & Zayadi, H. (1986). Resistivity of Rocks in Geothermal Systems: A laboratory study. *Proceedings 8th Geothermal Workshop* (pp. 221–231).

Caldwell, T. G., Bibby, H. M., & Brown, C. (2004). The magnetotelluric phase tensor. *Geophysical Journal International*, *158*(2), 457–469.

Chacko, T., De, S. K., Creaser, R. A., & Muehlenbachs, K. (2000). Tectonic setting of the Taltson magmatic zone at 1.9 - 2.0 Ga: a granitoid-based perspective. *Canadian Journal of Earth Sciences*, *37*(11), 1597–1609.

Chan, J. (2013). *Subsurface Geophysical Characterization of the Crystalline Canadian Shield in Northeastern Alberta: Implications for Geothermal Development. University of Alberta - MSc Thesis*. University of Alberta.

Conly, F. M., Crosley, R. W., & Headley, J. V. (2002). Characterizing sediment sources and natural hydrocarbon inputs in the lower Athabasca River, Canada. *Journal of Environmental Engineering Science*, *199*(1), 187–199.

Corrigan, D., Pehrsson, S., Wodicka, N., & de Kemp, E. (2009). The Palaeoproterozoic Trans-Hudson Orogen: a prototype of modern accretionary processes. *Geological Society, London, Special Publications*, *327*(1), 457–479.

Duba, A. G., & Shankland, T. J. (1982). Free carbon & electrical conductivity in the Earth's mantle. *Geophysical Research Letters*, *9*(11), 1271–1274.

Eaton, D. W. (2004). Lithospheric anisotropy structure inferred from collocated teleseismic and magnetotelluric observations: Great Slave Lake shear zone, northern Canada. *Geophysical Research Letters*, *31*, L19614.

Egbert, G., & Booker, J. (1986). Robust estimation of geomagnetic transfer functions. *Geophysical Journal International*, *87*, 173–194.

Eysteinsson, H., Árnason, K., & Flóvenz, Ó. G. (1994). Resistivity methods in geothermal prospecting in Iceland. *Surveys in geophysics*, *15*, 263–275.

Flóvenz, Ó. G. (2005). The role of electrical interface conduction in geothermal exploration. *Proceedings World Geothermal Congress 2005* (p. 9). Antalya, Turkey.

Flóvenz, Ó. G., & Karlsdottir, R. (2000). TEM-Resistivity image of a geothermal field in N-Iceland and the relation of the resistivity with lithology and temperature. *Proceedings World Geothermal Congress 2000* (pp. 1127–1132). Tohoku, Japan.

167

References

Fowler, C. M. R. (1990). *The Solid Earth: An Introduction to Geophysics* (2nd ed.). Cambridge: Cambridge University Press.

Glover, P. W. J., Hole, M. J., & Pous, J. (2000). A modified Archie's law for two conducting phases. *Earth and Planetary Science Letters*, *180*, 369–383.

Grasby, S. E., Allen, D. M., Raymond, J., Bell, S., Chen, Z., Ferguson, G., Jessop, A., et al. (2012). *Geothermal energy resource potential of Canada, Open File 6914 (revised)*. *Geological Survey of Canada* (Vol. Open File, p. 322 p.).

Groom, R. W., & Bailey, R. C. (1989). Decomposition of Magnetotelluric Impedance Tensors in the Presence of Local Three-Dimensional Galvanic Distortion. *Journal of Geophysical Research*, *94*(B2), 1913–1925.

Hanmer, S., Bowring, S. A., Breeman, O., & Parrish, R. R. (1992). Great Slave Lake shear zone, NW Canada: mylonitic record o f Early Proterozoic continental convergence , collision and indentation. *Journal of Structural Geology*, *14*(7), 757–773.

Harinarayana, T., Abdul Azeez, K. K., Murthy, D. N., Veeraswamy, K., Eknath Rao, S. P., Manoj, C., & Naganjaneyulu, K. (2006). Exploration of geothermal structure in Puga geothermal field, Ladakh Himalayas, India by magnetotelluric studies. *Journal of Applied Geophysics*, *58*(4), 280–295.

Hayes, B. J. R., Christopher, J. E., Rosenthal, L., Los, G., McKercher, B., Minken, D., Tremblay, Y. M., et al. (1994). Cretaceous Mannville Group of the Western Canada Sedimentary Basin. *Geological Atlas of the Western Canada Sedimentary Basin* (pp. 317–333).

Heise, W., Caldwell, T. G., Bibby, H. M., & Brown, C. (2006). Anisotropy and phase splits in magnetotellurics. *Physics of the Earth and Planetary Interiors*, *158*, 107–121.

Heise, W., & Pous, J. (2001). Effects of anisotropy on the two-dimensional inversion procedure. *Geophysical Journal International*, *147*(3), 610–621.

Heise, W., & Pous, J. (2003). Anomalous phases exceeding 90° in magnetotellurics: anisotropic model studies and a field example. *Geophysical Journal International*, *155*(1), 308–318.

Henderson, J. B., McGrath, P. H., James, D. T., & Macfie, R. I. (1987). An integrated geological, gravity and magnetic study of the Artillery Lake area and the Thelon Tectonic Zone, District of Mackenzie. *Current Research, Part A. Geological Survey Canada, Paper 87 1-A*, 803–814.

Hoffman, P. F. (1988). United Plates of America, the birth of a craton-Early Proterozoic assembly and growth of Laurentia. *Annual Review of Earth and Planetary Sciences*, *16*, 543–603.

References

Hoffman, P. F. (1989a). Precambrian Geology and Tectonic History of North America. *The Geology of North America Vol. A, The Geology of North America-An Overview. The Geology Society of America.* The Geology Society of America.

Hoffman, P. F. (1989b). Speculations on Laurentia's first gigayear (2.0 to 1.0 Ga). *Geology*, *17*(2), 135–138.

Hofmann, H., Babadagli, T., & Zimmermann, G. (2014). Hot water generation for oil sands processing from enhanced geothermal systems: Process simulation for different hydraulic fracturing scenarios. *Applied Energy*, *113*, 524–547. Elsevier Ltd.

Ingham, M. R. (1991). Numerical modelling of magnetotelluric soundings from the Central Volcanic Region. *Proceedings 13th New Zealand Geothermal Workshop 1991* (pp. 15–20).

Jiracek, G. R., Scot, L., & Biehler, L. W. (1996). Tracing Crustal Isotherms Under the Western Margin of the Jemez Mountains Using Sage and Industry Magnetotelluric Data. *New Mexico Geological Seociety Guidebook, 47th Field Conference, Jemez Mountains Region*, 129–133.

Jones, A. G. (1988). Static Shift of Magnetotelluric Data and its Removal in a Sedimentary Basin Environment. *Geophysics*, *53*(7), 967–978.

Jones, A. G., Craven, J. A., McNeice, G. W., Ferguson, I. J., Boyce, T., Farquharson, C., & Ellis, R. G. (1993). North American Central Plains conductivity anomaly within the Trans-Hudson orogen in northern Saskatchewan, Canada. *Geology*, *21*, 1027–1030.

Jones, A. G., Groom, R. W., Kurtz, R. D., Alan, G., & Ross, W. (1993). Decomposition and modelling of the BC87 dataset. *Journal of Geomagnetism and Geoelectricity*, *45*, 1127–1150.

Jones, A. G., Katsube, T. J., & Schwann, P. (1997). The longest conductivity anomaly in the world explained: sulphides in fold hinges causing very high electrical anisotropy. *Journal of geomagnetism and Geoelectricity*, *49*, 1619–1629.

Jones, F. W., & Munro, R. A. (2002). Regional geoelectrical complexity of the Western Canada Basin from magnetotelluric tensor invariants. *Earth Planets and Space*, *54*(9), 899–905.

Katsube, T. J., & Mareschal, M. (1993). Petrophysical model of deep electrical conductors: Graphite lining as a source and its disconnection due to uplift. *Journal of Geophysical Research*, *98*(B5), 8019–8030.

Lund, J. W., Freeston, D. H., & Boyd, T. L. (2011). Direct utilization of geothermal energy 2010 worldwide review. *Geothermics*, *40*(3), 159–180. CNR-Istituto di Geoscienze e Georisorse.

References

Majorowicz, J. A., Unsworth, M. J., Chacko, T., Gray, A., Heaman, L., Potter, D. K., Schmitt, D. R., et al. (2012). Geothermal Energy as a Source of Heat for Oil Sands Processing in Northern Alberta, Canada. *Heavy-oil and oil sand petroleum systems in Alberta and beyond: AAPG Studies in Geology*, *64*, 1–22.

Mareschal, M., Fyfe, W. S., Percival, J., & Chan, T. (1992). Grain-boundary graphite in Kapuskasing gneisses and implications for lower-crustal conductivity. *Nature*, *357*, 674–676.

Mareschal, M., Kellett, R. L., Kurtz, R. D., & Ludden, J. N. (1995). Archaean cratonic roots mantle shear zones and deep electrical anisotropy. *Nature*, *375*, 134–137.

Maxwell, J. C. (1861). On physical lines of force. *Philosophical Magazine*.

McDonough, M. R., McNicoll, V. J., Schetselaar, E. M., & Grover, T. W. (2000). Geochronological and kinematic constraints on crustal shortening and escape in a two-sided oblique-slip collisional and magmatic orogen, Paleoproterozoic Taltson magmatic zone, northeastern Alberta. *Canadian Journal of Earth Sciences*, *37*(11), 1549–1573.

McNeice, G. W., & Jones, A. G. (2001). Multisite, multifrequency tensor decomposition of magnetotelluric data. *Geophysics*, *66*(1), 158–173.

Meyer, M. T., Bickford, M. E., & Lewry, J. F. (1992). The Wathamun Batholith: An early Proterozoic continental arc in the Trans-Hudson orogenic belt. *Bulletin Geological Society America*, *104*, 1073–1085.

Moeck, I. (2013). Classification of geothermal plays according to geological habitats. *IGA Academy Report 0101-2013* (p. 10).

Monger, J. W. H., & Price, R. (2002). The Canadian Cordillera: geology and tectonic evolution. *CSEG Recorder*, 17–36.

Nelson, K. D., Baird, D. J., & Walters, J. J. (1993). Trans-Hudson orogen and Williston basin in Montana and North Dakota: New COCORP deep-profiling results. *Geology*, *21*, 447–450.

Newman, G. A., Gasperikova, E., Hoversten, M. G., & Wannamaker, P. E. (2008). Three-dimensional magnetotelluric characterization of the Coso geothermal field. *Geothermics*, *37*(4), 369–399.

Nieuwenhuis, G. (2011). *Magnetotelluric Imaging of Precambrian Lithosphere Beneath Southern Alberta*. *Masters Abstracts International*. University of Alberta.

Palacky, G. J. (1987). Resistivity characteristics of geologic targets. In: Nabighian, M.N. (Ed.). *Electromagnetic Methods in Applied Geophysics, vol. 1, Soc. Explor. Geophys, Tulsa, OK, USA* (pp. 53–130).

References

Parkinson, W. D. (1959). Directions of rapid geomagnetic fluctuations. *Geophysical Journal International*, *2*(1), 1–14.

Partzsch, G. M., Schilling, F. R., & Arndt, J. (2000). The influence of partial melting on the electrical behavior of crustal rocks: laboratory examinations, model calculations and geological interpretations. *Tectonophysics*, *317*, 189–203.

Pek, J. (2012). Magnetotelluric inversion for 2D generally anisotropic conductivities. *Extended Abstract 21st Workshop, Darwin, Australia* (pp. 1–4).

Pek, J., & Verner, T. (1997). Finite-difference modelling of magnetotelluric fields in two-dimensional anisotropic media. *Geophysical Journal International*, *128*(3), 505–521.

Pellerin, L., Johnston, J. M., & Hohmann, G. W. (1996). A numerical evaluation of electromagnetic methods in geothermal exploration. *Geophysics*, *61*(1), 121–130.

Presnall, D. C., Simmons, C. L., & Porath, H. (1972). Changes in electrical conductivity of a synthetic basalt during melting. *Journal of Geophysical Research*, *77*(29), 5665–5672.

Price, R. (1994). Cordilleran tectonics and the evolution of the Western Canada Sedimentary Basin. In G. Mossop & I. Shetsen (Eds.), *Geological Atlas of the Western Canada Sedimentary Basin* (Mossop, G., pp. 13 – 24). Calgary, Canada: Canadian Society of Petroleum Geologists and Alberta Research Council.

Quist, A. S., Iarshall, W. L. R., Franck, E. U., & Osten, W. V. (1970). A reference solution for electrical conductance measurements to 800 and 12,000 Bars. Aqueous 0.01 Demal Potassium Chloride, *74*(10), 2241–2243.

Reilly, W. I. (1972). New Zealand gravity map series. *New Zealand Journal of Geology and Geophysics*, *15*(1), 3–15.

Robinson, R., Smith, E. G. C., & Latter, J. H. (1981). Seismic studies of the crust under the hydrothermal areas of the Taupo Volcanic Zone, New Zealand. *Journal of Volcanology and Geothermal Research*, *9*, 253–267.

Rodi, W., & Mackie, R. (2001). Nonlinear conjugate gradients algorithm for 2-D magnetotelluric inversion. *Geophysics*, *66*(1), 174.

Ross, G. M. (2000). Introduction to special issue of Canadian Journal of Earth Sciences: The Alberta Basement Transect of Lithoprobe. *Canadian Journal of Earth Sciences*, *37*(11), 1447–1452.

Ross, G. M. (2002). Evolution of Precambrian continental lithosphere in Western Canada: results from Lithoprobe studies in Alberta and beyond. *Canadian Journal of Earth Sciences*, *39*(3), 413–437.

References

Ross, G. M., & Eaton, D. W. (1999). Basement reactivation in the Alberta Basin: Observational constraints and mechanical rationale. *Bulletin of Canadian Petroleum Geology*, *47*(4), 391–411.

Ross, G. M., Parrish, R. R., Villeneuve, M. E., & Bowring, S. A. (1991). Geophysics and geochronology of the crystalline basement of the Alberta Basin, western Canada. *Canadian Journal of Earth Sciences*, *28*(4), 512–522.

Sandberg, S. K., & Hohmann, G. W. (1982). Controlled-source audiomagnetotellurics in geothermal exploration. *Geophysics*, *47*(1), 100–116.

Schill, E., Geiermann, J., & Kümmritz, J. (2010). 2-D Magnetotellurics and gravity at the geothermal site at Soultz-sous-Forêts. *Proceedings World Geothermal Congress 2010* (pp. 1–10). Bali, Indonesia.

Schilling, F. R., Partzsch, G. M., Brasse, H., & Schwarz, G. (1997). Partial melting below the magmatic arc in the central Andes deduced from geoelectromagnetic field experiments and laboratory data. *Physics of the Earth and Planetary Interiors*, *103*, 17–31.

Selway, K., Thiel, S., & Key, K. (2012). A simple 2-D explanation for negative phases in TE magnetotelluric data. *Geophysical Journal International*, *188*(3), 945–958.

Shankland, T. J., & Ander, M. E. (1983). Electrical conductivity, temperatures, and fluids in the lower crust. *Journal of Geophysical Research*, *88*(B11), 9475–9484.

Simpson, F., & Bahr, K. (2005). *Practical magnetotellurics*. *Cambridge Univ. Press, Cambridge, U. K.* (p. 270). Cambridge, U.K.: Cambridge University Press.

Spichak, V. V., Geiermann, J., Zakharova, O., Calcagno, P., Genter, A., & Schill, E. (2010). Deep temperature extrapolation in the Soultz-sous-Forêts geothermal area using magnetotelluric data. *Proceedings 35th Workshop on Geothermal Reservoir Engineering*. Stanford, California.

Spichak, V. V., & Manzella, A. (2009). Electromagnetic sounding of geothermal zones. *Journal of Applied Geophysics*, *68*(4), 459–478.

Spichak, V. V., Zakharova, O. K., & Rybin, A. K. (2011). Methodology of the indirect temperature estimation basing on magnetotelluric data: Northern Tien Shan case study. *Journal of Applied Geophysics*, *73*(2), 164–173. Elsevier B.V.

Sprenke, K. F., Wavra, C. S., & Godfrey, J. D. (1986). Geophysical expression of the Canadian Shield of northeastern Alberta. *Alberta Research Council - Natural Resources Division - Alberta Geological Survey*, *52*, 60.

Stegena, L. (1976). Electric Conductivity Structure and Geothermal Reservoirs. *Acta Geodaet. Geophys. et Montanist. Acad. Sci. Hung. Tomus*, *11*(3-4), 377–393.

References

Tarling, D. H., & Hrouda, F. (1993). *Magnetic Anisotropy of Rocks*. *Chapman & Hall* (1st ed., p. 217). London, U.K.: Chapman & Hall.

Tester, J. W., Anderson, B. J., Batchelor, A. S., Blackwell, D., DiPippo, R., Drake, E. M., Garnish, J., et al. (2006). Impact of enhanced geothermal systems on US energy supply in the twenty-first century. *Philosophical transactions. Series A, Mathematical, physical, and engineering sciences*, *365*(1853), 1057–94.

Thériault, R. J. (1992). Nd Isotopic Evolution of the Taltson Magmatic Zone, Northwest Territories , Canada: Insights into Early Proterozoic Accretion along the Western Margin of the Churchill Province '. *The Journal of Geology*, *100*(4), 465–475.

Tikhonov, A. N. (1950). On Determing Electrical Characteristics of the Deep Lyers of the Earth's Crust. *Doklady*, *73*(2), 295–297.

Türkoğlu, E., Unsworth, M. J., & Pană, D. I. (2009). Deep electrical structure of northern Alberta (Canada): implications for diamond exploration. *Canadian Journal of Earth Sciences*, *46*(2), 139–154.

Unsworth, M. J. (2014). Geophysis 424 Class Notes D.2 - Theory of Magnetotellurics Over a 2-D Earth. *University of Alberta* (pp. 1–15).

Unsworth, M. J., & Rondenay, S. (2012). Mapping the Distribution of Fluids in the Crust and Lithospheric Mantle Utilizing Geophysical Methods. *Metasomatism and the Chemical Transformation of Rock: The Role of Fluids in Terrestrial and Extraterrestrial Processes*, Lecture Notes in Earth System Sciences (pp. 535–598). Berlin, Heidelberg: Springer-Verlag.

Ussher, G., & Harvey, C. (2000). Understanding the resistivities observed in geothermal systems. *Proceedings World Geothermal Congress 2000* (pp. 1915–1920). Tohoku, Japan.

Vozoff, K. (1991). The Magnetotelluric Method. In M. N. Nabighian (Ed.), *Electromagnetic Methods in Applied Geophysics: Volume 2B* (pp. 641–711). Tulsa, OK, USA: Society of Exploration Geophysicists.

Walsh, N. J. (2013). *Geochemistry and Geochronology of the Precambrian Basement Domains in the Vicinity of Fort McMurray, Alberta: A Geothermal Perspective.* University of Alberta.

Wannamaker, P. E. (1986). Electrical Conductivity of Water-Undersaturated Crustal Melting. *Journal of Geophysical Research*, *91*(B6), 6321–6327.

Wannamaker, P. E. (2005). Anisotropy Versus Heterogeneity in Continental Solid Earth Electromagnetic Studies: Fundamental Response Characteristics and Implications for Physicochemical State. *Surveys in Geophysics*, *26*, 733–765.

Wannamaker, P. E. (2007). Integrated dense array and transect MT surveying at dixie valley geothermal area, Nevada; structural controls, hydrothermal alteration and

deep fluid sources. *Proceedings 32nd Workshop on Geothermal Reservoir Engineering* (p. 6). Stanford, California.

Watson, E. B., & Brenan, J. M. (1987). Fluids in the lithosphere, 1. Experimentally determined wetting characteristics of CO2-H2O fluids and their implications for fluid transport, host-rock physical properties and fluid inclusion formation. *Earth and Planetary Science Letters*, *85*, 497–515.

Weckmann, U. (2006). Phase Splitting: Evidence for mantle anisotropy? *Kolloquium „Elektromagnetische Tiefenforschung", 21.* (pp. 276–80). Deutsche Geophysikalische Gesellschaft DGG.

Weckmann, U., Ritter, O., & Haak, V. (2003). A Magnetotelluric study of the Damara Belt in Namibia 2. internal structure of the Waterberg Fault/Omaruru Lineament. *Physics of the Earth and Planetary Interiors*, *138*(2), 91–112.

Weidelt, P., & Kaikkonen, P. (1994). Local 1-D interpretation of magnetotelluric B-polarization impedances. *Geophysical Journal International*, *117*(3), 733–748.

Wiese, H. (1962). Geomagnetische Tiefentellurik Teil II: Die Streichrichting der Undergrundstrukturn des Elektrischen Widerstandes, Erschlossen Aus Geomagnetischen Variationen. *Geofisica Pura e Applicata*, *52*(1), 83–103.

Wright, G. N., McMechan, M. E., & Potter, D. E. G. (1994). Structure and architecture of the Western Canada sedimentary basin. In G. Mossop & I. Sheltsin (Eds.), *Geological Atlas of the Western Canada Sedimentary Basin* (pp. 25–40). Calgary, Canada: Canadian Society of Petroleum Geologists and Alberta Research Council.

Yin, Y., Unsworth, M. J., Liddell, M., Pană, D. I., & Craven, J. A. (2014). 3-D resistivity structure of the Great Slave Lake shear zone, northwest Canada, in press Geophysical Journl International.